

Annual Report 2017

MLZ is a cooperation between:

Bayerisches Staatsministerium für
Bildung und Kultus, Wissenschaft und Kunst



SPONSORED BY THE



Federal Ministry
of Education
and Research

The Heinz Maier-Leibnitz Zentrum (MLZ):

The Heinz Maier-Leibnitz Zentrum is a leading centre for cutting-edge research with neutrons and positrons. Operating as a user facility, the MLZ offers a unique suite of high-performance neutron scattering instruments. This cooperation involves the Technische Universität München, the Forschungszentrum Jülich and the Helmholtz-Zentrum Geesthacht. The MLZ is funded by the German Federal Ministry of Education and Research, together with the Bavarian State Ministry of Education, Science and the Arts and the partners of the cooperation.

The Forschungs-Neutronenquelle Heinz-Maier-Leibnitz (FRM II):

The Forschungs-Neutronenquelle Heinz-Maier-Leibnitz provides neutron beams for the scientific experiments at the MLZ. The FRM II is operated by the Technische Universität München and is funded by the Bavarian State Ministry of Education, Science and the Arts.

Joint Annual Report 2017
of the MLZ and FRM II



Moving to pastures new

In 1957, the first research reactor in Germany became operational: the so-called “Atomic Egg”. The occasion of the 60th birthday of neutrons in Germany is a good opportunity not only to look back, but also to try to glimpse into the future. We celebrated the Atomic Egg’s birthday with a number of exhibitions and talks. Looking back in time, Germany has been a leading light in driving the innovation for neutron instrumentation since the 1950s. Today, the Heinz Maier-Leibnitz Zentrum (MLZ) is firmly established as Germany’s foremost facility for neutron science. Its strength derives from a fruitful collaboration between the three main partners - the Technical University of Munich (TUM), the Forschungszentrum Jülich (FZJ) and the Helmholtz-Zentrum Geesthacht (HZG) - incorporating research groups from universities and the Max Planck Institutes.

The expertise of the MLZ in neutron instrumentation becomes apparent from its involvement in the construction of the European Spallation Source (ESS) in Lund, Sweden. Seven instruments were contributed by the MLZ partners (JCNS/FZJ, GEMS/HZG and FRM II/TUM), having been proposed and built together with neutron centres from other European countries.

The next big step for the MLZ’s own instrumentation in the new neutron guide hall east was achieved by changing the plug of beam tube no. 6a, thereby facilitating the insertion of the future ultra-cold neutron source. The new guide hall will thus have at its disposal thermal, cold and ultra-cold neutrons, as well as positrons.

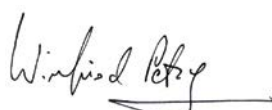
Two large scientific projects involving the FRM II and MLZ successfully applied for funding in 2017: the transregional project TRR 80 and the EU Project LEU FOREVER (Fuel FOR REsearch Reactors). Together, they total up to more than 15 mio. Euros!

The partners of the MLZ are paving the way to fostering this fruitful collaboration beyond the current cooperation agreement. Visible signs are the new twin buildings on the site in front of the Atomic Egg, for which we celebrated the ground-breaking ceremony in early 2017. These buildings will bring together staff from the MLZ and FRM II who are now scattered over the entire campus, thus fostering closer collaboration and increasing corporate identity. They will also provide additional laboratory space, as well as the urgently needed workshop for the FRM II.

In 2017, we initiated a process to map out a vision for the MLZ for the next decade. Intense discussions took place during the MLZ staff retreat, in the MLZ science groups, and with the MLZ advisory boards. Many exciting ideas have been developed, which will be fine-tuned in discussions with the MLZ users during a user meeting in September 2018 and put to the test in an MLZ review in November 2018. With the improved affinity of the partners and an increased corporate identity, the MLZ will be primed for a bright future.



Thomas Brückel



Winfried Petry



Johannes Nußbickel



Anton Kastenmüller

Scientific Highlights & Reports

Twisted magnetic fluctuations in superconductors	10
Neutrons probe a spin spiral.....	10
Skyrmions in a polar magnet.....	11
Tiny particles in the fast lane	11
Analysing proteins for gene regulation	12
Neutrons make hydrogen atoms visible	12
A new antiferromagnet enters the scene.....	13
The softer, the better?	13

Scientific Reports

Materials Science

Characterization of precipitates in the new Co-Re alloy for gas turbines.....	14
In situ SANS on anode materials for lithium-ion batteries	15
Morphology of fuel cell membranes.....	16
Light on the brain anatomy of a 260 million years old forerunner of mammals.....	17
Neutron computer tomography for preserving charred wooden cultural objects.....	18
Adsorption-induced deformation of silica monoliths with hierarchical porosity.....	19
Neutrons confirm Li-ion cells can last much longer with a proper anode	20
Magnetic order in $\text{CoFe}_{0.1}\text{Cr}_{1.9}\text{O}_4$ nanoparticles	21
In situ diffraction study on inhomogeneity and relaxation in lithium batteries.....	22
Water-based processing of LiFePO_4 studied using neutron and X-ray diffraction.....	23
Zinc phosphate dental cement microstructure: a key to its properties	24

Quantum Phenomena

Transverse acoustic phonon anomalies at intermediate wave vectors in MgV_2O_4	25
Breakdown of helical order in the Dzyaloshinskii-Moriya AF $\text{Ba}_2\text{CuGe}_2\text{O}_7$	26
Ferromagnetism in the ground state of the pyrochlore $\text{Yb}_2\text{Ti}_2\text{O}_7$	27
Vortex lattice domain formation in the type-II/1 superconductor Nb	28
Spin structure of MnO nanoparticles, powder and single crystal	29

Soft Matter

SANS/SAXS studies of iron oxide nanoparticles for cancer treatment.....	30
Elucidating lipid vesicle fusion by time-resolved neutron reflectivity	31
SANS experiments on membrane proteins with invisible detergents	32
Fullerene addition affects self-assembly of conjugated copolymer films.....	33
Structure and dynamics of non-lamellar lipid bilayers at interfaces.....	34
Polymer dynamics under cylindrical repulsive confinement	35

Membrane reorganizations in desert crust cyanobacteria	36
Interaction of an amphiphilic guanosine-based ionophore with lipid bilayers	37
Elucidation of the morphology of anion exchange membranes for fuel cells	38

Structure Research

Proton ordering in HacacPy.....	39
Phase diagram and properties of ferroelectric $K_{0.5}Na_{0.5}NbO_3 - Bi_{1/2}Na_{1/2}TiO_3$	40
Homo-chiral crystallization and mono-chiral helimagnetism in $CsCuCl_3$	41
Magnetic structure of the multiferroic melilite $Ca_2CoSi_2O_7$	42

Neutron Methods

Magnetic contrast neutron waveguide for all-oxide heterostructures	43
Connecting MARIA with MBE: PNR in UHV via portable transport chamber	44
Fast fission cross sections (n,f) of ^{238}U , ^{237}Np , and ^{242}Pu	45

Instrumental Upgrades & Services

News from the instruments.....	48
When the instruments operate smoothly	56
Support for MLZ from Jülich: Engineering and detectors	60
Exchanging the plug JMA16 in the beam tube SR6 at FRM II	66

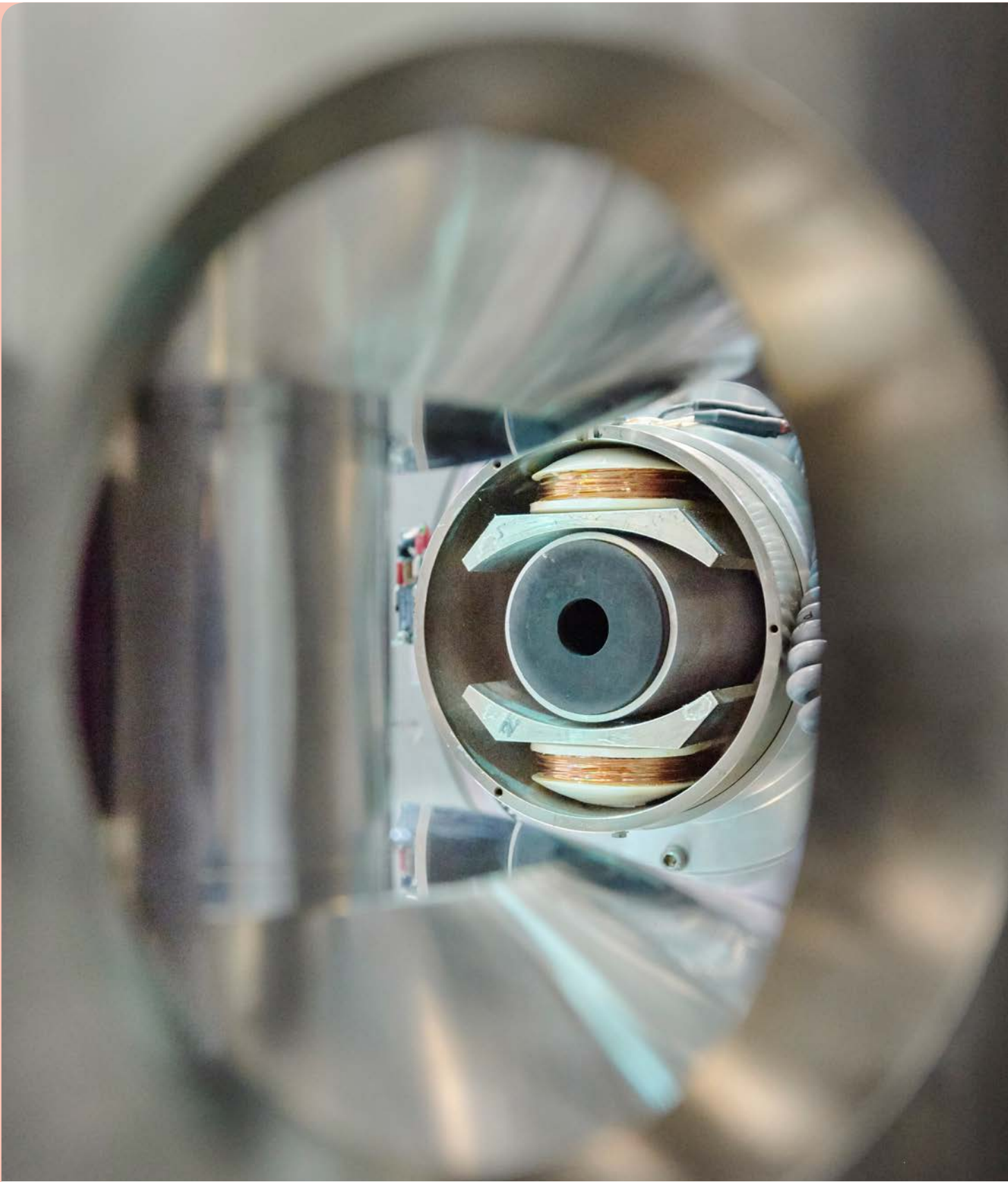
Reactor & Industry

Operation of the research reactor FRM II.....	72
Quantitative comparability of heavy ion and in-pile irradiation experiments.....	74

Facts & Figures

The year in pictures.....	78
Workshops, Conferences and Schools	84
From science to society.....	86
Behind the scenes – At the User Office in 2017	88
Organisation	90
Staff	92
Budget	93
Publications & Theses	94
Partner institutions.....	102
Imprint.....	106

Where do the polarized neutrons come from? A look backwards to the neutron polarizer of the instrument POLI through the window in the HTS magnet at the sample position.



Scientific Highlights & Reports

Twisted magnetic fluctuations in superconductors

$\text{Li}_{0.8}\text{Fe}_{0.2}\text{OHFeSe}$ is a new type of iron-selenide superconductor which exhibits very mysterious behavior: iron is a magnetic material where the electrons are aligned in parallel, thus precluding superconductivity. This new type by contrast is superconducting, since the FeSe layers are separated by $(\text{Li}_{0.8}\text{Fe}_{0.2})\text{OH}$ blocking layers. It was



Scientists and technicians at the three axes spectrometer PUMA – as seen with the artist's eye.

found that the magnetic resonant mode is located at an odd wave vector which connects to two electron Fermi pockets, indicating that the Cooper pairing symmetry with antiparallel electron spins still remains as a sign-reversed type, as with other iron-based superconductors. A further surprise comes from the high energy regime: the spin excitation slowly disperses outward in the low-energy region, and above 60 meV the dispersion suddenly turns into an inward shape, forming the twisted dispersion. No such behavior has been observed in any other Fe-based superconductors. Instead, it rather resembles the well-known “hour-glass” dispersion in copper-oxide based high T_c superconductors, which manifests the highest superconducting transition temperature among unconventional superconductors. This experimental observation implies that the higher superconducting transition temperature may favor not only the sign-changing pairing channels, but also the twisted spin excitations.

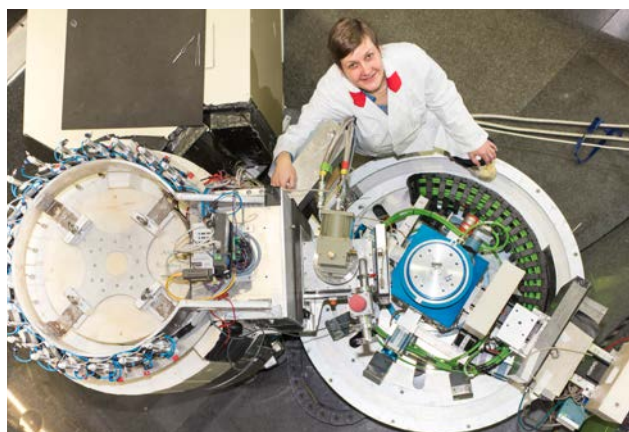
Experiments were carried out at PUMA.

B. Pan, Y. Shen, D. Hu, Y. Feng, J.T. Park, A.D. Christianson, Q. Wang, Y. Hao, H. Wo, Z. Yin, T.A. Maier and J. Zhao; Structure of spin excitations in heavily electron-doped $\text{Li}_{0.8}\text{Fe}_{0.2}\text{ODFeSe}$ superconductors; Nat. Commun. 8 (1), 123 (2017)

Neutrons probe a spin spiral

Crystalline materials form highly symmetric lattice structures, this symmetry being the basic precondition to describe the physical behavior of any compound. Phase transitions, such as water crystallizing into ice, lead to a change in symmetry. The British theoretical physicist Jeffrey Goldstone stated that whenever a continuous symmetry is broken, a low-energy excitation with a zero energy gap (Goldstone mode) emerges. In magnetic materials, a broken symmetry can be associated with a spontaneous formation of a periodic spin structure, e.g. a spiral propagating along a certain direction of the crystal. In the cubic spinel ZnCr_2Se_4 , such a spiral forms on the magnetic Cr^{3+} ions along one of the 3 main cubic axes: x, y or z. The choice among these 3 equivalent directions is spontaneous. If the z direction is chosen, for instance, the gapless Goldstone mode in the spin-excitation spectrum will form, meaning that spin waves along the z axis can be excited with vanishingly low energies.

It was generally assumed that the spin waves along the two other directions (x and y) that are perpendicular to the spiral would remain at high energies, not contributing to any thermodynamic or transport properties of the compound. However, new results obtained on ZnCr_2Se_4 using neutron scattering, which is the most direct method of measuring spin-wave energies, has challenged this preconception. It has been demonstrated that low-energy modes, similar to those predicted by the Goldstone theorem, also exist in orthogonal directions. Because of their very small but finite



Some of the experiments were carried out at the cold three axes spectrometer PANDA, to see here with Astrid Schneidewind, instrument scientist and co-author of the publication.

energy gap, they have been termed pseudo-Goldstone modes. This result can crucially change the interpretation of low-temperature measurements of helimagnets and stimulate future theoretical effort. They should generally apply not only to spin spirals, but also to a much broader class of materials where the broken symmetry makes a spontaneous choice among several equivalent crystal directions.

Experiments were carried out at PANDA.

Y. V. Tymoshenko, Y. A. Onyukienko, T. Müller, R. Thomale, S. Rachel, A. S. Cameron, P. Y. Portnichenko, D. V. Efremov, V. Tsurkan, D. L. Abernathy, J. Ollivier, A. Schneidewind, A. Piovano, V. Felea, A. Loidl, and D. S. Inosov; Pseudo-Goldstone magnons in the frustrated $S=3/2$ Heisenberg helimagnet ZnCr_2Se_4 with a pyrochlore magnetic sublattice; Phys. Rev. X 7, 041049 (2017)

Skyrmions in a polar magnet

Skyrmions show up in various chiral magnetic systems, typically in periodic whirl-like spin vortex structure lattices. Early theoretical predictions and subsequent experiment, however, revealed that a different type of skyrmion emerges due to another kind of asymmetry of the under-



These beautiful crystals are the polar magnet VOSe_2O_5 investigated, whose crystal structure consists of stacked square lattice tetragonal pyramids.

lying lattice. In this case, an applied magnetic field parallel to the polar axis induces a triangular skyrmion lattice: the spin rotates perpendicular to the plane and outwards from the core of the vortex. This type of skyrmion is known as the Néel-type skyrmion and has frequently been observed in magnetic ultrathin films and multilayers, which provide an important arena for practical applications in spintronics devices.

Scientists identified this kind of skyrmion lattice in the tetragonal polar magnet VOSe_2O_5 using small angle neutron scattering. They found a cycloidal spin state at zero field and a Néel-type skyrmion lattice phase under a magnetic field along the polar axis. Adjacent to this phase, another magnetic phase of an incommensurate spin texture was found at lower temperatures, tentatively assigned to a square skyrmion lattice phase. These findings exemplify the versatile features of Néel-type skyrmions in bulk materials, and provide a unique opportunity to explore the physics of topological spin textures in polar magnets.

Experiments were carried out at KWS-1.

T. Kurumaji, T. Nakajima, V. Ukleev, A. Feoktystov, T. Arima, K. Kakurai, and Y. Tokura; Néel-Type Skyrmion Lattice in the Tetragonal Polar Magnet VOSe_2O_5 ; Phys. Rev. Lett. 119, 237201 (2017)

Tiny particles in the fast lane

The hairy one-component nanocomposites (OCNCs) are tiny (1-200 nm) and seem to be a kind of a future silver bullet with the potential to offer enormous possibilities in many fields. These tiny molecules might be used for energy storage in supercapacitors, for the precise manufacturing of tunable hypersonic photonic crystals and much more. In biomedicine, envisaged applications are, e.g., polypeptide-based hybrids for drug carriers.

SiO_2 particles grafted with polyisoprene chains were chosen as a model; the particles are 6 nm in size, the "hair" being about 6 nm thick. Although many of the characteristics of OCNCs are known, the real structure is not; in particular, the question of how they move has yet to be answered. Skillful labeling with hydrogen or deuterium labeling followed by neutron scattering provides access to both the monomer density in the corona as well as the conformation of the grafted chains. The molecular motion depends on the interactions of the chains with the nanoparticle surfaces and their concentration. The conformation of a grafted chain is identical to that of a free chain, implying a high mutual penetration of the coronas from different particles. The brush crowding leads to topological confinement of the chain



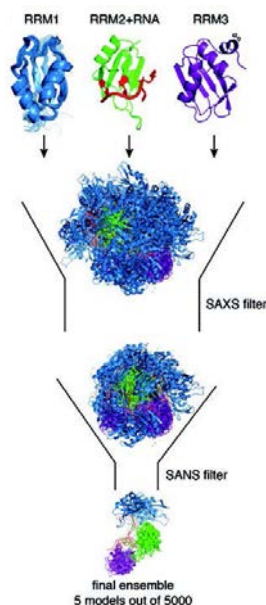
One of the application fields of OCNC is in racing cars, because they exhibit novel morphologies, dielectric and mechanical properties, overcome the challenge of dispersion, and are expected to display structure-related emergent properties that distinguish them from the more established field of nanocomposites.

dynamics: At local scales, the segmental dynamics is unchanged, while at the scale of the chain, the dynamics appears to be slowed down. Thus, the dynamics of OCNC materials depends on topological features rather than on any changes on the segmental scale. For OCNCs, particle size and grafting density, determining the cone, are an important source for chain confinement.

Experiments were carried out at J-NSE.

C. Mark, O. Holderer, J. Allgaier, E. Hübner, W. Pyckhout-Hintzen, M. Zamponi, A. Radulescu, A. Feoktystov, M. Monkenbusch, N. Jalarvo, and D. Richter; Polymer Chain Conformation and Dynamical Confinement in a Model One-Component Nanocomposite; Phys. Rev. Lett. 119, 047801 (2017)

Analysing proteins for gene regulation



Structural modeling of TIA-1 RRM123 domain arrangements bound to U15 RNA based on SAXS and SANS data. The three available high-resolution input structures of individual domains are used to calculate 5000 models of the RNA complex and 100 structures are shown. Following application of a SAXS filter, an ensemble of 67 structures remains, which is further reduced to five structures after scoring against the SANS data.

RNA binding proteins (RBPs) represent an important class of multi-domain proteins, which regulate gene expression by recognizing linear or structured RNA sequence motifs. NMR spectroscopy is usually well-suited for obtain-

ing structural information on multi-domain proteins. However, with increasing molecular weight, NMR analysis of such protein complexes is challenging and does not deliver sufficient information. The combination of NMR spectroscopy and small-angle scattering (SANS) is advantageous as NMR spectroscopy provides information on binding interfaces, domain conformations and dynamics, while SANS experiments yield information on overall shapes and domain distances.

In general, SANS data recorded at various D₂O concentrations could provide valuable structural information on the distances between domains in multi-domain proteins if the hydrogens of some, but not all, domains are replaced by the heavier deuterium atoms. This requires efficient, robust and generally applicable domain-selective deuterium labeling as SANS requires protein amounts in the milligram range. Sortase A-mediated ligation enabled the production of a domain-selective deuterium labeled RBP to acquire experimental SANS data, which was used to score 5000 modeled structures based on NMR and the X-ray crystallography data of single domains in the RNA bound and free states. A representative ensemble of 100 initial models illustrates the large possible conformational space.

Domain-selective perdeuteration combined with contrast-matched SANS, SAXS, NMR and computational modeling makes it possible to define relative domain distances and orientations by filtering initial models against all available data. This approach is generally applicable to a study of the conformational arrangements of individual domains in multi-domain proteins as well as changes induced by ligand binding and is expected to be widely applicable.

Experiments were carried out at KWS-2.

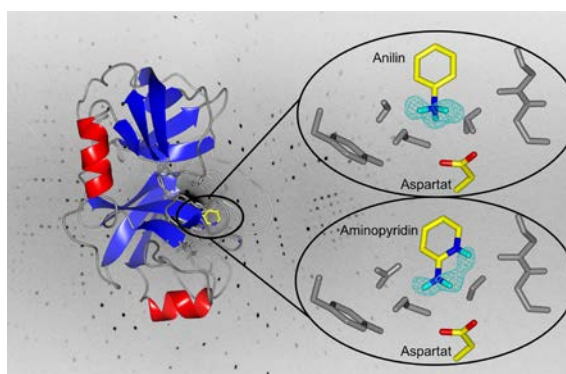
M. Sonntag, P. K. Ankush Jagtap, B. Simon, M.-S. Appavou, A. Geerlof, R. Stehle, F. Gabel, J. Hennig, and M. Sattler, Segmental, Domain-Selective Perdeuteration and Small-Angle Neutron Scattering for Structural Analysis of Multi-Domain Proteins; Angew. Chem. Int. Ed. 56, 9322 (2017)

Neutrons make hydrogen atoms visible

Biomolecules often bind to partners, such as drug molecules, via so-called hydrogen bonds. Exact knowledge of the position of the hydrogen atoms on relevant molecular groups is crucial if new drugs are to be developed in pharmaceutical research. The drug molecules are often weak acids or bases, and change easily between the protonated state (with hydrogen atom) and the deprotonated state (without hydrogen atom).

Trypsin was used as a model enzyme for the class of so-called trypsin-like serine proteases involved in the digestion process, blood coagulation, cancer metastasis or immune response. During digestion, trypsin recognizes and always cleaves a peptide bond of a protein (the substrate) after the strongly basic amino acids arginine and lysine. Not so in this case: The head group of the trypsin inhibitor 2-aminopyridine is more basic than that of aniline, but surprisingly the amino group is not protonated upon binding to trypsin, the proton being attached to the ring nitrogen despite a greater distance from a negatively charged aspartate of trypsin. However, based on a second data set collected from a

large crystal, the amino group of aniline was found to be clearly protonated and thus positively charged.



Left side: the enzyme trypsin in ribbon presentation. Right side: close-up of the binding pocket. The chicken wire network in cyan represents the measured density for the hydrogen atoms of aniline and 2-aminopyridine. The head group of aniline clearly possesses three hydrogen atoms and is thus positively charged. The head-group of 2-aminopyridine carries only two hydrogens, but here the pyridine-type nitrogen in the ring system is protonated.

Experiments were carried out at BIODIFF.

J. Schiebel, R. Gaspari, A. Sandner, K. Ngo, H-D. Gerber, A. Cavalli, A. Ostermann, A. Heine and G. Klebe; Charges shift protonation: neutron diffraction reveals that aniline and 2-aminopyridine are protonated upon binding to trypsin; Angew. Chem. Int. Ed. 56, 1 (2017)



Data could be saved more reliably and permanently using antiferromagnets.

Antiferromagnetic materials have several advantages over conventional ferromagnetic materials. They are insensitive to external and perturbing magnetic fields. Using antiferromagnets in memory devices could help save information more reliably and permanently than ferromagnetic materials can.

A Chinese-German team of researchers has presented a novel synthetic antiferromagnetic material, which may

prove pioneering for progress in nanomedicine and information technology. In contrast to a ferromagnet, an antiferromagnet does not show a magnetic field detectable from outside. However, the antiferromagnet is a magnetic material: It is simply that the little compass needles, “spins”, of the electrons do not point in parallel directions, but are antiparallel. Therefore, the magnetic moments erase each other.

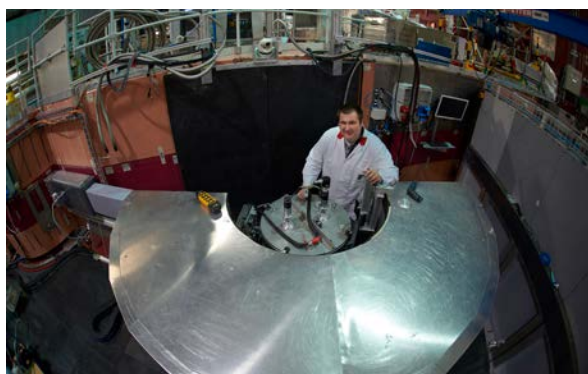
The new synthetic antiferromagnet under study has several ferromagnetic manganese layers only a few nanometers thick, coupled by an ultra-thin isolating titanium oxide layer. This leads to coupled antiferromagnetic spins whose direction of spin changes when they are transferred from one layer to the other. Changes in the layer structure will also alter the properties of the magnetic material. The researchers used polarized neutron reflectivity measurements to show that the single layers of the new material can be magnetized individually. They were also able to show that an external magnetic field can reverse individual layers of the material.

Experiments were carried out at MARIA.

B. Chen, H. Xu, C. Ma, S. Mattauch, D. Lan, F. Jin, Z. Guo, S. Wan, P. Chen, G. Gao, F. Chen, Y. Su, and W. Wu, All-oxide-based synthetic antiferromagnets exhibiting layer-resolved magnetization reversal; Science 357, 191 (2017)

The softer, the better?

The advent of solid-state batteries has spawned renewed research on lithium solid ionic conductors and the underlying principles of ionic diffusion. These materials are intrinsically soft in nature, which has always been believed to be beneficial for ionic transport. It is usually assumed that ion transport comes with lower activation barriers in softer, more polarizable lattices. Within a more polarizable lattice, the anions can dis-



Some of the experiments were carried out at the neutron powder diffractometer SPODI, to see here with Anatoliy Senyshyn, instrument scientist and co-author of the publication.

place more easily and the energetic cost for a moving ion is much smaller. This chemical intuition has been corroborated by the good conduction observed in materials with iodine or sulfide anions, as compared to the stiffer and less polarizable oxides.

Neutron powder diffraction, in combination with impedance spectroscopy and speed of sound measurements of the dynamics of the anion lattice, has been employed to understand the influence of the lattice polarizability in $\text{Li}_6\text{PS}_5\text{X}$ ($\text{X} = \text{Cl}, \text{Br}, \text{I}$). It can indeed be observed that significant changes in the ionic transport occur due to a softening of the lattice. With decreasing bond-strength, i.e. increasing polarizability, the activation barriers do indeed decrease as expected. However, the increasing softness of the lattice detrimentally affects the temperature dependence of reaction rates and prevents a higher conductivity with increasing lattice polarizability. These data show that the current belief of “the softer, the better” needs to be revisited in order to design better superionic conductors.

Experiments were carried out at SPODI.

M. Kraft, S. P. Culver, M. Calderon, F. Boecher, T. Krauskopf, A. Senyshyn, C. Dietrich, A. Zevalkink, J. Janek, and W. G. Zeier; On the Influence of Lattice Polarizability on the Ionic Conductivity in the Lithium Superionic Argyrodites $\text{Li}_6\text{PS}_5\text{X}$ ($\text{X} = \text{Cl}, \text{Br}, \text{I}$); J. Am. Chem. Soc. 139, 10909 (2017)

R. Gilles¹, L. Karge¹, D. Mukherji², P. Strunz³, P. Beran³, J. Rösler², W. Petry¹

¹Heinz Maier-Leibnitz Zentrum (MLZ), Technical University of Munich (TUM), Garching, Germany; ²Institut für Werkstoffe, Technische Universität Braunschweig, Braunschweig, Germany; ³Nuclear Physics Institute ASCR, Řež, Prague, Czech Republic

The Co-Re high temperature alloy is a candidate for supplementing the Ni-base superalloys in gas turbines. The main goal in developing the alloy is to increase its maximum service temperature. The Co-Re alloy system studied, with nominal composition Co-17Re-23Cr-1.2Ta-2.6C, consists of a Co matrix in which three kinds of precipitates, namely a TaC, Cr₂₃C₆ and σ phase (Cr₂Re₃ type), are embedded. The kinetics of the precipitation of the hardening carbide is particularly fast and it is generally not possible to suppress precipitation during cooling from the single phase γ Co at high temperatures. For this reason, it is impossible to observe the precipitation of the most important strengthening phase TaC by direct imaging. Nevertheless, using the in-situ small-angle neutron scattering (SANS) method, we were able to observe the growth of the TaC precipitates during isothermal holding at high temperatures and by way of an example the results at 1473 K are shown in Fig. 1. After 7 hours of holding, the mean size of TaC precipitates increased from 21 nm to 52 nm, while the volume fraction of TaC in this Q-range remained fairly stable below 1 %. These results show that the small TaC precipitates remain stable in nanosize scale at high temperatures and are therefore suitable for alloy strengthening.

Due to the very high flux and low background of the SANS-1 instrument of the MLZ, the evolving precipitation can even be observed during in-situ cooling by measuring the changes in the integral intensity on the detector for a fixed instrument set-up. In the temperature region 1393 - 1300 K and with a cooling rate of ~ 10 K min⁻¹ Cr₂₃C₆ precipitation was detected. This phase is not very useful in Co-Re alloys, as it is not stable at very high temperature. However, the size and volume fraction of the Cr₂₃C₆ and σ phases influence the formation of TaC precipitates. Due to the fact that in this temperature region the Co-Re matrix also undergoes an allotropic phase transformation and that the reverse transformation has a hysteresis, it is highly desirable and necessary to study the behaviour of the precipitate in-situ at high temperatures. Thus, ageing and cooling experiments with SANS have a huge impact in helping to gain a deeper insight into Co-Re alloys at their anticipated operating temperatures and can significantly improve the development of this alloy for industrial application.

[1] L. Karge et al., *The influence of C/Ta ratio on TaC precipitates in Co-Re base alloys investigated by small-angle neutron scattering*; *Acta Mater.* 132, 354 (2017)

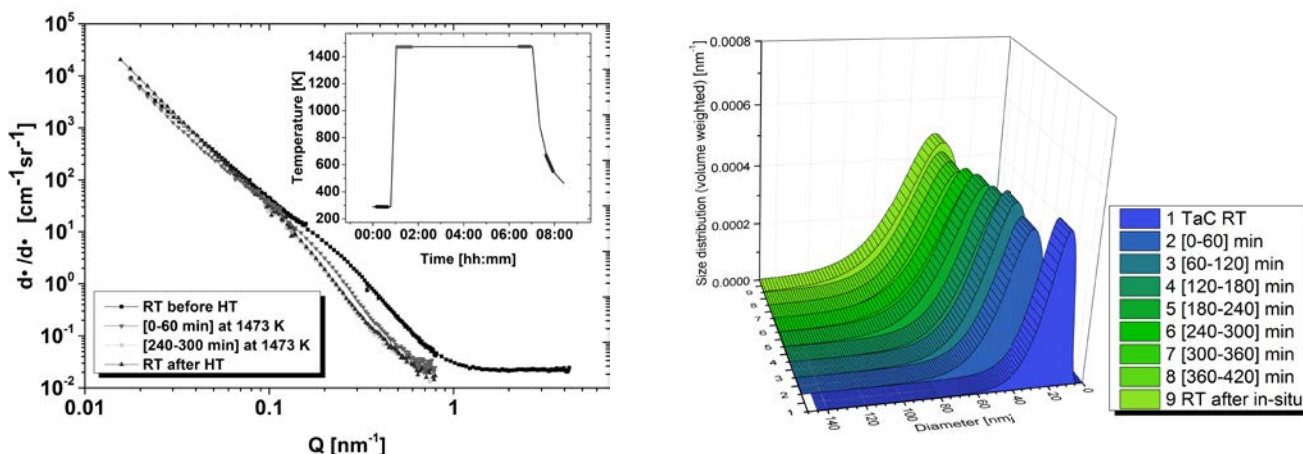


Figure 1: In situ SANS patterns of CoRe sample at RT, start of holding at 1473 K, end of holding after about 5 hours and after cooling to RT (left). Size distribution (volume weighted) and volume fraction of TaC is plotted at RT and during holding at 1473 K (right).

X. He^{1,2}, J. Li², H. Frielinghaus³
¹Helmholtz Institute Münster / Forschungszentrum Jülich GmbH (IEK 12), Münster, Germany; ²MEET Battery Research Center, Institute of Physical Chemistry, University of Münster, Münster, Germany; ³Jülich Centre for Neutron Science (JCNS) at MLZ, Forschungszentrum Jülich GmbH, Garching, Germany

The binary metal phosphide (M-P, M = Cu, Fe, Sn, Sb) compounds are of great interest as negative electrode materials for high energy density lithium-ion batteries. However, the morphological and structural details at the nanoscale upon electrochemical (de)lithiation are still unclear as yet and require further detailed investigation.

In situ small-angle neutron scattering at the instrument KWS-1 was used to investigate the morphological changes of two metal phosphide materials during the initial electrochemical lithiation-delithiation cycle. By comparing the results of scanning electron microscopy for the electrodes at different electrochemical states, it was possible to evaluate the electrochemical reactions of the active materials, including the solid electrolyte interphase formation, the swelling and recovery of nanoparticles the appearance of cracks, and stripping at nanoscale. For the data evaluated from SANS experiments performed in situ, we focused on

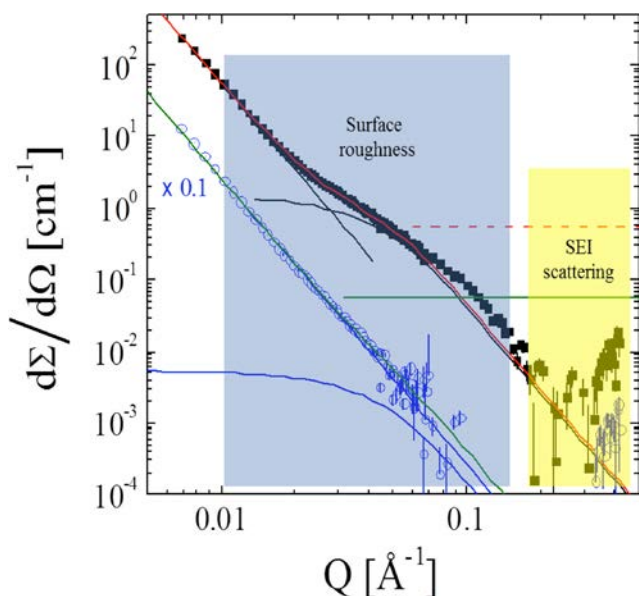


Figure 1: Scattering functions obtained from the in situ SANS measurement for Cu_3P (black) and Sn_3P_4 (blue) electrodes lithiated to 0.01 V. Total fitting functions (red and green), the incoherent background (horizontal lines in red/dashed and green/solid), and their separated two components (Porod and globular particles, both black and blue) are indicated.

a standardized fitting procedure, combining the Porod surface scattering from large domains (larger than $0.5 \mu\text{m}$), the amplitude of smaller globules (8 nm in diameter) and background (shown in Fig. 1) for all states during the discharge/charge process in the same way. In the case of Cu_3P , the scattering signal almost recovers to the initial state after the full cycle, which indicates a high degree of reversibility. In contrast, the anode prepared by Sn_3P_4 did not show this high degree of reversibility. These findings also agreed with the electrochemical performance over several cycles.

With in situ x-ray diffraction measurements, which detected and characterized phase transition occurring primarily at various electrochemical states, the energy storage mechanism was further explained. During the lithiation process of the Cu_3P and Sn_4P_3 electrodes, the insertion of Li ions into the active component caused a large tensile stress. In the case of the Cu_3P material, no further reaction occurred between the Li ions and Cu at the high lithiation state (low potential), which limited the whole volume expansion and reduced the related stress. As a result, only some branch cracks formed on the electrode surface at the end of the first cycle, but the structure and morphology of the active materials can be well maintained. For the Sn_4P_3 electrode, although Sn can further react with Li and significantly contribute to the specific capacity, it leads to large volume changes and stress. The interconnected cracks were able to isolate part of the active material particles from the current collector, and the active material was finally detached during the delithiation process. These results provide new insights into the electrochemical nanostructural changes of active materials, which are used as an anode for lithium-ion batteries via conversion and alloying reactions. This can help to understand the electrochemical behaviour of the materials and further improve their electrochemical performance.

[1] X. He et al., *In Situ Investigations on the Structural and Morphological Changes of Metal Phosphides as Anode Materials in Lithium-Ion Batteries*; *Adv. Mater. Interfaces* 4(7), 1601047 (2017)

Morphology of fuel cell membranes

O. Ivanova¹, W. Lüke², A. Majerus², M. Kruteva³, N. K. Szekely¹, W. Pyckhout-Hintzen³, M.-S. Appavou¹, M. Monkenbusch³, R. Zorn³, W. Lehnert^{2,4}, O. Holderer¹

¹Jülich Centre for Neutron Science (JCNS) at MLZ, Forschungszentrum Jülich GmbH, Garching, Germany; ²Institute of Energy and Climate Research IEK-3: Electrochemical Process Engineering, Forschungszentrum Jülich GmbH, Jülich, Germany; ³Jülich Centre for Neutron Science (JCNS), Forschungszentrum Jülich GmbH, Jülich, Germany; ⁴Faculty of Mechanical Engineering, RWTH Aachen University, Aachen

Polymer Electrolyte Fuel Cells (PEFC) – together with hydrogen produced from renewable sources – are widely seen as alternative fuel towards emission-free energy conversion system. In particular, High Temperature Polymer Electrolyte Membrane Fuel Cells (HT-PEFC) operating at elevated temperatures between 120–180 °C are considered to be very promising due to their short start-up time, favourable power-to-weight ratio, good water management and high CO tolerance, which permit a wide range of applications in the medium power range. Naturally, a basic understanding of the material properties and the way its processing influences the structure and performance is required.

Small angle neutron scattering at KWS-2

In the present work, the morphology of the polymer electrolyte membrane poly(2,5-benzimidazole) (ABPBI) in its pristine state and after doping with phosphoric acid (PA) for proton conduction has been investigated on a wide range of length scales, using small angle neutron scattering (SANS) at the KWS-2 instrument and X-ray scattering, as well as transmission electron microscopy (TEM) and polarized light

microscopy. The contrast of the PA doped membranes favours neutron experiments due to the H/D sensitivity. The measurements reveal that the membranes have fractal morphology on a wide range of length scales. The formation of crystalline aggregates upon aging in the amorphous matrix of the pristine ABPBI membrane could also be demonstrated. Thus, for PA doped ABPBI, SANS data exhibit the same fractal dimension for fresh and aged membranes at Q-values below 0.015 Å⁻¹ while at larger Q, the slope of the aged sample changes from 3.7 (surface fractal) to 2.6 (mass or volume fractal). These changes are consistent with the X-ray data (SAXS) for the pristine samples, see Fig. 1 and associated with the aging effect on crystalline formation [1]. We believe that our findings contribute to the general understanding of HT-PEFC's, i.e. their mechanical and transport properties and thus may be helpful in modifying well-established, and developing new membrane materials.

[1] O. Ivanova et al., *Influence of morphology on physical properties of poly(2,5-benzimidazole) membranes*; *J. Membrane Sci.* **533**, 342 (2017)

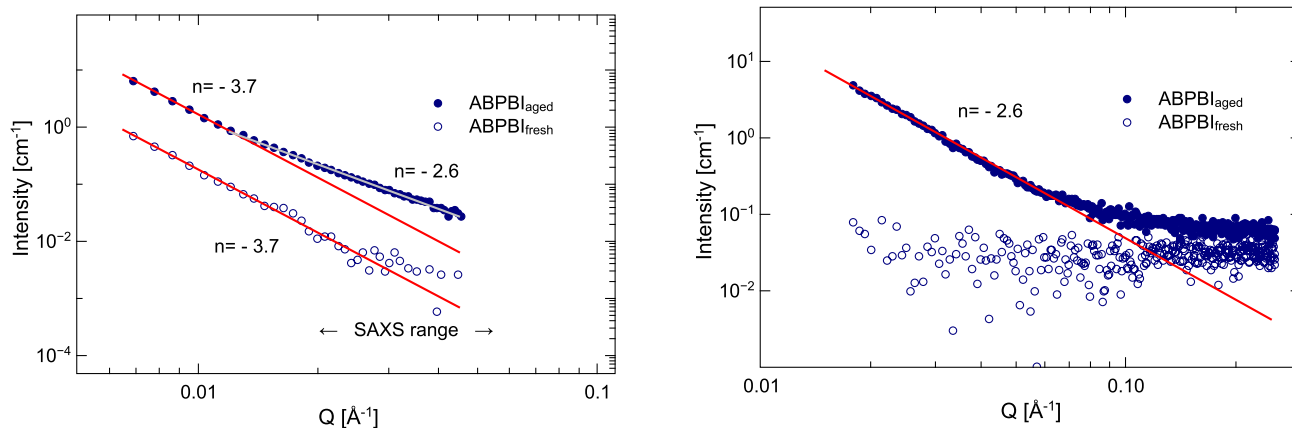


Figure 1: Scattered intensity from aged and fresh poly(2,5-benzimidazole) membranes, i.e. ABPBI_{aged} and ABPBI_{fresh} as a function of the scattering wave vector obtained by SANS (KWS-2 @MLZ), left and laboratory SAXS (JCNS, FZJ), right. Independent of contrast, the aged lot exhibits fractal decay in both data sets (SANS and SAXS), while the fresh lot did not show any evidence of small angle scattering on length scales covered by SAXS.

M. Laaß¹, B. Schillinger²

¹Department of General Zoology, Faculty of Biology, University of Duisburg-Essen, Essen, Germany; ²Heinz Maier-Leibnitz Zentrum (MLZ) and Department of Physics, Technical University of Munich, Garching, Germany

Thousands of vertebrate fossils are housed in palaeontological collections worldwide, which were assigned to the Therapsida. The Therapsida were the forerunners of mammals and the dominant group of tetrapods on land before the emergence of the dinosaurs. In former times they were also called “mammal-like reptiles”, because therapsids show both primitive reptilian as well as mammalian features.

Unfortunately, all non-mammalian therapsids are completely extinct and can only be studied from fossils. Moreover, the endocranial cavities of fossil therapsid skulls are often filled with iron-rich rock matrix (Figure 1a), which makes it difficult to investigate their internal cranial structure. As soft tissue is not preserved, the brain anatomy of the therapsids is almost completely unknown. If at all, some information can only be deduced from impressions of soft-tissue structures in the surrounding brain cavity, which is in most cases only incompletely ossified and preserved. Besides this, it seems that the therapsid brain often did not completely fill in the braincase as it is also known from modern turtles and reptiles.

We investigated a fossil skull of the mammalian forerunner *Diictodon feliceps* at the facility ANTARES at FRM II (Fig. 1 a, b). Neutrons were well suited to penetrate this fossil and produced a good contrast between bones and matrix. As a result, we found sharp impressions of several blood vessels on the inner side of the braincase, which allowed a more complete reconstruction of the vascular system of

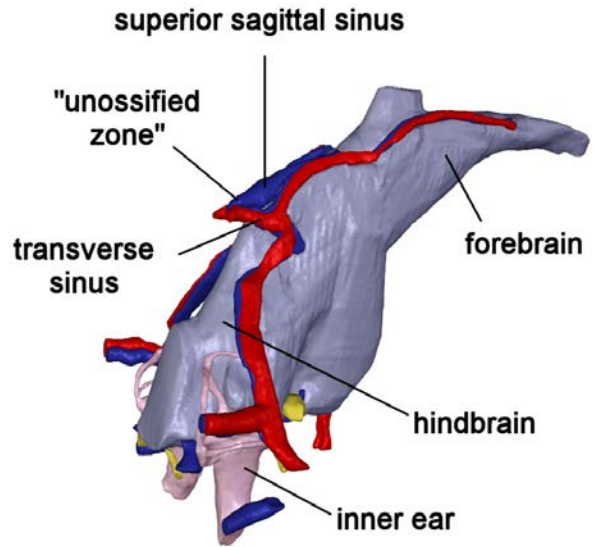


Figure 2: Brain endocast of the therapsid *Diictodon feliceps* with reconstructed blood vessels.

the therapsid brain. So it was also possible to clarify the nature of the so called “unossified zone”, which is a depression in the braincavity at the level of the hindbrain (Fig. 2). The neutron tomographic images clearly showed that the unossified zone was a terminal chamber of several blood vessels.

[1] M. Laaß et al., What did the “unossified zone” of the non-mammalian therapsid braincase house?; *J. Morphol.* 278(8), 1020 (2017)

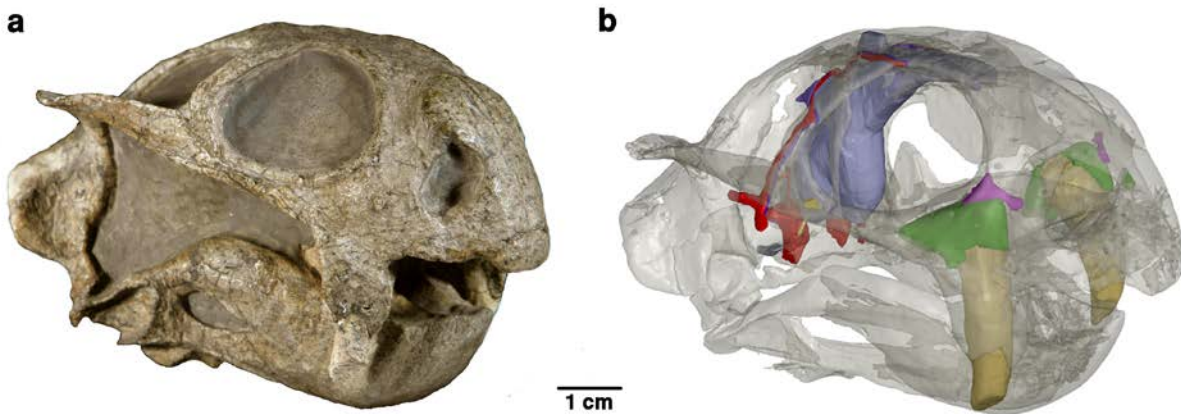


Figure 1: Fossil skull (a) and the virtual 3D model (b) of the mammalian forerunner *Diictodon feliceps* from the collection of the Museum of Natural History in Berlin (number MB.R.1000).

K. Osterloh¹, A. Nusser², S. Röhrs², S. Radujkovic³, A. Schwabe⁴, S. Söllrad⁵, T. Bücherl⁶, I. Reiche²

¹BAM 8.3 Radiological Methods, Berlin, Germany; ²Rathgen-Forschungslabor, Staatliche Museen zu Berlin (SMB), Stiftung Preußischer Kulturbesitz (SPK), Berlin, Germany; ³Vorderasiatisches Museum, SMB, SPK, Berlin, Germany; ⁴Stiftung Luthergedenkstätten in Sachsen-Anhalt, Museumstechnik, Präventive Konservierung, Wittenberg, Germany; ⁵Heinz Maier-Leibnitz Zentrum (MLZ), Technical University of Munich, Garching, Germany; ⁶Radiochemie München RCM, Technical University of Munich, Garching, Germany

Generally, computed tomography (CT) is focussed on elucidating the internal structure of objects. In the context of the preservation of cultural objects, it is the internal composition of the material, rather than the structural details, that is of interest. This type of problem is encountered, in particular, in the case of ancient wooden objects requiring preservation treatment. They are generally stabilised by impregnation with an organic consolidant. In this case, both the wooden matrix and the chemical applied consist of hydrocarbons. Consequently, the increase in contrast resulting from the agent might be hardly detectable by X-ray CT, particularly if the amount of agent taken up remains low. If the hydrocarbon content of the consolidant is higher than that of wood, then an absorption difference is detectable using neutrons. This has been proven by a study of the preservation of charred wooden objects at the NECTAR facility at FRM II.

Pieces of charred wood, serving as a model for extremely fragile objects, were treated with seven different consolidants that have various uptake properties into wood, and subsequently subjected to neutron CT (Fig. 1). The intention was that the consolidant should penetrate into the fragile zones rather than having it distributed throughout the whole object. Since the scope of the study did not allow the investigation of one and the same specimen before and after treatment, histograms have been calculated from the reconstructed image data to demonstrate the density shift

between treated and untreated samples. In cases of massive uptake, i.e. some 30% of the original weight, areas of increased density clearly indicated the distribution within the specimens. Density histograms accordingly showed a shift from lower to higher values. However, the interpretation of histograms proved to be rather challenging in cases of low uptake, around 5 % of the initial weight as e.g. with polyvinylbutyral. Since it was not obvious whether the shift seen here was due to an uptake of substances or to structural differences, the areas of increased density were stratified in a new approach, as indicated by different colours. The increased density close to the surface (arrow in Fig. 2) could be related to an uptake of consolidant into a fragile zone, whereas the denser areas deeper within the bulk might be partially due to structural differences between the reference and the treated sample. These results give rise to novel approaches of semi-quantitative evaluations of neutron CTs. The support of the study by the Berliner Antike-Kolleg (BAK-TT8-2015) and by Prof. Dr. Markus Hilgert, SPK, is gratefully acknowledged.

[1] K. Osterloh et al., *Neutron computer tomography for preserving charred wooden cultural objects*; *N.i.Ke.-Schriftenreihe 1, 94 (2017), ISSN 2567-1251*



Figure 1: Experimental set-up for the neutron CT measurements at NECTAR.

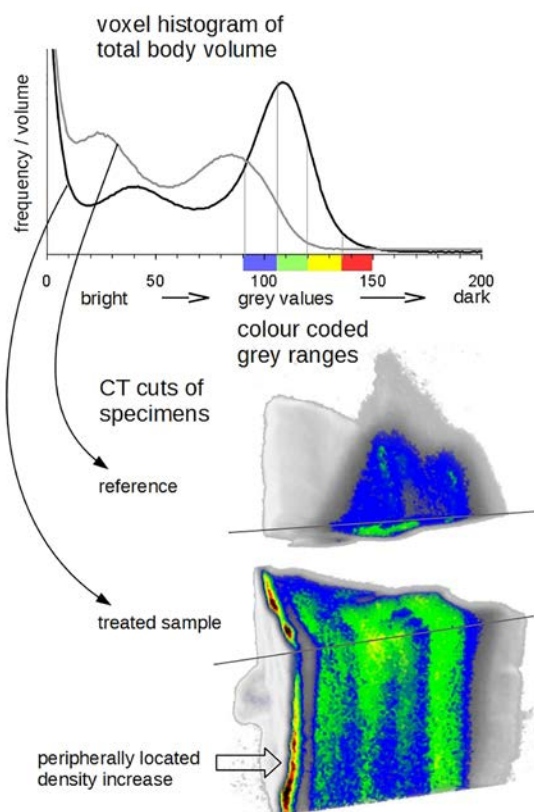


Figure 2: Histograms and corresponding CT reconstructions.

R. Morak¹, S. Braxmeier², C. Balzer², L. Ludescher¹, F. Putz³, S. Busch⁴, N. Hüsing³, G. Reichenauer², O. Paris¹

¹Institut für Physik, Montanuniversität Leoben, Leoben, Austria; ²Bavarian Center for Applied Energy Research, Würzburg, Germany; ³Chemistry and Physics of Materials, Paris-Lodron University of Salzburg, Salzburg, Austria; ⁴German Engineering Materials Science Centre (GEMS) at MLZ, Helmholtz-Zentrum Geesthacht GmbH, Garching, Germany

Nanoporous materials play an important role in many applications such as catalysis, drug delivery, gas separation, or energy storage. Consequently, the synthesis of tailored materials with large surface area, well-controlled pore size and shape, and designed chemical functionalities is the subject of intense research activity worldwide. As a side effect, the adsorption and condensation of gases and vapours in the nanopores lead to a mechanical deformation of the whole porous scaffold, with the strain amplitude ranging from < 0.1 % to several 10 %, depending on the type of material. This effect may have consequences for the mechanical stability, such as irreversible volume changes or even severe damage. However, it also affords the opportunity to design novel types of sensors or actuators based on adsorption-induced deformation.

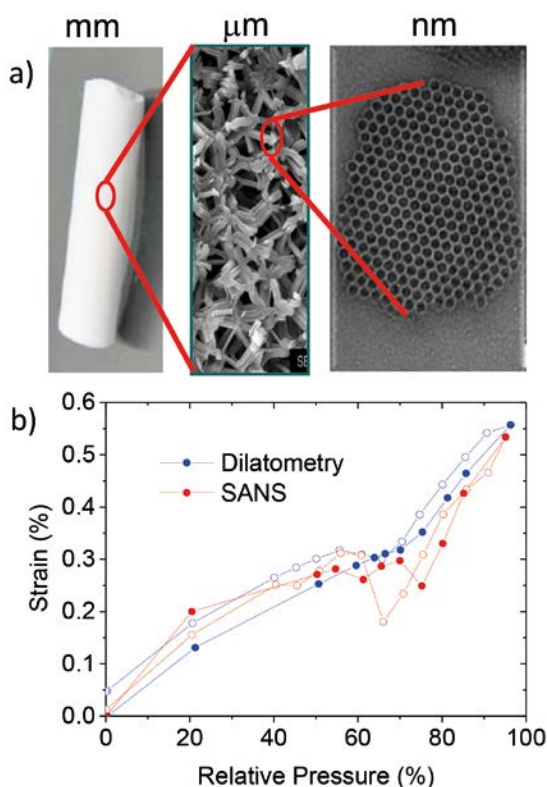


Figure 1: a) Hierarchically organized silica monolith (left) with an isotropic network of struts on the micron scale (middle) and hexagonally ordered cylindrical mesopores on the nanometer scale (right). b) Monolith deformation (blue) and radial strut deformation (red) as a function of relative water vapour pressure. Full symbols denote the adsorption, and open symbols the desorption branches.

In an international project jointly funded by the Austrian (FWF) and the German (DFG) Science Foundations, we investigated silica monoliths with hierarchical porosity (Fig. 1a). The material consists of a network of struts forming macropores ($\approx 1 \mu\text{m}$, Fig. 1a, middle). Each strut comprises well-ordered cylindrical mesopores of about 10 nm diameter, arranged in parallel on a hexagonal lattice (Fig. 1a, right). To provide experimental data for quantitative strain modelling, we applied two complementary in-situ methods. While dilatometry, being particularly sensitive to a length change of the struts, gives the macroscopic deformation of the whole sample, small-angle neutron scattering (SANS) provides the pore lattice strain and, thus, the radial deformation of the struts. The experiments were performed at the SANS-1 instrument at MLZ using water as the adsorbate, its scattering length density being adjusted to zero by using a $\text{H}_2\text{O}/\text{D}_2\text{O}$ mixture. Hence, in contrast to X-rays, the changes observed in the coherent neutron scattering during water adsorption are not influenced by changes in scattering contrast, and can therefore be directly related to the deformation of the porous silica. In addition, the strong incoherent neutron scattering from hydrogen allows the quantitative water uptake (the adsorption isotherm) to be determined.

A custom-designed in-situ sample cell allowed simultaneous recording of SANS and dilatometric data as a function of relative water vapour pressure. Comparison of their strain isotherms (Fig. 1b) provided new insights into the axial and radial components of the adsorption-induced deformation of cylindrical pores, allowing experimental validation of recent theoretical models. The data furthermore revealed the strong impact of micropores within the mesopore walls on the deformation amplitude. Finally, we recently synthesized promising new materials where the struts (Fig. 1a, middle) show a macroscopic preferred orientation. This permits, in principle, an anisotropic deformation at the macroscopic level as well, which is the last missing link in the quest for actuators based on this principle.

[1] R. Morak et al., *Quantifying adsorption-induced deformation of nanoporous materials on different length scales*; *J. Appl. Crystallogr.* 50 (5), 1404 (2017)

N. Paul¹, J. Wandt², S. Seidlmayer¹, S. Schebesta³, M. J. Mühlbauer^{1,4,5}, O. Dolotko¹, H. A. Gasteiger², R. Gilles¹

¹Heinz Maier-Leibnitz Zentrum (MLZ), Technical University of Munich (TUM), Garching, Germany; ²Chair of Technical Electrochemistry, Technical University of Munich (TUM), Garching, Germany; ³VW-VM Forschungsgesellschaft mbH & Co. KG, Ellwangen, Germany; ⁴Institute for Applied Materials (IAM), Karlsruhe Institute of Technology (KIT), Eggenstein-Leopoldshafen, Germany; ⁵Helmholtz-Institute Ulm for Electrochemical Energy Storage (HIU), Karlsruhe, Germany

Anodes in Li-ion cells

Li-ion batteries are not only popular in portable consumer electronics but are also spreading into new markets such as electric vehicles and grid storage systems, where long battery lifetimes are crucial. Therefore, batteries consisting of lithium iron phosphate (LFP) cathode and graphite anode, typically used in grid storage systems, aspire for alternative electrode materials that provide longer lifetimes. We compare the performance of two prospective anode materials and report that mesocarbon microbead (MCMB) is a better alternative to needle coke (NC) for Li-ion cells [1].

Different aging behaviour

Fig. 1 shows the discharge capacities of the LFP/graphite cells as a function of cycle number. The MCMB cell (black line) shows a linear capacity fade, with a relative capacity loss of 8 %. In contrast, the capacity fading rate for the NC cell (green line) is substantially higher during the initial 1000 cycles, before gradually leveling off to a capacity fading rate which is similar to the MCMB cells, resulting in an overall relative capacity loss of 23 %.

Morphology of pristine materials

The anode powders, shown in the inset of Fig. 1, display quite different shapes. Mesocarbon microbead consists of homogeneously distributed spherical particles whereas needle coke consists of anisotropic flake shaped particles with a broad size distribution. These differing morphologies result in dissimilar ion transport paths or different tortuosities, when these materials are used as electrodes.

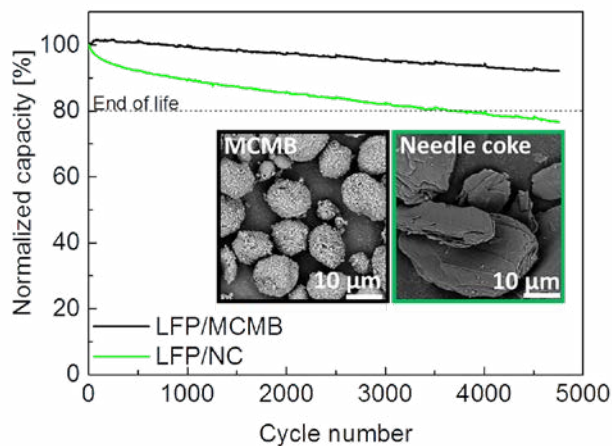


Figure 1: Discharge capacities of the cells as a function of cycle number. Inset shows SEM images of the pristine MCMB and NC powders.

Li inventory in cells containing either MCMB or NC

Identical cells were prepared, differing only in the choice of anode material. Upon storage, the capacity of the needle coke cells decreases by 11 %, showing that the cell suffers significant calendar aging. In contrast, the mesocarbon microbead cell shows no calendar aging. Moreover, the observed formation and cycling losses are in excellent agreement with the active lithium inventory determined by neutron diffraction from the $\text{LiFePO}_4 / \text{FePO}_4$ ratio and the $\text{LiC}_6 / \text{LiC}_{12}$ ratios (Fig. 2), meaning that active lithium loss accounts for the entire capacity loss of the stored and cycled cells. Other aging mechanisms such as structural degradation or deactivation of the electrodes are ruled out, as no LiFePO_4 is observed in the charged cells and no lithiated graphite phases are observed in the discharged cells. Mesocarbon microbead anodes offer excellent structural stability and a longer lifetime compared to needle coke anodes.

[1] N. Paul et al., *Aging behaviour of lithium iron phosphate based 18650-type cells studied by in situ neutron diffraction*, *J. Power Sources* 345, 85 (2017)

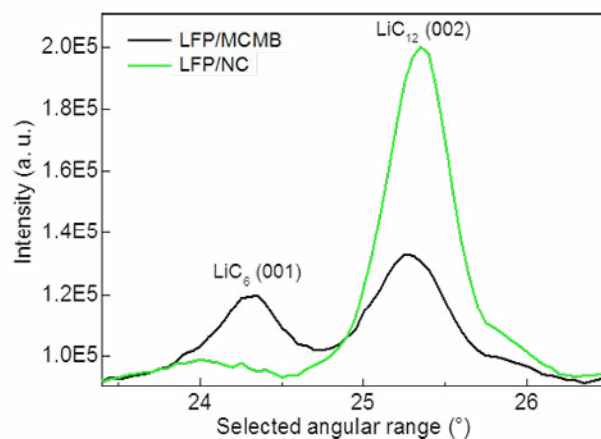


Figure 2: Selected regions of the neutron diffractograms in the fully charged state of the cells.

D. Kumar¹, K.S. Nemkovski², Y. Su², C. Rath¹

¹School of Materials Science and Technology, Indian Institute of Technology (BHU), Varanasi, India; ²Jülich Centre for Neutron Science (JCNS) at MLZ, Forschungszentrum Jülich GmbH, Garching, Germany

The coexistence and coupling of magnetic and ferroelectric ordering observed in multiferroic materials such as CoCr_2O_4 has attracted considerable attention. In the magnetic transition in bulk CoCr_2O_4 , the transitions are characterized by a paramagnetic to ferrimagnetic transition at the Curie temperature T_C , a ferrimagnetic to spiral transition at T_S , and a lock-in transition at T_L . In this study, the magnetic transitions in Fe-doped $\text{CoFe}_{0.1}\text{Cr}_{1.9}\text{O}_4$ nanoparticles with sizes between 10 and 50 nm are investigated using polarized neutron scattering at the DNS instrument.

Temperature dependent magnetic Bragg peaks were measured in detail along three orthogonal directions by spin flip scattering in the range of 3 K to 110 K (Fig. 1). In 10 and 50 nm particles, the fundamental reflections are coherent Bragg reflections up to 90 K. At 110 K, the intensity of the (111) reflection diminishes to the background level. This indicates that the ferrimagnetic component exhibits long-range order below 110 K. With decreasing temperature from 110 K, the (111) reflection in 10 nm particles is found to be very broad and asymmetric, whereas, in 50 nm particles, we observed sharp (111) reflection and an additional satellite peak below 50 K. The intensity of the (111) peak gradually increases upon cooling, a change in slope occurring at around 26 K in 10 nm particles. A slight decrease in intensity at T_S is evidence of the tilting of the magnetic moment. In contrast, to 50 nm particles, the integrated intensity increases sharply while cooling from 110K and shows two clear peaks at around T_C and T_S . Apparently, the magnetic phase transitions are continuous in 10nm particles. Due to the broad and asymmetric nature of the (111) reflection for 10 nm particles, we have deconvoluted the (111) into two peaks where the lower Q peak corresponds to the fundamental, and the latter is the satellite peak. Although the intensity of the satellite peak is found to be very weak, we observe a clear change in slope below 26 K, indicating a short range spiral order. In 50 nm particles, the satellite peak dominates over the fundamental peak below 50 K. With a decrease in temperature, the sharp increase in intensity of the peak flattens at T_S and shows a kink at $T_L \sim 10$ K, i.e. the lock-in-temperature. This implies that the spiral component fluctuates dynamically, retaining the correlation above T_S .

The half width at half maximum (HWHM) of the fundamental and satellite magnetic peak in both samples shows that as the temperature decreases, the correlation length ξ , which is about 0.71 nm at 35 K increases up to 3.91 nm at 3.5 K in 50 nm particles. However, ξ does not change significantly in 10 nm particles. The correlation length in 50 nm particles is higher than the CoCr_2O_4 , corroborating the weak magnetic frustration in B-site due to the substitution of Fe in place of Cr. In accordance with the theoretical prediction, the spiral order observed in our case is commensurate, which could be due to surface defects. Moreover, we confirm that the long range ferrimagnetic order is preserved in both particles sizes, spiral ordering is found to be sharp and short range in 50 nm and is found to be diffused in 10 nm particles [1]

[1] D. Kumar et al., *Size-dependent magnetic transitions in $\text{CoFe}_{0.1}\text{Cr}_{1.9}\text{O}_4$ nanoparticles studied by magnetic and neutron-polarization analysis*; *Nanotechnology* 27, 175702 (2016)

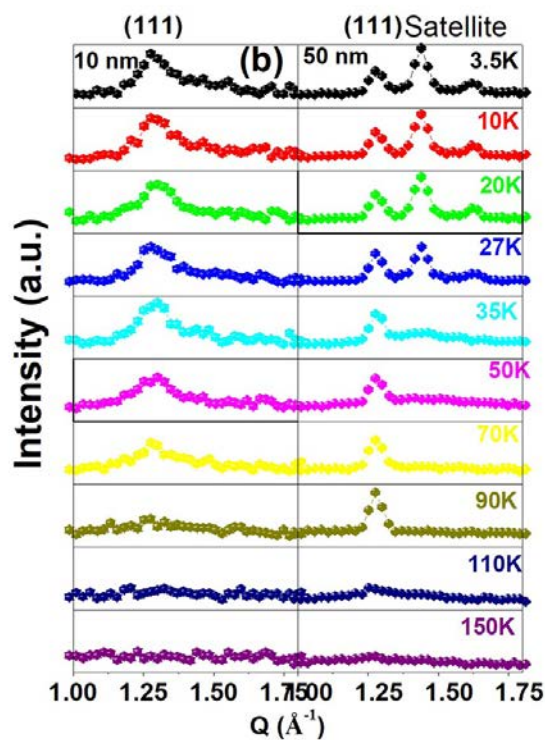


Figure 1: Temperature dependence polarized neutron scattering data for 10 nm and 50 nm particles.

V. Zinth¹, C. von Lüderts², J. Wilhelm², S. V. Erhard², M. Hofmann¹, S. Seidlmayer¹, J. Rebelo-Kornmeier¹, W. Gan³, A. Jossen², R. Gilles¹

¹Heinz Maier-Leibnitz Zentrum (MLZ), Technical University of Munich (TUM), Garching, Germany; ²Institute for Electrical Energy Storage Technology (EES), Technical University of Munich (TUM), München, Germany; ³German Engineering Materials Science Centre at MLZ, Helmholtz-Zentrum Geesthacht GmbH, Garching, Germany

Lithium gradients forming in the graphite anode of a commercial 18650-type lithium-ion battery during discharge and the associated relaxation processes after discharge were monitored in situ using neutron diffraction [1], measured at the STRESS-SPEC instrument at the MLZ.

The experiments reveal the coexistence of up to four different $\text{Li}_{1-x}\text{C}_y$ phases with different lithium contents during discharge. As shown in Fig. 1, diffraction peaks of the different $\text{Li}_{1-x}\text{C}_y$ phases are visible simultaneously. During the subsequent relaxation phase, after the discharge process had been stopped, the relative intensity of the peaks was still changing, indicating that phase equilibration towards a phase with mean lithium content was taking place. At room temperature ($\approx 28^\circ\text{C}$) the inhomogeneity during and after discharge is more pronounced for higher rates (1C vs. C/2), although the observed and observable maximum inhomogeneity might be somewhat influenced by the different depth of discharge. The time-frame for relaxation before this inhomogeneity has levelled out is within the range of 20 – 40 min. At low temperatures (-20°C), inhomogeneity is still observed even during slow C/10 discharge and the subsequent equilibration processes are extremely slow and not complete even after 11 h. Phase equilibration processes and inho-

mogeneity are presumed to occur due to slow lithium diffusion in the solid phase, which prevents full delithiation of the graphite particles. These observations can be explained by a model, which allows faster delithiation of the graphite particles as compared to the equilibration of the resulting lithium gradient by lithium diffusion within the solid phase during discharge. It also appears that lithium deintercalation is faster than intercalation and, thus, a higher discharge than charge rate can be applied at low temperatures before inhomogeneity is observable.

Neutron diffraction is a powerful tool to study anode inhomogeneity during operation and relaxation in commercial 18650 type batteries. This approach will be useful in further studies for anode optimization in high power and low temperature applications. Further investigation of these kinetic effects could be very important when neutron diffraction is applied to large format batteries and combined with measurements of the diffusion and transport properties at the electrode level.

[1] V. Zinth et al., *Inhomogeneity and relaxation phenomena in the graphite anode of a lithium-ion battery probed by in situ neutron diffraction*; *J. of Power Sources* 361, 54 (2017)

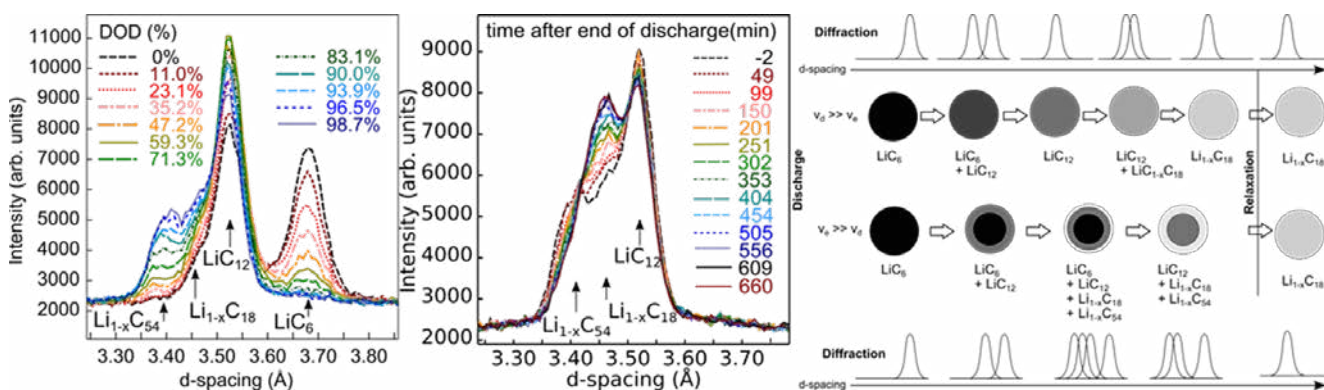


Figure 1: left) Exemplary diffraction data measured during -20°C discharge; middle) relaxation at -20°C ; right) illustration model showing how faster lithium extraction from particles can induce phase inhomogeneity observable by neutron diffraction;

B. Starke¹, S. Seidlmayer², S. Jankowsky¹, O. Dolotko², R. Gilles² and K.-H. Pettinger¹

¹University of Applied Sciences Landshut, Landshut, Germany; ²Heinz Maier-Leibnitz Zentrum (MLZ), Technical University of Munich, Garching, Germany

LiFePO₄ (LFP) is a superior cathode material for lithium-ion batteries. It can be produced at low cost, is environmentally friendly and provides high operational safety. In this study, various morphologies of LFP (primary particles (PP) and secondary agglomerates (SA) as shown in Fig. 1) and their performance characteristics have been investigated in the context of water- and solvent-based processing. For water-based cathodes, eco-friendly carboxymethyl cellulose (CMC) was used as a binder. Following common industrial procedures, solvent-based cathodes were obtained by using the organic solvent N-methyl-2-pyrrolidone (NMP) combined with polyvinylidene fluoride (PVDF) as a binder.

Via neutron and X-ray diffraction performed at the SPO-DI instrument and the X-ray diffractometer at the Materials Science Laboratory of the MLZ, it was verified that the structural properties of both morphologies are insensitive to water-based processing. The neutron and X-ray diffraction patterns are shown in Fig. 2: Comparison of the X-ray and neutron diffraction patterns of LiFePO₄ (LFP) samples studied: (a) Neutron diffraction data of pristine LFP-powder ($\lambda = 1.5482 \text{ \AA}$); (b) X-ray diffraction patterns of prepared cathodes ($\lambda = 0.70932 \text{ \AA}$).

With regard to electrochemical properties, water-based processing of PP leads to reduced performance. Since the structure of LFP itself remains unaffected, this is very likely to be caused by the partial loss of carbon coating at the LFP

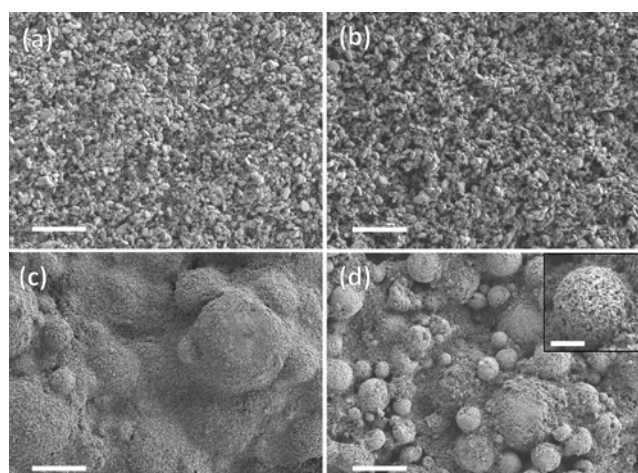


Figure 1: FE SEM micrographs of the prepared cathodes: (a) PP_{H₂O} cathode (scale bar: 4 μm); (b) PP_{NMP} cathode (scale bar: 4 μm); (c) SA_{H₂O} cathode (scale bar: 20 μm); (d) SA_{NMP} cathode (scale bar: 20 μm); inset in (d) shows a secondary agglomerate without conductive carbon covering (scale bar: 3 μm).

particle surface due to simultaneous contact with water and high mechanical stress. SA did not show any such shortcomings following water-based processing. The reason may be found in the fact that the majority of LFP particles are located inside the agglomerates and thus protected from shear force and mechanical stress during slurry preparation. Comparing the performance of cathodes produced with SA via the water- or organic solvent-based process, identical long-term capacity fading can be observed. The results of this study show that the use of secondary agglomerates holds great potential and demonstrate their suitability for high energy applications with moderate (dis-) charge currents. This allows the application of water-based processing for industrial use and would greatly improve the environmental footprint of battery production since it would make the expensive treatment of the toxic solvents emitted and protection of workers superfluous. This study demonstrates that, if secondary agglomerates are used, much cheaper water-based processing, as compared to the currently established NMP solvent, leads to electrodes with the same performance. Therefore the use of less ecologically critical and more ecofriendly binders are an economic and environmentally friendly solution for battery production.

[1] B. Starke et al., *Influence of Particle Morphologies of LiFePO₄ on Water- and Solvent-Based Processing and Electrochemical Properties*; *Sustainability* 9, 888 (2017)

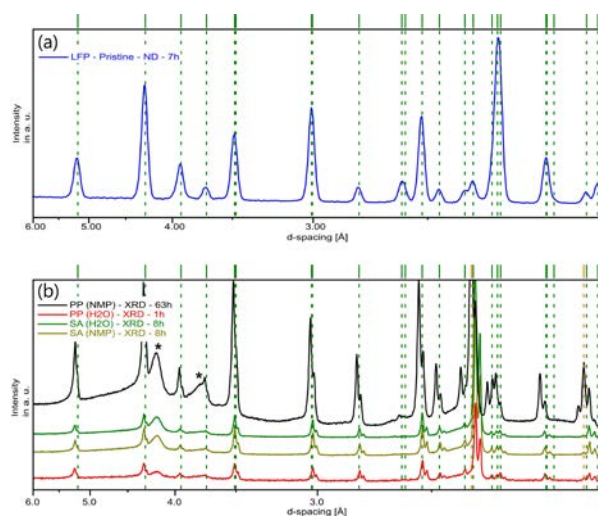


Figure 2: Comparison of the X-ray and neutron diffraction patterns of LiFePO₄ (LFP) samples studied: (a) Neutron diffraction data of pristine LFP-powder ($\lambda = 1.5482 \text{ \AA}$); (b) X-ray diffraction patterns of prepared cathodes ($\lambda = 0.70932 \text{ \AA}$)

A. Viani¹, K. Sotiriadis¹, I. Kumpová¹, L. Mancini², M.-S. Appavou³

¹Institute of Theoretical and Applied Mechanics AS CR, Centre of Excellence Telč, Telč, Czechia; ²Elettra-Sincrotrone Trieste S.C.p.A., Trieste, Basovizza, Italy; ³Jülich Centre for Neutron Science (JCNS) at MLZ, Forschungszentrum Jülich GmbH, Garching, Germany

Zinc phosphate cement (ZPC) is one of the oldest dental cements. It is still widely employed worldwide thanks to its successful track record, and it is generally considered the “gold standard” of the restorative materials for dentistry.

Different microstructure for clinical practice

ZPC hardens after mixing two components: a solution of phosphoric acid and a ZnO powder. Cement properties are ‘tuned’, acting on both the liquid composition and the reactivity of the powder. In clinical practice, the liquid to solid weight ratio (l/s) is optimized for specific applications, resulting in cements with different microstructure and mechanical properties. ZPCs are highly defect-limited materials and their porosity affects their performance. The pore surface area per unit volume, which depends on cement porosity and microstructure, controls to a large extent the rate of the chemical and/or physical-chemical reactions. In fact, important properties, such as dissolution/erosion, take up or release of fluoride (added to improve the resistance to caries), are essentially surface-dependent.

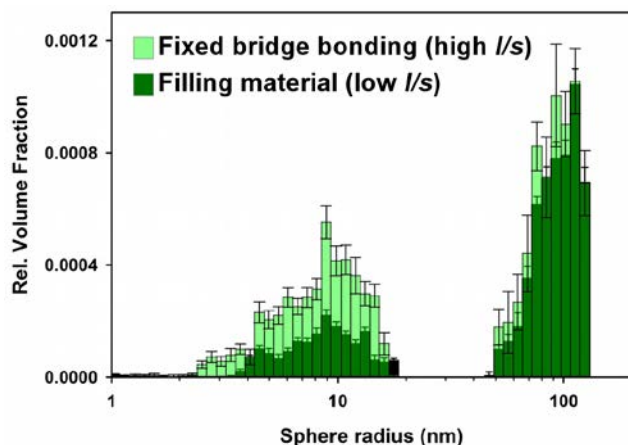


Figure 1: Volume-weighted size distributions of pores obtained from the fit of the SANS curves of ZPC samples using a sphere model for the pore shape (modified from [1]).

The microstructure of two ZPC formulations of commercial cement have been investigated combining small angle neutron scattering (SANS) and X-ray computed tomography (XCT) [1]. In this way, a wide range of pore sizes has been accessed in a totally non-invasive fashion, including the ‘isolated’ pores not detectable using other techniques.

SANS at KWS-2

SANS data were collected at the KWS-2 instrument operated by JCNS at the Heinz Maier-Leibnitz Zentrum MLZ. The fit of the SANS curves with the Monte Carlo method indicated a bi-modal distribution with two populations of pores, the size being centered at around 20 and 200 nm (Fig. 1). The surface area per unit volume is largely contributed by the finest porosity, highlighting the importance of SANS derived values. The cement with higher l/s (recommended as fixed bridge bonding material) showed higher porosity and lower mechanical strength with respect to that recommended as filling material (with lower l/s). Pores, sub-spherical in shape, developed essentially through the segregation of liquid during the setting reaction, therefore, the contribution of air entrapment during mixing was negligible. The lower specific surface area of the formulation recommended as filling material makes the cement less active with respect to fluoride release/uptake (which is surface dependent). At the same time, it should exhibit a higher dissolution rate owing to the higher content of unreacted ZnO powder. There are indications that the porosity evolves with time, albeit very slowly, with consequences for the life span of the restorations.

[1] A. Viani et al., *Microstructural characterization of dental zinc phosphate cements using combined small angle neutron scattering and microfocus X-ray computed tomography*; *Dent. Mater.* 33, 402 (2017)

T. Weber^{1,2}, B. Roessli³, C. Stock⁴, T. Keller^{5,2}, K. Schmalzl⁶, F. Bourdarot⁷, R. Georgii², R. A. Ewings⁸, R. S. Perry^{8,9}, P. Böni¹

¹Department of Physics E21, Technical University of Munich (TUM), Garching, Germany; ²Heinz-Maier-Leibnitz-Zentrum (MLZ), Technical University of Munich (TUM), Garching, Germany; ³Laboratory for Neutron Scattering and Imaging (LNS), Paul Scherrer Institute (PSI), Villigen, Switzerland; ⁴School of Physics and Astronomy and Centre for Science at Extreme Conditions, University of Edinburgh, United Kingdom; ⁵Max-Planck-Institute for Solid State Research, Stuttgart, Germany; ⁶Jülich Centre for Neutron Science (JCNS), Forschungszentrum Jülich GmbH, Outstation at Institut Laue-Langevin, Grenoble, France; ⁷Département de Recherche Fondamentale sur la Matière Condensée, SPSMS/MDN, CEA Grenoble, France; ⁸ISIS Pulsed Neutron and Muon Source, STFC Rutherford Appleton Laboratory (RAL), Didcot, Oxon, United Kingdom; ⁹London Centre for Nanotechnology and UCL Centre for Materials Discovery, University College London, London, United Kingdom

Spinel vanadates, as shown in Fig. 1, are chemical compounds possessing electrons that are shared among three equivalent orbitals of the vanadium atoms. Such an orbital degeneracy is an unfavourable configuration which the crystal tries to overcome by geometrically distorting and, thus, changing the energy levels of the orbitals with respect to one another. In the spinel MgV_2O_4 , these distortions take place at a temperature $T \approx 63$ K and – since the vanadium atoms are in a special arrangement called a “pyrochlore lattice” – lead to a collective motion of the atoms in the crystal, a “cooperative Jahn-Teller effect”.

In a collaboration between the MLZ (instruments MIRA and TRISP), the Institut Laue-Langevin in France (IN22) and the Paul-Scherrer-Institut in Switzerland (EIGER) we measured the phonons in the vicinity of the Jahn-Teller transition. Here, we found an anomalous softening of the phonons accompanied by a “damping”, i.e. a decrease in their lifetime restricted to momentum transfers q between the Brillouin zone centre (labelled Γ) and the border (labelled K). The measurements are depicted in Fig. 2.

The observed simultaneous softening and damping of the phonons indicates a coupling between the phonon modes and other available degrees of freedom. Possible mechanisms for such an interaction are the interactions of the phonon with the crystal field, or with charge fluctuations.

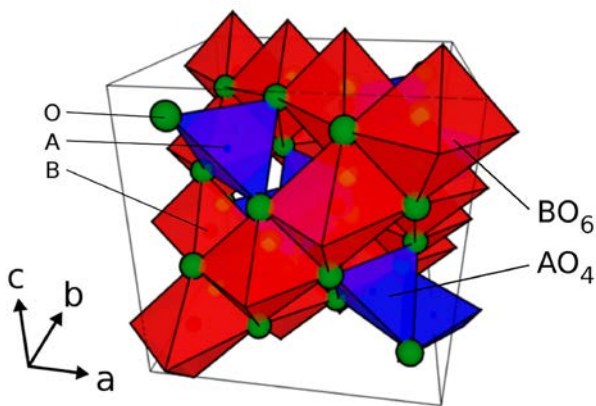


Figure 1: In a spinel, the metallic ions, here: A = Mg, B = V, are in a tetrahedral AO_4 and octahedral BO_6 coordination, respectively. The edge-sharing BO_6 octahedra are responsible for the cooperative nature of the Jahn-Teller effect.

For the first possibility, we note that the crystal-electric field in the octahedral environment causes a spin-orbit splitting of the degenerate ground states of vanadium. The energy of such a splitting is of the same order as the energy of the phonons where the softening was observed, thus enabling a coupling. Such a mechanism would, however, lead to a true soft mode with vanishing energy, not merely a softening.

For the second possibility, we compare our results to those of F. Weber et al. (Ref. 71 in [1]). That study identified a phonon softening similar to ours in a metallic manganite. They attributed the observed anomalies to an interaction between the electrons and the phonons for momenta q close to the Fermi surface. While the results are similar, the mechanism in our case cannot be the same since MgV_2O_4 is not a metal and hence does not possess a Fermi surface. A theoretical work (Ref. 81 in [1]) finds strong charge fluctuations in MgV_2O_4 whose coupling to the acoustic modes is a likely contender to explain the observed effects.

[1] T. Weber et al., *Transverse acoustic phonon anomalies at intermediate wave vectors in MgV_2O_4* ; *Phys. Rev. B* 96, 184301 (2017)

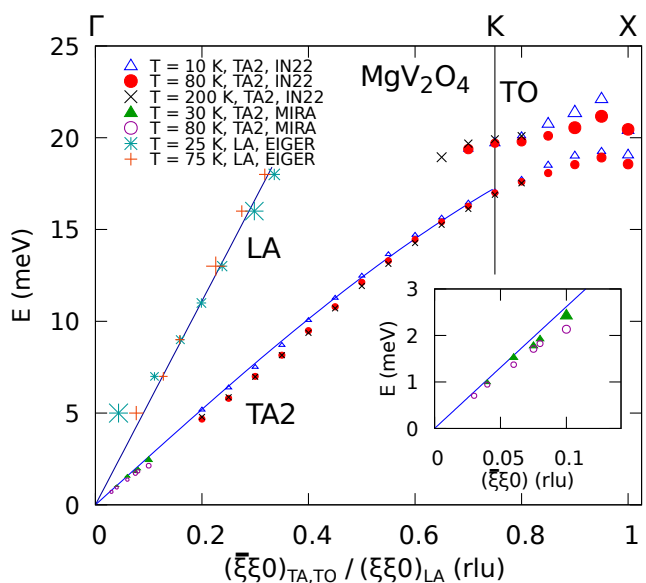


Figure 2: The transverse-acoustic (“TA2”) phonon dispersion shows a marked softening for momenta between Γ and K. No such effect could be observed for either the other transverse phonon branches (not shown) nor for the longitudinal-acoustic (“LA”) branch.

S. Mühlbauer¹, G. Brandl^{2,3}, M. Månsson⁴, M. Garst⁵

¹Heinz Maier-Leibnitz Zentrum (MLZ), Technical University of Munich, Garching, Germany; ²Jülich Centre for Neutron Science (JCNS) at MLZ, Forschungszentrum Jülich GmbH, Garching, Germany; ³Department of Physics E21, Technical University of Munich, Garching, Germany; ⁴Materials Physics, KTH Royal Institute of Technology, Stockholm Kista, Sweden; ⁵Institut für Theoretische Physik, Technische Universität Dresden, Dresden, Germany

Spin-orbit coupling (SOC) in noncentrosymmetric magnets leads to the Dzyaloshinskii-Moriya interaction (DMI) that favors incommensurate cycloidal or helical magnetic order. In the limit of weak SOC, the associated wavelength becomes large. As a consequence, magneto-crystalline anisotropies are less effective in fixing the orientation of the helices. Depending on the symmetry of the material, the energies of the helices might then be almost degenerate for orientations of their wave vectors k that belong to manifolds in k -space, e.g., a sphere, which can qualitatively influence the phase transition. When approaching the phase transition from high temperatures, magnons soften on this manifold and the associated large phase space gives rise to large entropy that might drive the phase transition to first order, known as the Brazovskii transition. Recently, experimental evidence has shown that such a scenario is realized in the cubic helimagnet MnSi and other cubic helimagnets with the same symmetry, with the magnons softening on a sphere in k -space.

It is an open question as to whether such a scenario is also realized in systems of lower symmetry. A promising candidate is the noncentrosymmetric tetragonal antiferromagnet (AF) $\text{Ba}_2\text{CuGe}_2\text{O}_7$. Below $T_N \approx 3.05\text{K}$, an incommensurate, long-range AF cycloidal spin structure is caused by the DMI. Nearest neighbor AF exchange in the (a,b) -plane is the dominant magnetic interaction. The coupling between adjacent planes is weak, essentially leading to a system of

weakly coupled 2D-layers. The transition between the zero-field paramagnet and the cycloidal AFM order is weakly first-order. Similar to MnSi, the specific heat shows a sharp latent heat that sits on top of a broader peak.

In the present work [1], we performed neutron diffraction experiments on $\text{Ba}_2\text{CuGe}_2\text{O}_7$ on the triple axis spectrometer TASP at PSI and the SANS-1 beamline at the MLZ to study the critical magnetic fluctuations. We demonstrate that, close to the critical temperature T_N , magnetic intensity indeed accumulates on a manifold in momentum space which corresponds to a ring in the (a,b) -plane. This suggests that magneto-crystalline anisotropies are comparatively small. These observations fulfill the preconditions for a Brazovskii type transition. However, the temperature dependence of the inverse correlation length, $\kappa(T)$, is not in agreement with the predictions of the Brazovskii theory: We find that $\kappa(T)$ does not change its curvature, but is always convex in an extended temperature range above T_N . We attribute the convexity of $\kappa(T)$ to the effective low dimensionality of fluctuations due to the weak coupling between the layers.

[1] S. Mühlbauer et al., *Formation of incommensurate long-range magnetic order in the Dzyaloshinskii-Moriya antiferromagnet $\text{Ba}_2\text{CuGe}_2\text{O}_7$, studied by neutron diffraction*; *Phys. Rev. B* 96, 134409 (2017)

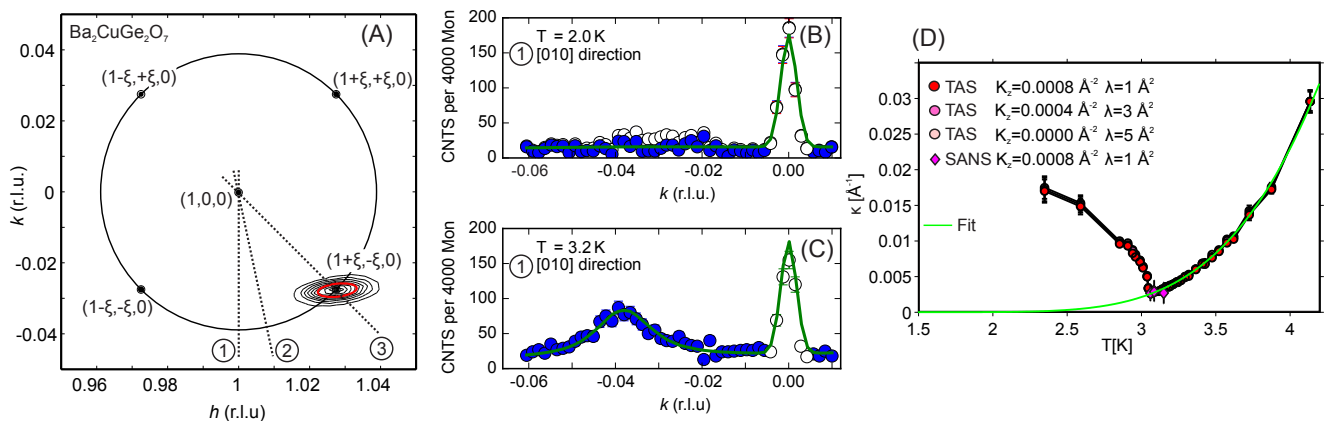


Figure 1: (A): Schematic depiction of the four incommensurate AF satellite reflections of $\text{Ba}_2\text{CuGe}_2\text{O}_7$, centered at the Néel point $(1, 0, 0)$. The contour lines denote the instrumental resolution as measured on TASP. The dotted lines denote the different scans in reciprocal space. Panels (B) and (C): Scans along the $[0, 1, 0]$ direction for temperatures below (B) and just above (C) the transition at T_N . A broad peak at $[-0.04, 1, 0]$ indicates a cut through the fluctuations on the ring. Blue filled points indicate magnetic intensity; the green line represents a global fit. (D) Temperature dependence of the inverse correlation length $\kappa(T)$ of the ring for different sets of fitting parameters.

V. Peçanha-Antonio^{1,2}, E. Feng¹, Y. Su¹, V. Pomjakushin³, F. Demmel⁴, L.-J. Chang⁵, R. J. Aldus¹, Y. Xiao⁶, M. R. Lees⁷, T. Brückel^{6,1}

¹Jülich Centre for Neutron Science (JCNS) at MLZ, Forschungszentrum Jülich GmbH, Garching, Germany; ²Department of Physics, Technical University of Munich, Garching, Germany; ³Laboratory for Neutron Scattering and Imaging (LNS), Paul Scherrer Institute, Villigen, Switzerland; ⁴ISIS Facility, Rutherford Appleton Laboratory, Chilton, United Kingdom; ⁵Department of Physics, National Cheng Kung University, Tainan, Taiwan; ⁶Jülich Centre for Neutron Science (JCNS) and Peter Grünberg Institut (PGI), Forschungszentrum Jülich GmbH, Jülich, Germany; ⁷Department of Physics, University of Warwick, Coventry, United Kingdom

The pyrochlore compound $\text{Yb}_2\text{Ti}_2\text{O}_7$ is well known for displaying exotic magnetism. Despite a sharp heat capacity anomaly, which indicates that a phase transition takes place at $T_c \sim 280$ mK, until very recently this compound was believed not to display long-range magnetic order in its low-temperature ground state. Experiments performed at the instrument DNS at the MLZ helped us to show that the compound does present magnetic long-range order at temperatures below T_c , even though its ordered moment is much reduced from that expected. The experiments performed with both polarized and unpolarized neutrons allowed us, firstly, to observe strong neutron beam depolarization upon cooling from 600 mK down to 100 mK (Fig. 1). It suggests the development of ferromagnetic domains in the sample below the phase transition temperature. The unpolarized neutron diffraction data (Fig. 2) indeed confirm that the spin structure in the compound corresponds to that of a quasicollinear ferromagnet (schematic drawing in Fig. 3), unique within the pyrochlore titanate series. The negative downturn at low momentum transfers in Fig. 2 also gives some hints about the persistent spin dynamics coexisting with the long-range order at temperatures as low as 130 mK. A further high-resolution inelastic neutron scattering experiment, performed at ISIS, identifies a significant amount of quasielastic neutron scattering remnant deep in the ordered state. The unusual behaviour of $\text{Yb}_2\text{Ti}_2\text{O}_7$ is not only restricted to elastic or quasielastic scattering; exotic low-energy gapped excitations also take place at temperatures up to at least 2 K, around $7 \cdot T_c$.

[1] V. Peçanha-Antonio et al., *Magnetic excitations in the ground state of $\text{Yb}_2\text{Ti}_2\text{O}_7$* ; *Phys. Rev. B* 96, 214415 (2017)

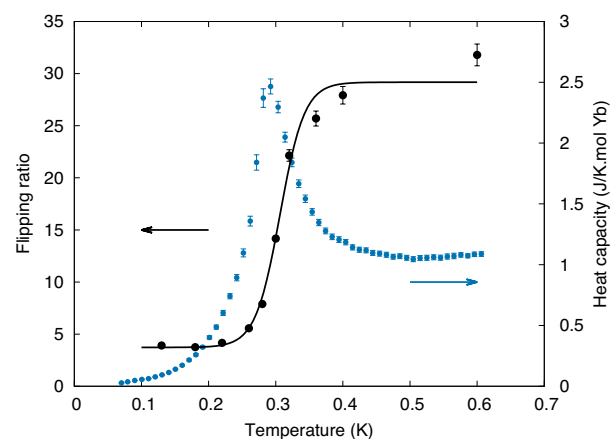


Figure 1: Flipping ratio plotted along with heat capacity as a function of temperature. The drop in the neutron polarization around T_c establishes the ferromagnetic nature of the phase transition. The black line is a guide to the eye.

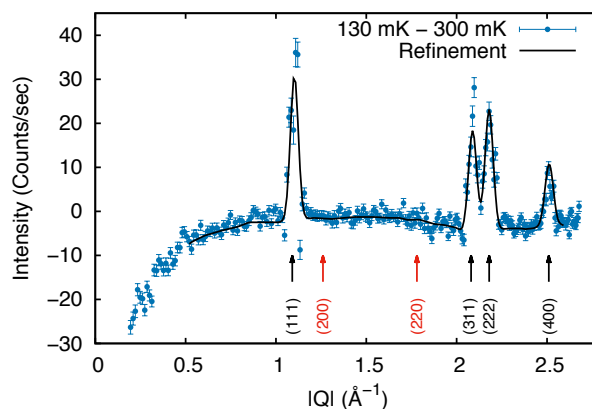


Figure 2: Unpolarised neutron diffraction measurement performed at 300 mK subtracted from the data measured at 130 mK. Representational analysis carried out on the resulting magnetic scattering allows us to identify the magnetic structure as being that of a quasicollinear ferromagnet below T_c . The arrows indicate the position of the magnetic zone centers.

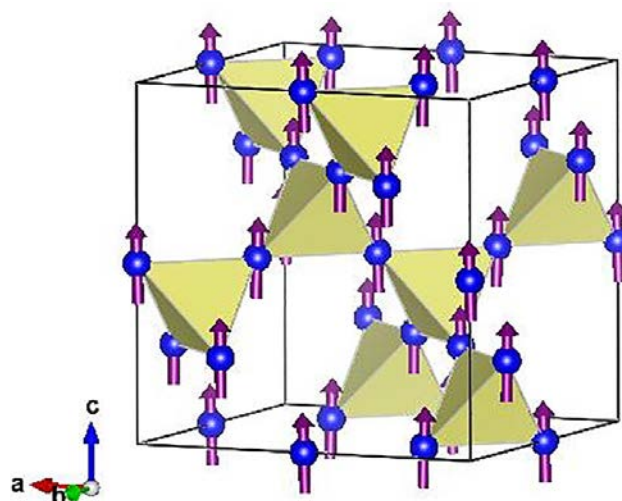


Figure 3: Schematic representation of the ground-state magnetic structure. The arrows indicate the ordered magnetic moment direction of the rare-earth Yb^{3+} in the pyrochlore unit cell.

T. Reimann^{1,2}, M. Schulz^{1,2}, D. F. R. Mildner³, M. Bleuel³, A. Brület⁴, R. P. Harti⁵, G. Benka⁶, A. Bauer⁶, P. Böni², S. Mühlbauer¹

¹Heinz Maier-Leibnitz Zentrum (MLZ), Technical University of Munich, Garching, Germany; ²Department of Physics E21, Technical University of Munich, Garching, Germany; ³NIST Center for Neutron Research, National Institute of Standards and Technology, Gaithersburg, USA; ⁴Laboratoire Léon Brillouin, CNRS-CEA, CEN Saclay, Gif-sur-Yvette, France; ⁵Neutron Imaging and Activation Group, Paul Scherrer Institut, Villigen, Switzerland; ⁶Department of Physics E51, Technical University of Munich, Garching, Germany

Vortex lattices (VL) in type-II superconductors arise in a variety of different configurations e.g., liquid, solid, glassy, and amorphous phases. Their different manifestations are due to the multitude of interactions influencing the vortices: intervortex interaction, correlations with the crystal lattice, thermal activation, pinning, and topological restrictions. Depending on the material, these interactions can be of similar magnitude. The complexity of vortex matter is further compounded by the different length scales of these interactions: while intervortex interactions and crystal lattice correlations determine the vortex spacing and can affect the crystallography of vortex matter, pinning acts collectively on the VL. Finally, geometrical effects cause an inhomogeneous distribution of vortices on a macroscopic scale. At variance with the Ginzburg-Landau (GL) theory, which predicts a pure repulsion of vortices, attractive intervortex interaction is observed in the intermediate mixed state (IMS) of type-II/1 superconductors with small GL coefficient κ , which arises from the energy reduction of partially overlaying vortex cores. The IMS is characterized by microscopic separation into VL domains and field-free areas.

We present an experimental study [1] on the influence of pinning, geometrical barriers, and vortex attraction on the IMS formation in the type-II/1 superconductor niobium. This study is based on the combination of neutron grating inter-

ferometry (nGI at ANTARES, MLZ) with SANS (SANS-1 at MLZ) and USANS (TPA at LLB and BT-5 at NIST); As a model case of a phase separation, the transformation of the homogeneous VL to an inhomogeneous IMS domain structure is examined as a function of cooling, where the VL decomposes at the onset of vortex attraction. Despite the trapping of flux at a freezing transition, a subsequent nucleation of an irregular domain structure characterized by a micrometer correlation length is found at lower temperatures. The results suggest that collective pinning weakens at the threshold from repulsive to attractive vortex-vortex interaction. Moreover, the observed phase separation reveals strong similarities to the process of spinodal decomposition. An increase in the correlation length with increasing field is explained by the competition of the domains' surface tension and the energy associated with the disturbance of the applied field. While the length scale of the IMS is not influenced by pinning, all relevant field scales are reduced compared to pinning free samples. Finally, a pronounced impact of the geometrical barrier is observed.

[1] T. Reimann et al., *Domain formation in the type-II/1 superconductor niobium: Interplay of pinning, geometry, and attractive vortex-vortex interaction*; *Phys. Rev. B* 96, 144506 (2017)

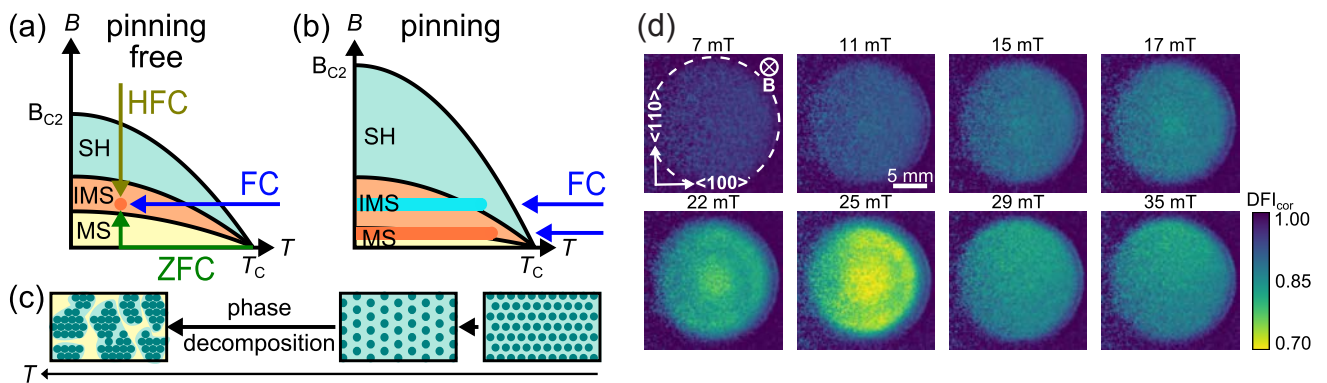


Figure 1: Panels (a), (b): Schematic (B, T) -phase diagram of a type-II/1 superconductor without (a) and with pinning (b) following different cooling paths. SH denotes the Shubnikov phase, IMS and MS denote the intermediate mixed state and the Meissner phase, respectively. (c): Illustration of the phase decomposition of the homogeneous VL to an inhomogeneous IMS domain structure during cooling in a constant, small magnetic field. (d): nGI data showing the distribution of the IMS phase as a function of different magnetic fields, each after field cooling to the base temperature of 4 K. The white dotted line indicates the shape of the sample.

X. Sun¹, E. Feng², A. Klapper¹, Y. Su², K. Nemkovski², H. Bauer³, O. Köhler³, A. Schilman³, W. Tremel³, O. Petracic¹, Th. Brückel¹

¹Jülich Centre for Neutron Science JCNS and Peter Grünberg Institut PGI, JARA-FIT, Forschungszentrum Jülich GmbH, Jülich, Germany; ²Jülich Centre for Neutron Science (JCNS) at MLZ, Forschungszentrum Jülich GmbH, Garching, Germany; ³Institut für Anorganische Chemie und Analytische Chemie, Johannes Gutenberg-Universität Mainz, Mainz, Germany

Magnetic nanoparticles (NPs) have attracted considerable interest for decades due to their potential applications in magnetic data storage, ferrofluidic systems, and nanomedicine. The spin structure of antiferromagnetic (AF) MnO NPs was studied and compared to bulk samples (powder and single crystal) using a combination of magnetometry and neutron scattering. At low temperatures, the zero field cooled (ZFC) magnetization curves of NPs usually show a peak at ca. 25 K (Fig. 1a). However, *no* feature indicating the Néel temperature at 118 K could be found. To confirm the AF order of MnO NPs, polarized neutron scattering was performed using the DNS instrument. Despite the extremely small amount of the sample (50 mg), as well as the hydrogen contained in the oleic acid shell covering the particles, the magnetic (red circles) component was successfully separated from the nuclear coherent (black squares) and spin-incoherent (blue triangles) components using polarization analysis. Here, the expected behaviour of the AF order parameter that vanishes at around 118 K was observed (Fig. 2), in contrast to the magnetometry result. The magnetic behaviour of MnO particles can be explained by a superposition of superparamagnetic-like thermal fluctuations of the AF-Néel vector inside the AF core and a magnetic coupling to a ferrimagnetic (FiM) Mn₂O₃ or Mn₃O₄ shell.

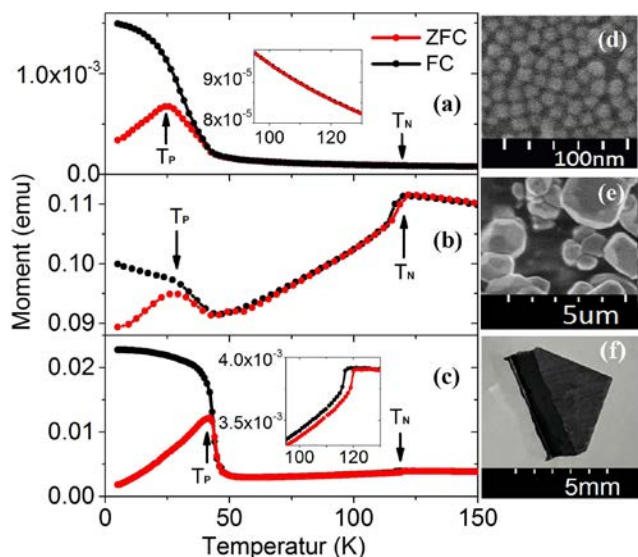


Fig. 1: ZFC/FC curves of (a) 12 nm MnO NPs, (b) MnO powder and (c) MnO single crystal measured at 100 mT. Insets in panel (a) and (c) are enlarged views near the Néel temperature. (d) and (e) show the SEM images of MnO NPs with 12 nm diameter and MnO powder, respectively. (f) shows a photo of one piece of the MnO single crystal.

In order to gain a better understanding of the intrinsic magnetic behaviour of MnO itself, bulk MnO as a powder and single crystals was studied and compared to the results of NPs. Both the magnetometry and polarized neutron diffraction results confirm the PM-to-AF phase transition at T_N . Interestingly, ZFC curves of both types of sample show a peculiar peak at low temperatures similar to the low temperature peak observed in NPs (Fig. 1). For the powder sample, this peak shows behaviour similar to that for the NPs. It is, therefore, likely to be due to the nano-sized particles between or attached to the large powder particles (Fig. 1e). For the single crystal, the low temperature peak is relatively sharp compared to that observed for NPs and powder and bears a greater resemblance to the behaviour of a ferromagnet (FM) or ferrimagnet (FiM). Moreover, the temperature of 40 K agrees with the Curie temperature of Mn₃O₄ (42 K). This peak is not observed in single phase MnO powder after an annealing procedure. We conclude that this peak originates from nanosized particles for powder samples or a small quantity of FiM Mn₂O₃ or Mn₃O₄ impurities at the interfaces between MnO crystal twins, respectively.

[1] X. Sun et al., *Magnetism of monomer MnO and hetero dimer FePt@MnO nanoparticles*; *Phys. Rev. B* 95, 134427 (2017)

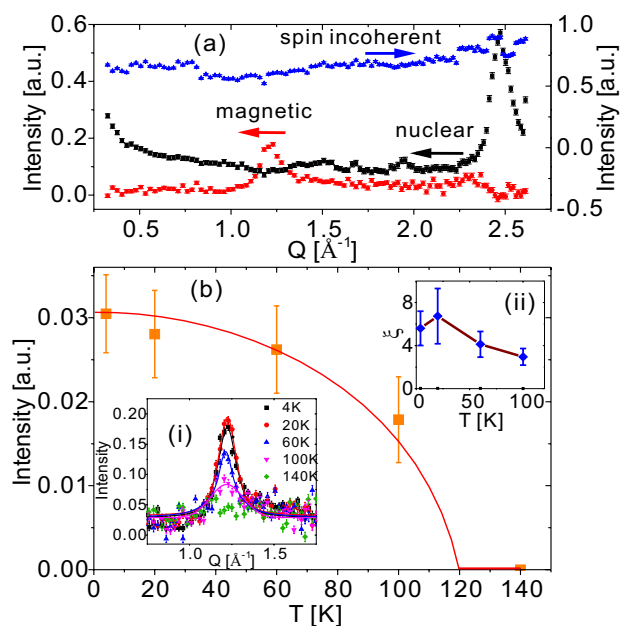


Fig. 2: (a) Separated neutron-scattering contributions of 12 nm MnO NPs from polarized neutron scattering measured at 4 K. (b) Temperature dependence of the integrated intensity of the AF $(1/2, 1/2, 1/2)$ Bragg peak. The red line is a guide to the eye assuming the bulk T_N of 120 K and a continuous transition. The inset (i) in (b) shows the magnetic $(1/2, 1/2, 1/2)$ Bragg peaks at different temperatures. The inset (ii) in (b) displays the magnetic correlation length as a function of temperature.

A. Feoktystov¹, V. M. Garamus², J. Zaloga³, W. Karawacka³, A. Ioffe¹, Th. Brückel⁴, R. Tietze³, C. Alexiou³, S. Lyer³

¹Jülich Centre for Neutron Science (JCNS) at MLZ, Forschungszentrum Jülich GmbH, Garching, Germany; ²Helmholtz-Zentrum Geesthacht GmbH, Geesthacht, Germany; ³Head and Neck Surgery, Section for Experimental Oncology and Nanomedicine (SEON), Department of Otorhinolaryngology, Else Kröner-Fresenius-Stiftung Professorship, University Hospital Erlangen, Germany; ⁴Jülich Centre for Neutron Science (JCNS-2) and Peter Grünberg Institute (PGI-4), JARA-FIT, Forschungszentrum Jülich GmbH, Jülich, Germany

Mitoxantrone (MTO), a potent anti-cancer drug, can be absorbed on functionalized surfaces, such as lauric acid human serum albumin (LA-HSA) coated superparamagnetic iron oxide nanoparticles (SEON^{LA-HSA}) for smart drug delivery. Such MTO-loaded complexes have already shown very promising results in treating cancer in *in vivo* animal models. Since the exact location of MTO loaded to SEON^{LA-HSA} (SEON^{LA-HSA}*MTO) was unknown, small-angle neutron and X-ray scattering (SANS/SAXS) experiments have been performed in H₂O and D₂O, with both regular MTO and partially deuterated MTO (dMTO). SANS contrast variation showed that the initial SEON^{LA-HSA} system consists of multicore particle aggregates, which have an organic shell, and that the adsorption of MTO takes place in the form of separated molecules (there is no supramolecular aggregation of MTO).

Complementary SAXS studies of the SEON^{LA-HSA} concentration series were performed in the range of 0.01 to 1.28 wt.% in respect to the magnetic nanoparticles. We used the fact that the SAXS scattering curve at the lowest concentration (0.01 wt.%) is almost free of any interparticle interaction and obtained the structure factor by dividing the SAXS curve from the most concentrated sample (1.28 wt.%) by the lowest concentration (0.01 wt.%). The resulting structure factors are represented in the Figure. The structure factor decreases more slowly towards smaller q after the addition of the drug, which points to the reduction of the interparticle repulsive interaction in the system. The effect of

possible free salts on the interaction in the samples (Debye screening length variation) was checked and found to be negligible for the difference observed in the structure factors. SANS and SAXS on SEON^{LA-HSA}*dMTO suggest that the dMTO decreases the interaction between clusters i.e., it should be located at the outer shell of SEON^{LA-HSA} clusters (namely at the LA-HSA layer) and a molecular adsorption of dMTO should occur. That is why the interaction between LA-HSA and dMTO has been studied by SAXS in mixtures of LA-HSA and LA-HSA with dMTO (100 µg/ml), where the amount of the constituents corresponded to the SEON^{LA-HSA} sample with magnetic nanoparticles. The SAXS curves obtained from the LA-HSA and LA-HSA*dMTO samples were satisfactory fitted to the model of an oblate ellipsoid of revolution with screened Coulomb interaction. A decrease in the electrical charge of the LA-HSA complex with drug addition was found.

These results show that the addition of MTO to the SEON^{LA-HSA} system leads to a reduction in the interaction of its clusters due to a compensation of surface charge. This leads to a change in cluster-cluster interaction. The location of MTO molecules at the surface of SEON^{LA-HSA} should be considered for further application of such formulations.

[1] J. Zaloga et al., *Studies on the adsorption and desorption of mitoxantrone to lauric acid/albumin coated iron oxide nanoparticles*; *Colloids Surf. B* 161, 18 (2018)

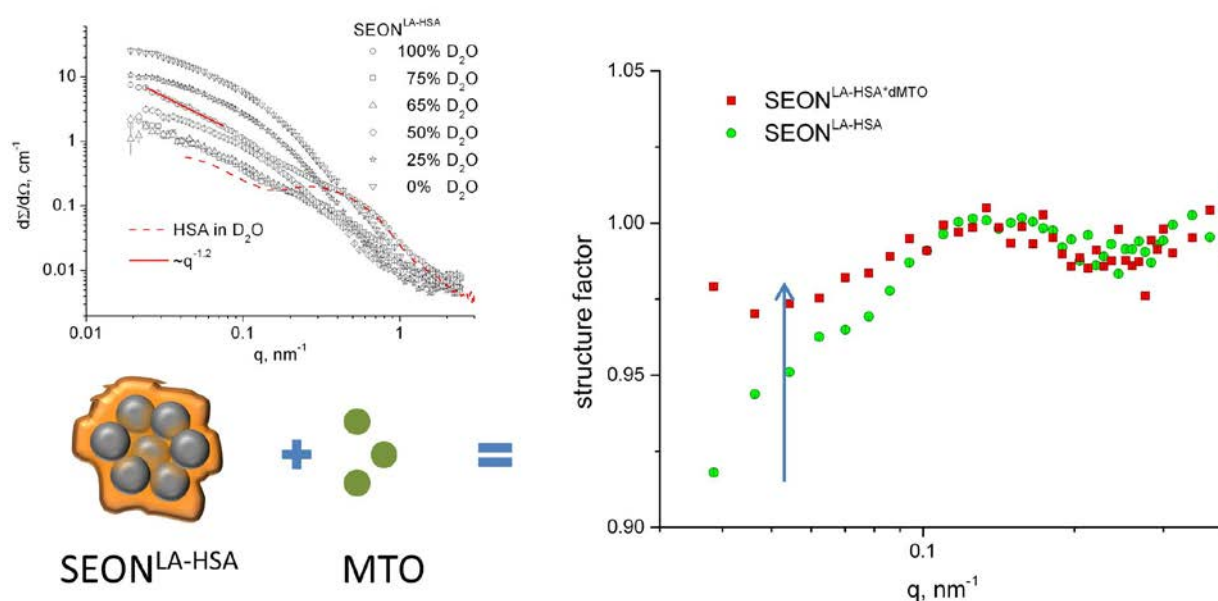


Figure 1: Results of the SANS contrast variation experiments (top left) and the experimentally determined structure factors for samples before and after the addition of dMTO (right). The difference between the structure factors in the low- q region points to the reduction of interaction in the system after drug adsorption.

Elucidating lipid vesicle fusion by time-resolved neutron reflectivity

A. Koutsioumpas¹, M.-S. Appavou¹, D. Lairez²

¹Jülich Centre for Neutron Science (JCNS) at MLZ, Forschungszentrum Jülich GmbH, Garching, Germany; ²Laboratoire des Solides Irradiés, École Polytechnique, CNRS, CEA, Université Paris-Saclay and Laboratoire Léon Brillouin, CNRS, CEA, Université Paris-Saclay, Gif-sur-Yvette, France

Biophysical investigations that rely on the use of supported lipid bilayers (SLB) are proving useful in elucidating model membrane structures and their interaction with biological molecules. The special nature of SLBs i.e., their reconstitution on planar hydrophilic surfaces using vesicle fusion allows the application of a multitude of surface analytical techniques to probe their structure. However, the actual mechanism of membrane formation by fusion is contended in the literature, and many different experimental techniques have been employed in the past in an attempt to address this problem. Since neutron reflectivity can provide a unique subnanometer picture of membrane structure, we have designed and executed a series of time-resolved reflectivity experiments at the MARIA instrument, aiming to capture the intermediate states of membrane formation.

In these experiments, model hydrophilic silicon substrates were brought into contact with low-concentration D₂O solutions of 1-palmitoyl-2-oleoyl-*sn*-glycero-3-phosphocholine (POPC) lipid vesicles that are pre-characterized by cryo-Transmission Electron Microscopy and Dynamic Light Scattering. Under these conditions, membrane formation is relatively slow (in the range of a few hours) so that reflectivity measurements in the 10-20 min time scale may provide representative snapshots of the interfacial scattering length density profile (which informs us about the molecular distribution near the substrate) during the various stages of the phenomenon.

The general features of the time-resolved reflectivity measurements obtained are in agreement with the progressive adsorption of intact vesicles in the initial stage and, subsequently, their transformation to a complete single bilayer separated from the substrate by a thin water layer. However, the experimental observation (Fig. 2) of an early minimum in the

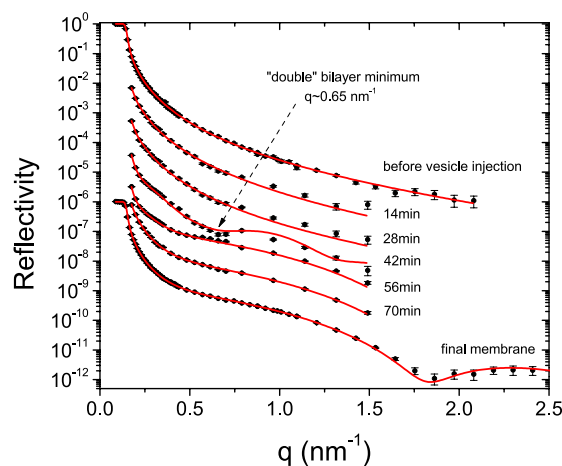


Figure 2: Neutron reflectivity measurements before, during, and after the formation of a POPC bilayer on SiO₂ via vesicle fusion. After the initial measurement, vesicles are injected into the measurement cell at a concentration of 10 µg/mL and reflectivity curves are acquired every 14 min in the q range of up to 1.5 nm⁻¹. For clarity, successive curves are displaced by 1 order of magnitude.

reflectivity profile during the intermediate stage of the process indicates the presence of partial double bilayer stacking. We have theoretically shown that such an effect cannot be attributed to the deformation of unfused vesicles on the substrate. In this respect, it has been shown that the present results favor a mechanism involving the enhanced adhesion of incoming vesicles on the edges of already-formed bilayer patches, in agreement with recent reports based on Interferometric Scattering Microscopy data. Future reflectivity investigations with higher time-resolution (especially on time-of-flight instruments) may extend the present study and elucidate intermediate structural states in more detail, or reveal even faster processes that take place during the formation of lipid membranes on substrates.

[1] A. Koutsioubas et al., *Time-Resolved Neutron Reflectivity during Supported Membrane Formation by Vesicle Fusion*; *Langmuir* 33 (40), 10598 (2017)

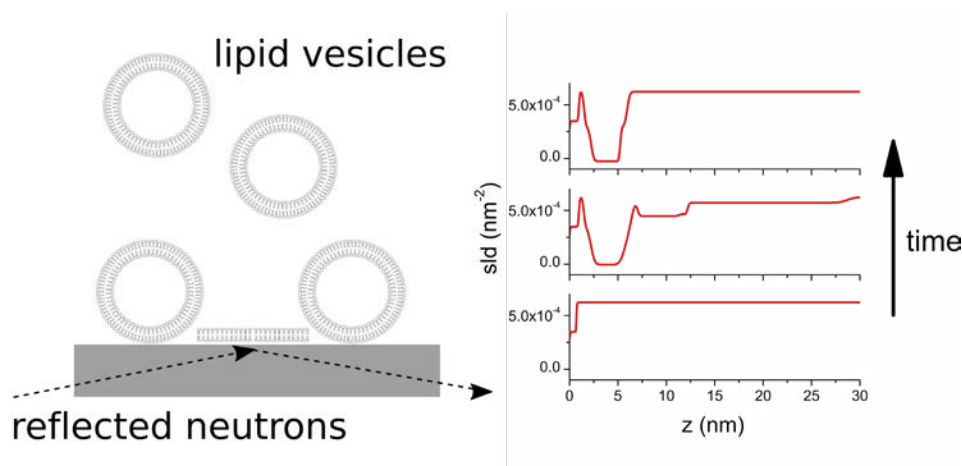


Figure 1: (left) cartoon illustration of the experimental system. (right) scattering length density profiles near the surface as a function of time.

S. R. Midtgaard¹, L. Arleth¹, H. Frielinghaus²¹Structural Biophysics, X-ray and Neutron Science, The Niels Bohr Institute, University of Copenhagen, Copenhagen, Denmark; ²Jülich Centre for Neutron Science (JCNS) at MLZ, Forschungszentrum Jülich GmbH, Garching, Germany

A novel and widely applicable method to determine the structures of membrane proteins in solution via small-angle neutron scattering (SANS) is presented [1]. In order to obtain unimeric (non aggregated) proteins in solution, specifically labeled detergents needed to be developed.

Common detergents for solubilizing membrane proteins were synthesized in isotope-substituted versions to utilize the intrinsic neutron scattering length difference between hydrogen and deuterium. Individual hydrogen/deuterium levels of the detergent head and tail groups were achieved such that the micelles formed became effectively invisible in heavy water (D_2O) when investigated using neutrons. In this way, only the signal from the membrane protein remained in the NS data. We demonstrate that the method is not only generally applicable to five very different membrane proteins, but also reveals subtle structural details about the sarco/endoplasmic reticulum Ca^{2+} ATPase (SERCA). All in all, the synthesis of isotope-substituted detergents makes the solution structure determination of membrane proteins by SANS and subsequent data analysis available to non-specialists.

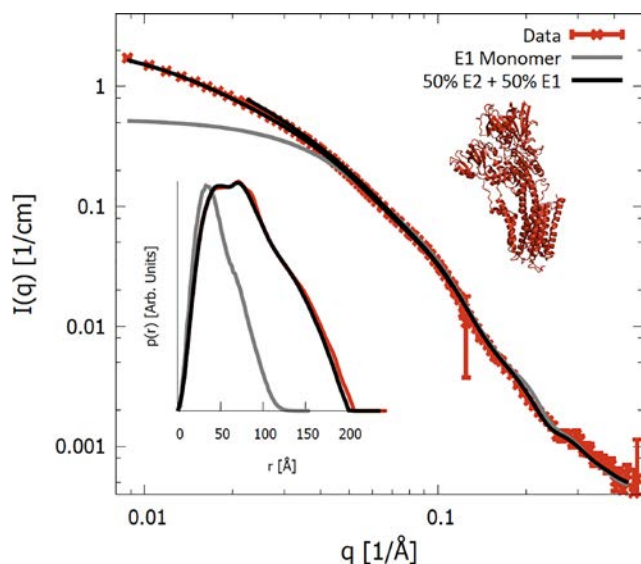


Figure 1: Experimental SANS data (colored points) and the resulting model fit (black full and dashed line) for the membrane protein sarco/endoplasmic reticulum Ca^{2+} ATPase. Note that the instrumental resolution effect is included in the model, which then exhibits small discontinuities at medium q -values. Insert: The corresponding pair-distance distribution function as determined by Indirect Fourier transform with identical color scheme. The figure shows the known structure from crystallography.

The crystal structure was available for the SERCA protein, and was used as a basis for modeling the theoretical scattering patterns to be compared to the experimental data. SERCA was found with a combination of two structural states combined with a minor aggregated fraction of SERCA using an approach developed earlier [1]. A hydration layer was added to the water-exposed surface. Resolution effects were taken into account. A constant background and a scale factor were fitted to obtain the best agreement between the data and model, as shown in Fig. 1. The figure also plots the theoretical pair distance distribution functions $p(r)$ calculated from the fitted model, together with those obtained from the data by indirect Fourier transformation.

A bottleneck: Obtaining crystals of membrane proteins

The method of using match-out deuterated detergents to obtain the solution structures of membrane proteins fills an important gap in the toolbox for their detailed investigation. While traditional protein crystallography has undeniably produced fantastic new insights into biological processes over several decades, obtaining crystals of membrane proteins diffracting to high resolution remains a bottleneck. Indeed, larger flexible membrane proteins are under-represented in the protein data bank due to this obstacle. The method presented here makes it possible to probe the structure in detail early in the process when a robust expression and purification protocol has been established.

Five different membrane proteins and two detergents were investigated in this study [1]. The data demonstrate the general applicability of the approach and provide promising perspectives for future use. The basic idea of match-out deuteration may easily be generalized to other detergent types to accommodate special needs for particular membrane proteins or in combination with the selective deuteration of different subunits.

[1] S.R. Midtgaard et al., *Invisible detergents for structure determination of membrane proteins by small-angle neutron scattering*; *FEBS J.* 285, 357 (2017)

R. Wang^{1,2}, Z.-Y. Di¹, P. Müller-Buschbaum², H. Frielinghaus¹

¹Jülich Centre for Neutron Science (JCNS) at MLZ, Forschungszentrum Jülich GmbH, Garching, Germany; ²Institute for Functional Materials, Department of Physics, Technical University of Munich, Garching, Germany

Diblock copolymers are a very interesting polymer type in which two immiscible polymers are covalently bonded. Instead of the macrophase separation that is present in the blend of the two components, diblock copolymers undergo a microphase separation. Thereby, they self-assemble into an array of fine morphologies with domain size close to 10 nm, matching the exciton diffusion length of polymer-based organic solar cells. In addition, using a conjugated polymer as one of the two blocks adds unique optical and electronic properties. Therefore, the combination of these intriguing characteristics makes conjugated diblock copolymers appealing for fundamental studies in organic photovoltaic research.

In the present investigation, the diblock copolymer poly(3-hexylthiophene-2,5-diyl)-block-polystyrene (P3HT-b-PS) is blended with phenyl-C61-butyric acid methyl ester (PCBM) at different weight ratios to prepare thin films. Due to the unique contrast advantage afforded by P3HT-b-PS:

PCBM films, the formed morphologies are quantitatively determined by grazing incidence small angle neutron scattering (GISANS) at the KWS-1 instrument. As shown in Fig. 1, the degree of lamellar order of P3HT-b-PS is diminished upon the addition of PCBM, whereas well-ordered hexagonal packed cylindrical structures appear in the sample with a PCBM weight fraction of 67%. As demonstrated by the variation of the scattering contrast, PCBM first interacts with the PS block at low PCBM content and forms aggregates in samples with PCBM weight fractions above 50%. The revealed morphology evolution directly impacts on the photoluminescence property and provides a new insight into the design of potential solar cell devices based on conductive block copolymers.

[1] R. Wang et al., *Effect of PCBM additive on morphology and optoelectronic properties of P3HT-b-PS films*; *Polymer* 121, 173 (2017)

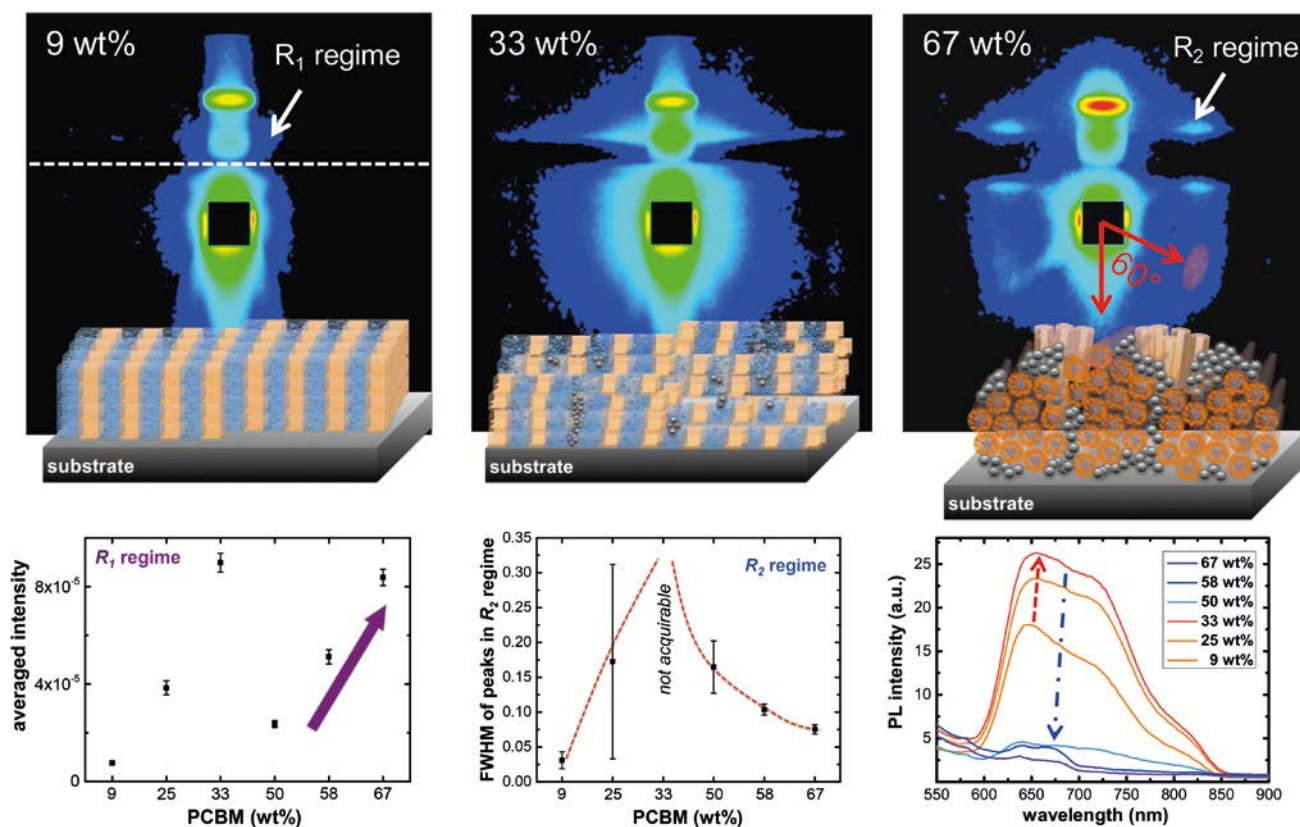


Figure 1: Top row: 2D GISANS data of P3HT-b-PS:PCBM blend films with three different weight fractions alongside the corresponding schematic representation of the related morphologies. Bottom row: Average intensities in R_1 regime (left), full width at half maxima (FWHM) of the scattering peaks in R_2 regime (middle), and photoluminescence spectra (right) of the different composite films.

T. Nylander^{1,2}, O. Soltwedel^{3,4}, M. Ganeva⁵, C. Hirst¹, J. Holdaway¹, M. Yanez Arteta¹, M. Wadsäter^{2,6}, J. Barauskas^{6,7}, H. Frielinghaus⁵, O. Holderer⁵

¹Department of Chemistry, Physical Chemistry, Lund University, Lund, Sweden; ²NanoLund, Lund University, Lund, Sweden; ³Max-Planck-Institute for Solid State Research, Stuttgart, Germany; ⁴Heinz Maier-Leibnitz Zentrum (MLZ), Garching, Germany; ⁵Jülich Centre for Neutron Science (JCNS) at MLZ, Forschungszentrum Jülich GmbH, Garching, Germany; ⁶Camurus AB, Lund, Sweden; ⁷Faculty of Health and Society, Biomedical Science, Malmö University, Malmö, Sweden

The main building blocks of the membranes that surround cells are lipid mixtures that form lamellar phases. However, lipids have a rich phase behaviour ranging from micellar, hexagonal or cubic to lamellar and, further, to the reversed counterparts, which are also utilized in many biological systems. These phases make it possible to tune key properties, such as rigidity, curvature and interfacial behaviour – all essential points for living systems as well as in applications such as drug delivery systems. By selectively manipulating the packing parameter of the building blocks, the ratio of the minimum area of the hydrophilic heads and hydrophobic tails of the lipids or lipid mixtures required, the particular phases can be tuned.

We have used a combination of grazing incidence neutron spin echo spectroscopy, specular and off-specular neutron reflectivity (NR) and grazing incidence small angle neutron scattering, as well as small angle x-ray scattering to determine the dynamics and structural characteristics of non-lamellar lipid assembly films supported on a silicon block. The ratios of phosphatidylcholine (PC) and glycerol dioleate (GDO) investigated showed a cubic (35/65 SPC/GDO) and reverse hexagonal (60/40 SPC/GDO) lipid crystalline structure, irrespective of the type of preparation. On closer inspection, both structures exhibit similar lattice parameters on supporting surface as in bulk. However, on a supporting surface, they are ~10% larger than those determined in bulk, due to enhanced hydration. The lateral domain-size at the interface of the inverse-hexagonal phase

is estimated to some microns. In contrast, the cubic phase domains show no strong orientation, but rather exhibit a typical powder pattern.

Exact lattice parameters of the inverse hexagonal phase at a hydrophilic interface were further examined using the Born-Again software package. It turns out that the formed cylinders are more than a micrometer in length and are oriented parallel to the interface, while the lattice is slightly distorted towards a face centered. Since the orientation of the inverse hexagonal lipid bilayers at an interface changes from a 2D into a 3D structure, possible depth dependent dynamics are investigated. Here, the spectrum of undulations is roughly 4 times higher adjacent to a rigid interface. Moreover, in comparison to that of the rigid cubic phase, which possesses a more perfect lattice, the pronounced flexibility of the hexagonal lattices is reflected by their distortion toward a face-centered lattice. With its strong hydration at the interface it seems to act as a lubrication layer. The hexagonal phase exhibits fluctuations in the length and time scales of nanometers and nanoseconds, while the cubic phase suppresses undulations. This study opens up the possibility for new nanostructured materials based on tailor-made lipid layers.

[1] T. Nylander et al., *Relationship between Structure and Fluctuations of Lipid Nonlamellar Phases Deposited at the Solid-Liquid Interface*; *J. Phys. Chem. B* 121 (13), 2705 (2017)

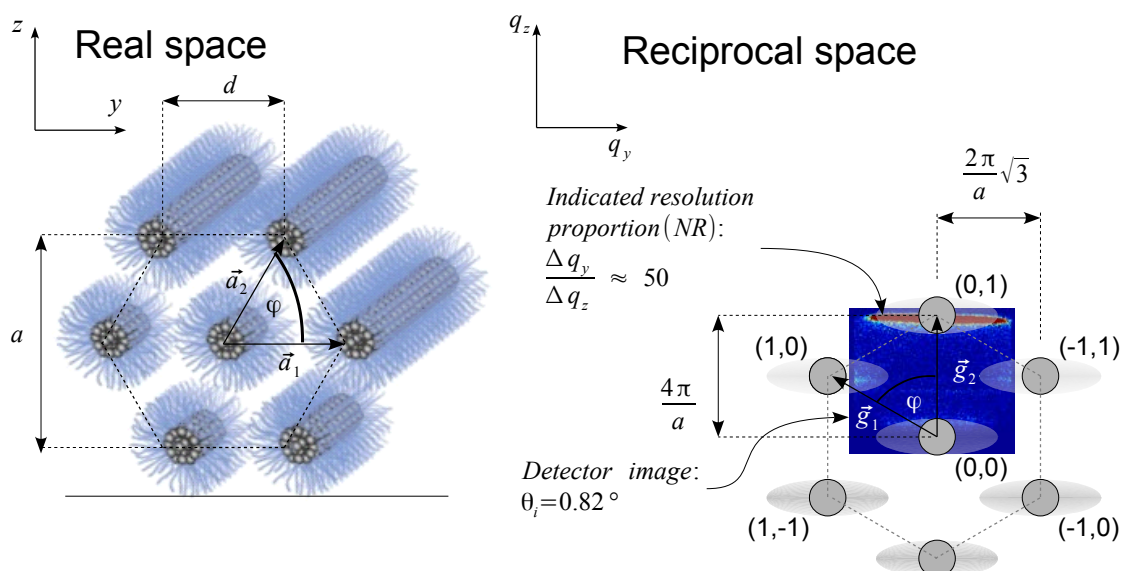


Figure 1: Evaluated real space structure (SPC/GDO (60/40 wt %)) from the NR-detector image at 0.82° incident angle.

M. Kruteva¹, S. Pasini¹, M. Monkenbusch¹, J. Allgaier¹, J. Maiz², C. Mijangos², B. Hartmann-Azanza³, M. Steinhart³, N. Jalarvo^{1,4}, O. Ivanova⁵, O. Holderer⁵, A. Radulescu⁵, M. Ohl⁶, P. Falus⁷, T. Unruh⁸, D. Richter¹

¹Jülich Centre for Neutron Science (JCNS) and Institute for Complex Systems (ICS), Forschungszentrum Jülich GmbH, Jülich, Germany; ²Instituto de Ciencia y Tecnología de Polímeros, CSIC, Madrid, Spain; ³Institute of Chemistry of new Materials, Universität Osnabrück, Osnabrück, Germany; ⁴Chemical and Engineering Materials Division, Oak Ridge National Laboratory (ORNL), Oak Ridge, USA; ⁵Jülich Centre for Neutron Science (JCNS) at MLZ, Forschungszentrum Jülich GmbH, Garching, Germany; ⁶Jülich Centre for Neutron Science (JCNS), Forschungszentrum Jülich GmbH, Outstation Oak Ridge, USA; ⁷Institute Laue-Langevin (ILL), Grenoble, France; ⁸Institute for Crystallography and Structural Physics, Physics Department, Friedrich-Alexander-University Erlangen-Nürnberg, Erlangen, Germany

Polymer composite materials are gaining ever more in importance due to the tunability of their properties. Their structure and dynamics are perturbed in confinement, especially when the confinement length is comparable to the size of a polymer chain. For polymers confined in porous media, the presence of a large amount of solid surface reduces the number of possible conformations of a polymer chain and influences the dynamics. We investigated the structure and dynamics of polyethylene-*alt*-propylene (PEP) melts confined in cylindrical nanopores of self-ordered anodic alumina, for which the hydrophilic alumina surface may be considered as locally repulsive with respect to the strongly hydrophobic PEP.

SANS measurements

We used a mixture of h/d PEP polymers with a molecular weight of $M_w = 50$ kg/mol for sample and bulk. The nanopores have a diameter of 20 nm, a nearest-neighbour distance of 55 nm and a pore depth of 100 μm .

The Debye model describes the small-angle data quite well and makes it possible to extract the radius of gyration (R_g). We found $R_g = 85$ Å, which is comparable to the radius of gyration for PEP bulk 96 Å. Thus the structure of the polymer is not dramatically altered by the confinement. Nevertheless, we found that the exponent of the chain statistics ($1/Q^n$) deviates from the Gaussian value of 2 and is rather $n = 2.3$. Thus the shape of polymer scattering indicates some degree of compression.

NSE and the dynamics

The Rouse rate was extracted from the NSE data of the bulk sample at 420 K in the early time regime: $W^t = (1.10 \pm 0.02)$ nm⁴/ns. This value compares well with the $W^t = 0.95$ nm⁴/ns for PEP at 423 K known from litera-

ture.

Fig. 1 shows how the data for confined and bulk lie on top of each other, not only in the Rouse regime, but also the local reptation regime. Thus, no evident effects due to confinement are seen on the polymer dynamics. In this regime we fitted the tube diameter d : We found for the bulk $d = (47.3 \pm 0.4)$ Å and $d = (48.7 \pm 0.5)$ Å for PEP, after imposing the same Rouse rate as for the bulk; with contour length fluctuation contributions the fit yields $d_{\text{bulk}} = (52.5 \pm 0.5)$ Å and $d_{\text{PEP}} = (52.8 \pm 0.6)$ Å. Thus, our experiment shed some light on the as yet unclear results from numerical simulations and showed that, within the limits of experimental error, intermediate confinement between locally repulsive walls does not affect the entanglement network.

[1] M. Kruteva et al., *Polymer dynamics under cylindrical confinement featuring a locally repulsive surface: A quasielastic neutron scattering study*; *J. Chem. Phys.* **146**, 203306 (2017)

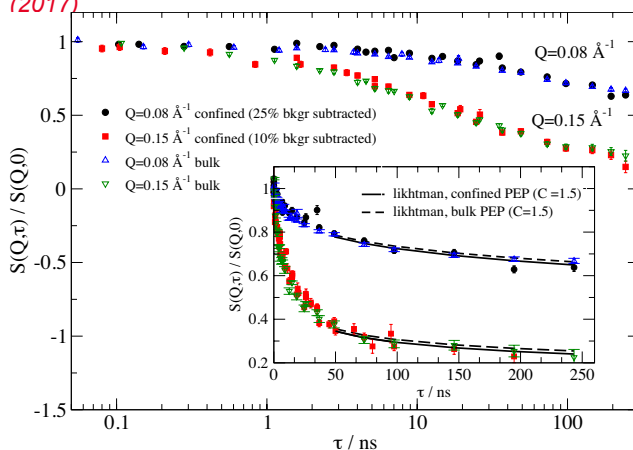


Figure 1: PEP bulk and PEP confined data (with background subtracted). Inset: same data fitted in the reptation regime. Backscattering results on the local dynamics showed that the Rouse rate hardly changes under confinement; after subtracting an estimated background of 25 % for $Q = 0.08$ Å⁻¹ and 10 % for $Q = 0.15$ Å⁻¹ bulk and sample show the same dynamics at short Fourier times.

R. Ünneper¹, M.-S. Appavou², G. Garab³, N. Keren⁴

¹Wigner Research Centre for Physics, Institute for Solid State Physics and Optics, Hungarian Academy of Sciences, Budapest, Hungary; ²Jülich Centre for Neutron Science (JCNS) at MLZ, Forschungszentrum Jülich GmbH, Garching, Germany; ³Institute of Plant Biology, Biological Research Center, Hungarian Academy of Sciences, Szeged, Hungary; ⁴Department of Plant & Environmental Sciences, The Alexander Silberman Institute of Life Sciences, Hebrew University, Jerusalem, Israel

Cyanobacteria (or blue-green algae), the ancestors of chloroplasts of vascular plants, the first photosynthetic organisms that are capable of producing oxygen, appeared about 3 billion years ago and contributed significantly to the transformation of our globe into a habitable planet. These organisms can be found in the most diverse terrestrial and aquatic habitats – from hot springs to the Antarctic region, and from the oceans and fresh water lakes to rocks and desert soils that are exposed to only temporary moisture. In order to acclimate to these different habitats and to adapt to rapidly changing environmental conditions (temperature, illumination intensity, availability of nutrients and water), different cyanobacteria evolved different, multilevel regulatory mechanisms, the details of which are not well understood.

We studied a desiccation tolerant desert cyanobacterium, *Leptolyngbya ohadii*, a species in desert sand crusts. *L. ohadii* spends most of the daytime in the desiccated state in strong sunshine, surviving extremely harsh conditions. Recovery of photosynthesis can occur immediately upon the addition of water (in nature, e.g. predawn dew deposition). Desiccation and rehydration in photosynthetic organisms are complex processes; it is important to reveal their structural background.

As revealed by small-angle neutron scattering, in the hydrated state, the multilamellar thylakoid membrane system (responsible for the conversion of light energy to chemical energy in the cell) displayed three peaks in the SANS profile (measured at KWS 2), at $q = 0.072 \text{ nm}^{-1}$ and two additional, higher harmonic features at 0.139 and 0.221 nm^{-1} (Fig. 1a). These values can be interpreted as the $RD \approx 87 \text{ nm}$ of thylakoid membranes (the repeat distance of thylakoids, with the two bilayer membranes, the lumen, and the interthylakoidal space containing the large hemispherical outer-membrane light-harvesting antenna complexes, the phycobilisomes). In the desiccated state these peaks were completely lost. The scattering intensity decreased dramatically due to the loss of water and no Bragg peak could be discerned between 0.05 and 0.1 nm^{-1} ; instead, a broad shoulder emerged between 0.10 and 0.15 nm^{-1} , which can be assigned to a $20\text{-}30 \text{ nm}$ shrinkage in the RD . Based on these SANS results and other experiments (SAXS, electron microscopy, functional and ultrafast spectroscopy measurements), a novel energy-dissipation mechanism was proposed that is reliant on changes in the aggregation state of the phycobilisomes (Fig. 1b).

[1] L. Bar-Eyal et al., *Changes in aggregation states of light-harvesting complexes as a mechanism for modulating energy transfer in desert crust cyanobacteria*; *Proc. Natl. Acad. Sci. U.S.A.* 114, 9481 (2017)

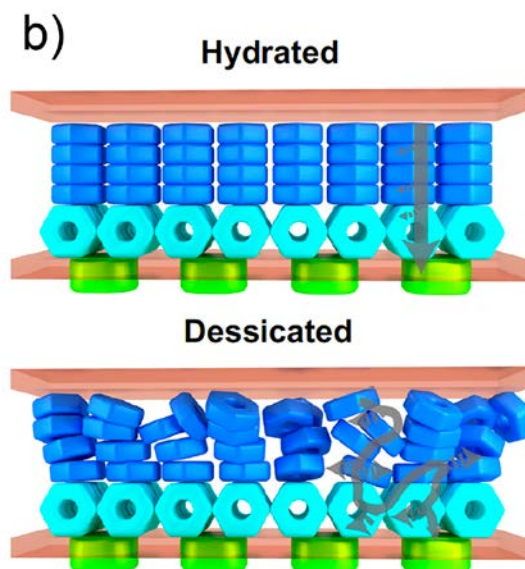
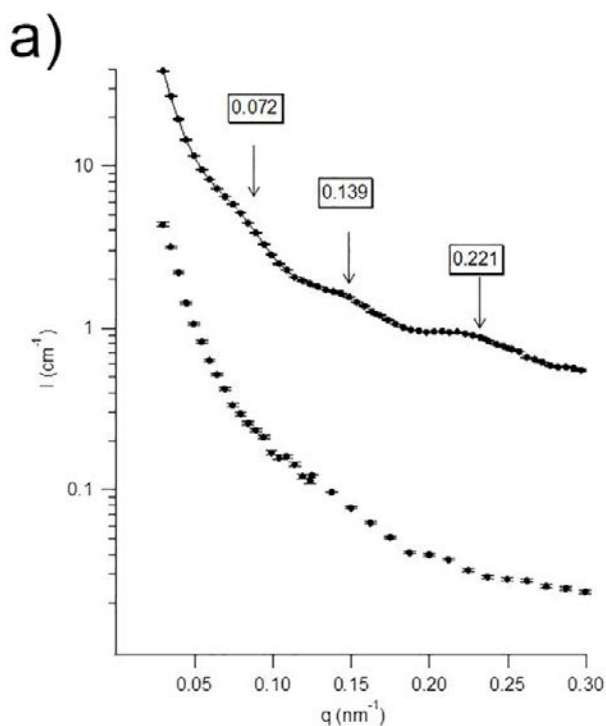


Figure 1: Radially averaged SANS curves and schematic figure of cyanobacterial thylakoid membranes showing phycobilisomes in hydrated and desiccated states [1].

G. Vitiello¹, L. Paduano², A. Koutsoubas³¹Department of Chemical, Materials and Production Engineering, University of Naples "Federico II", Naples, Italy; ²Department of Chemical Sciences, University of Naples "Federico II", Naples, Italy; ³Jülich Centre for Neutron Science (JCNS) at MLZ, Forschungszentrum Jülich GmbH, Garching, Germany

Amphiphilic ionophores

Interaction with cell membranes is of crucial importance for biologically active small organic molecules, which can be conveyed into the cell by exploiting a variety of active or passive transport mechanisms. An example of these processes is provided by ionophores, i.e. synthetic amphiphiles able to transport cations or anions into the cells either by forming specific channels, or acting as carriers within the membrane bilayers. By altering the ion concentration within the cytoplasm, they can actively interfere with physiological processes or even reverse pathological effects.

Recently, an amphiphilic guanosine-based ionophore was synthesized (Fig. 1a), showing an interesting biological activity. To elucidate the structure-activity relationships of this molecule, in the search for indications of a rational design of second-generation guanosine-based ionophores, we have studied its interaction with lipid bilayers.

Neutron Reflectometry: ionophore-membrane interaction

Neutron reflectometry measurements were performed on supported bilayers of dioleoylphosphocholine (DOPC)/dioleoylphosphoglycerol (DOPG) 95/5 w/w in the absence and presence of the amphiphilic guanosine-derivative (Fig. 1a) by using D₂O, H₂O and their mixtures (SMW, 4MW) as isotopic contrast solvents (Fig. 1b and c). The best fit to these curves makes it possible to describe the changes in the membrane structure due to the interaction with the ionophore. A large increase in the bilayer thickness (~9 Å) was observed following the addition of the ionophore, suggesting it had been inserted into the bilayer. In particular, the thickness increases by ~2 and ~3 Å for the inner and outer

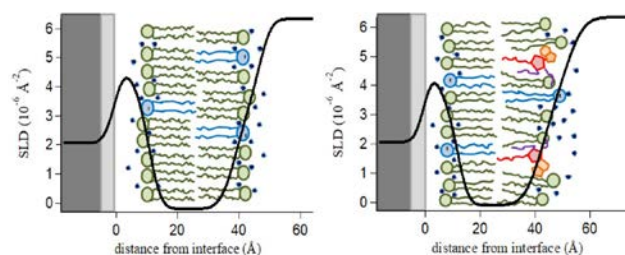


Figure 2: Scattering Length Density (SLD) profiles in D₂O for DOPC/DOPG bilayers in the absence (on the right) and presence (on the left) of guanosine-based ionophore.

headgroup layers, respectively, while the hydrophobic region thickness increases by ~3 Å. Remarkably, a decrease in the solvent content of the external headgroup layer was also obtained.

This model suggested that the guanosine-based amphiphile interacts stably with the lipid bilayer (Fig. 2), partially modifying the lipid organization and increasing both its thicknesses. Also, the dehydration of lipid headgroups operated by the amphiphilic guanosines and the insertion of the oligo(ethylene glycol) chains in the bilayer hydrophobic core could play a fundamental role in driving the process, thus furnishing directions to rationally implement future ionophores design.

This study has furnished an in-depth picture of the effect of this ionophore on membrane structure, relevant for their ion transport mechanism through lipid bilayers.

[1] G. Vitiello et al., Ionophores at work: Exploring the interaction of guanosine-based amphiphiles with phospholipid membranes; *BBA-Biomembranes* 1859, 2392 (2017)

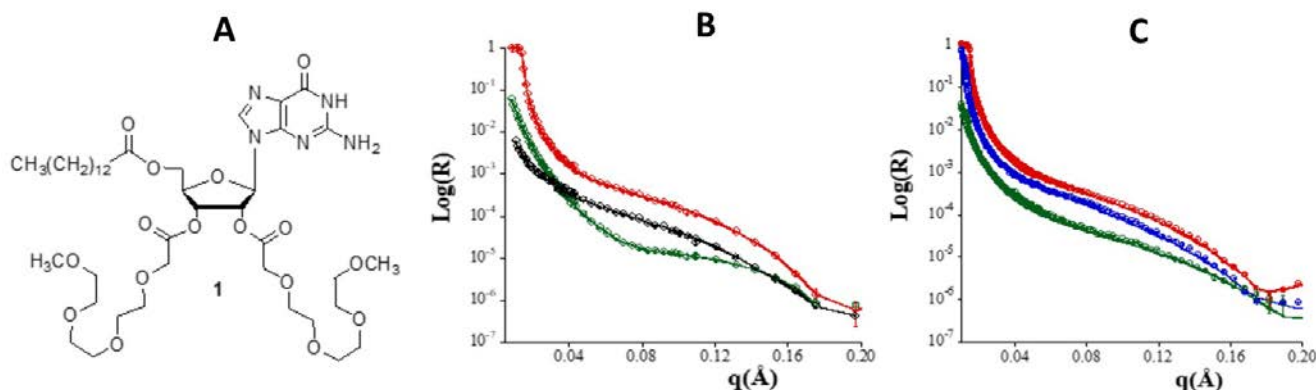


Figure 1: Chemical structure of amphiphilic guanosine derivative (panel a) Neutron reflectivity curves for lipid bilayers of DOPC/DOPG in the absence (panel b) and presence (panel c) of the amphiphilic guanosine derivative in D₂O (red), SMW (black), 4MW (blue) and H₂O (green) contrast solvents.

Y. Zhao¹, K. Yoshimura¹, A. Hiroki¹, Y. Kishiyama², H. Shishitani², S. Yamaguchi², H. Tanaka², S. Koizumi³, J. Houston⁴, A. Radulescu⁴, M.-S. Appavou⁴, D. Richter⁵, Y. Maekawa¹

¹Takasaki Advanced Radiation Research Institute, Department of Advanced Functional Materials Research, National Institutes for Quantum and Radiological Science and Technology (QST), Takasaki, Japan; ²Daihatsu Motor Co., Ltd., Ryuo Gamo, Japan; ³Department of Engineering, Ibaraki University, Japan; ⁴Jülich Centre for Neutron Science (JCNS) at MLZ, Forschungszentrum Jülich GmbH, Garching, Germany; ⁵Jülich Centre for Neutron Science & Institute for Complex Systems, Forschungszentrum Jülich GmbH, Jülich, Germany

Anion-exchange membranes (AEMs) have been regarded as an alternative to proton-exchange membranes (PEMs) in energy conversion devices, due to the advantage they offer of saving expensive platinum catalysts. However, neither the molecular design nor our understanding of their properties is sufficient to develop AEMs capable of practical fuel cell applications. It is crucial to thoroughly study the current AEMs in terms of microphase structures and conducting properties. Recently, we developed a new graft type of AEMs by the radiation-induced grafting method, where imidazolium and styrene monomers were grafted into poly(ethylene-co-tetrafluoroethylene) (ETFE) base films under a dose of 80 kGy from the ⁶⁰Co γ -ray source (QST, Takasaki), followed by alkylation and ion exchange reactions. These AEMs exhibit well-balanced properties of high ion conductivity (> 100 mS/cm at 80 °C) and good stability, which are believed to be controlled by the microphase structure of the membrane. In this report, we investigate a specific AEM (denoted as AEM91, imidazolium/styrene ratio ~ 65/35, grafting degree ~ 91 %, and ion exchange capacity ~ 1.82 meq/g), and reveal its structure and the relationship between this and its properties, using the small-angle neutron scattering (SANS) method, performed on KWS-2 SANS diffractometer at the MLZ.

Fig. 1 shows SANS intensity profiles, $I(q)$, of pristine ETFE films (profile 1), grafted-ETFE membranes (profile 2), dry AEM91 (profile 3) and AEM91 equilibrated in D₂O (profile 4)

as a function of the scattering vector q . The different morphologies which can be deduced from the SANS profiles are also shown in the Fig. 1.

The experiments confirm the semi-crystalline feature of AEM91 conserved from the original ETFE base film, which is the key factor in high membrane mechanical stability, and show the dependence of the structure on hydration.

Contrast variation experiments performed on AEM91 equilibrated in water mixtures of H₂O and D₂O, further show that graft polymers and water constitute the hydrophilic ion channels [1]. Since graft polymers distribute randomly in AEM91, well-connected hydrophilic ion channels are feasibly formed, which are the key factor in high membrane conductivity.

Above all, the morphology of AEM91 can be characterized by three phases: phase 1) the crystalline ETFE phase offers good mechanical properties; phase 2) the hydrophobic amorphous phase offers a matrix to embed conducting channels; and phase 3) well-connected hydrophilic ion channels promote the anion conductivity.

[1] Y. Zhao et al., *Imidazolium-based anion exchange membranes for alkaline anion fuel cells: elucidation of the morphology and the interplay between the morphology and properties*; *Soft Matter* 12, 1567 (2016)

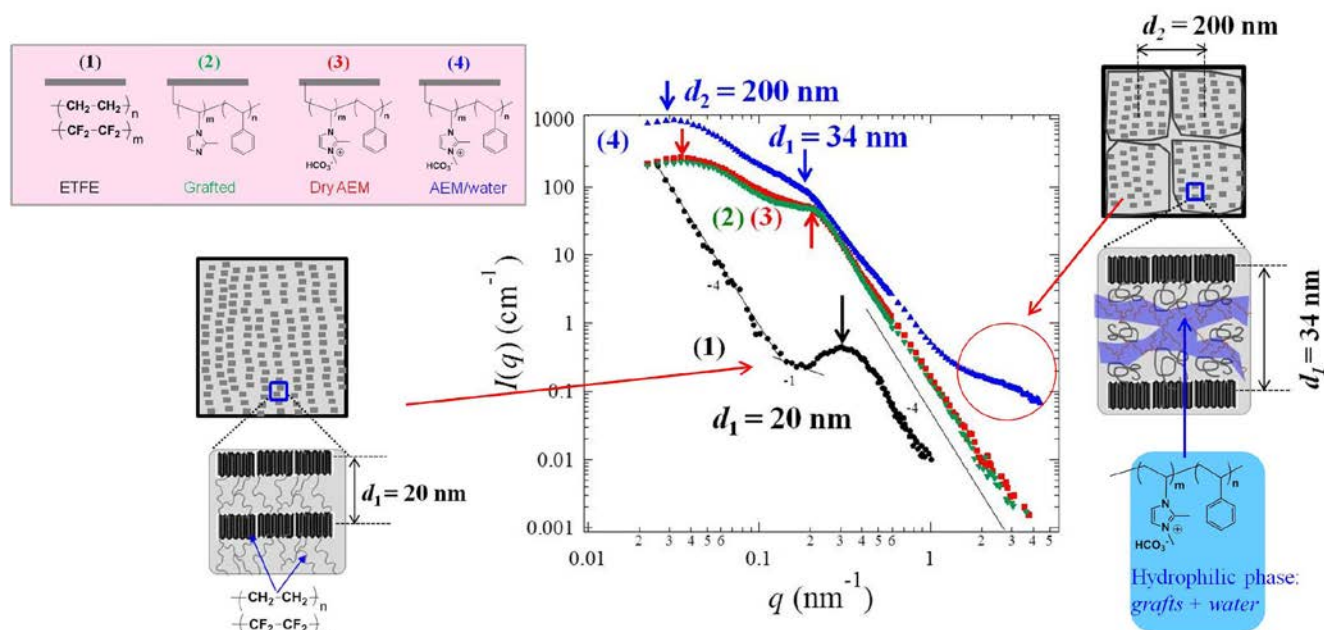


Figure 1: SANS profiles of (1) pristine ETFE film, (2) grafted-ETFE, (3) dry AEM91, and (4) AEM91 equilibrated in D₂O.

K.-N. Truong¹, C. Merckens¹, M. Meven², B. Faßbänder¹, R. Dronskowski^{1,3}, U. Englert¹¹Institute of Inorganic Chemistry, RWTH Aachen University, Aachen, Germany; ²Institute of Crystallography, RWTH Aachen, and Jülich Centre for Neutron Science (JCNS) at MLZ, Garching, Germany; ³Jülich-Aachen Research Alliance (JARA-HPC), RWTH Aachen University, Aachen, Germany

The organic, substituted acetylacetonate molecule 3-(pyridin-4-yl)pentane-2,4-dione, HacacPy, **1** (Fig. 1) represents a versatile reagent in coordination chemistry and exhibits a reversible second-order phase transition at approximately 50 K. In its high temperature form 1α , the molecule is disordered around the twofold axis in the space group $C2/c$, the proton H10 being located on two equivalent positions with 50 % : 50 % probability. During the t_2 type (translationengleich) phase transition, the 1α structure transforms into the twinned low temperature modification $P\bar{1}(1\beta)$, resulting in a reflection splitting along with proton ordering in the intramolecular hydrogen bond (Fig. 1).

Neutron diffraction at HEiDi

Large ($> 60 \text{ mm}^3$) high-quality single crystals of **1** were obtained by sublimation. An understanding of the underlying nature of the observed phase transition requires accurate localisation of the protons in this system. Neutron diffraction with its superior sensitivity for hydrogen, easy handling at low temperatures down to about 2 K and the high resolution available at the HEiDi instrument are ideally suited for

such diffraction experiments. These measurements were performed on one sample ($4.4 \times 4.3 \times 3.3 \text{ mm}^3$) at temperatures well above and well below the phase transition (100 and 2.5 K, respectively), combining data obtained with two different wavelengths ($\lambda = 0.793 \text{ \AA}$ and 1.170 \AA , $\Delta\lambda/\lambda \approx 5 \cdot 10^{-3}$) to maximize the accessible Q-range in reciprocal space ($(\sin\theta/\lambda)_{\text{max}} = 0.74 \text{ \AA}^{-1}$).

The structural phase transition studied on our single crystal has been found to be very sluggish, showing a very pronounced hysteresis, which at first glance contradicts the Landau theory for group – subgroup phase relations. We therefore performed a temperature-resolved X-ray powder diffraction study which confirms that this hysteresis depends primarily on the particle size as it is not present in the case of finely-ground powder. This enabled us to determine a transition temperature of about 50 K.

[1] K.-N. Truong et al., *Phase transition and proton ordering at 50 K in 3-(pyridin-4-yl)pentane-2,4-dione*; *Acta Crystallogr. B* **73**, 1172 (2017)

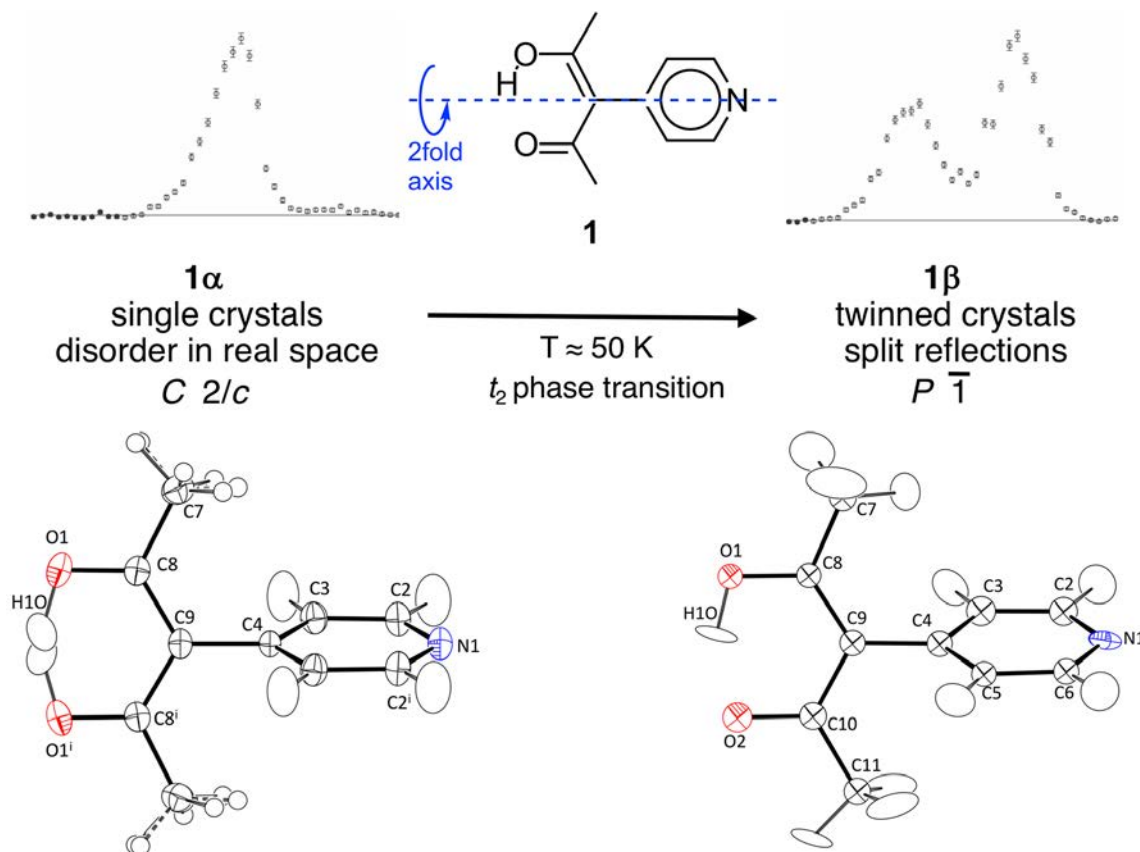


Figure 1: Lewis diagram of **1** (top, center) and symmetry relationship between the high-temperature form 1α (left) and the low-temperature form 1β (right); the situation in reciprocal space is depicted in the upper part of this figure, in real space in the lower part. The single reflection $(0\ \bar{6}\ 2)$ in 1α splits into $(2\ 3\ \bar{3})$ and $(2\ \bar{3}\ 3)$ in 1β . Ellipsoids are drawn with 50 % probability level; H atoms of the disordered methyl group (bottom, left) are shown as spheres of arbitrary radii. Symmetry operator: (i): $-x + 2, y, -z + 3/2$.

L. Liu^{1,2}, M. Knapp¹, H. Ehrenberg¹, L. Fang¹, H. Fan³, L. A. Schmitt⁴, H. Fuess⁴, M. Hoelzel⁵, H. Dammak⁶, M. P. Thi⁷, M. Hinterstein^{1,8}

¹Institute for Applied Materials (IAM), Karlsruhe Institute of Technology (KIT), Karlsruhe, Germany; ²College of Materials Science and Engineering, Guilin University of Technology, Guilin, China; ³School of Materials Science and Engineering, Northwestern Polytechnical University, Xi'an, China; ⁴Institute of Materials Science, Technische Universität Darmstadt, Darmstadt, Germany; ⁵Heinz Maier-Leibnitz Zentrum (MLZ), Technical University of Munich, Garching, Germany; ⁶Laboratoire Structures, Propriétés et Modélisation des Solides, Ecole Centrale Paris, Châtenay-Malabry, France; ⁷Thales Research and Technology, Ceramics and Packaging Department, Orsay, France; ⁸School of Materials Science and Engineering, UNSW Australia, Sydney, Australia

Ferroelectric materials of the system $K_{0.5}Na_{0.5}NbO_3 - Bi_{0.5}Na_{0.5}TiO_3$ (KNN-BNT) are considered as lead-free replacements for $PbZr_xTi_{1-x}TiO_3$ due to their good piezoelectric properties. In a comprehensive study, we have revealed the complex phase diagram of the KNN-BNT solid solution [1]. Temperature dependent neutron powder diffraction was combined with electron and X-ray diffraction, as well as Raman spectroscopy and dielectric measurements, to probe different length scales and poling mechanisms.

Neutron powder diffraction at SPODI

Temperature dependent neutron powder diffraction at SPODI allowed a detailed characterization of the oxygen octahedral tilting systems across the phase diagram. Due to the high coherent scattering length of oxygen, characteristic superlattice reflections could be observed that were not visible in the synchrotron X-ray data (Fig. 1).

While the end members exhibit classic ferroelectric (KNN) and relaxor-like behaviour (BNT), the solid solution involves a complex series of transitions with re-entrant and dipolar glass-like behaviour together with diffuse phase transitions. The simultaneous substitution of A- (Bi^{3+}) and B-sites (Ti^{4+}) in KNN is accompanied by the disappearance of long-range order ferroelectric domains and the formation of nanoclusters. Fig. 2 illustrates the structural phase diagram together with the corresponding physical properties.

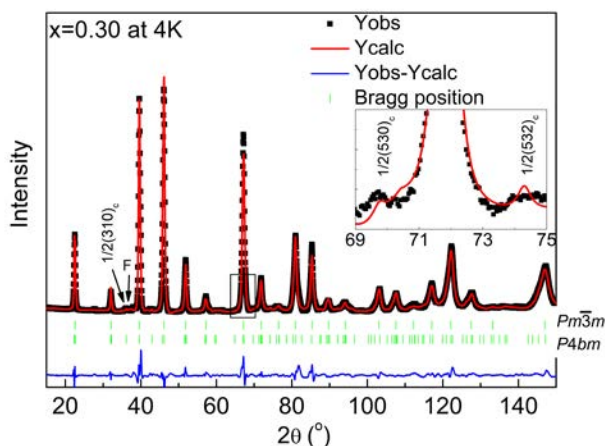


Figure 1: Rietveld refined neutron diffraction data of $x = 0.30$ in x BNT-(1- x)KNN at 4 K. Inset shows the characteristic superlattice reflections $1/200c$ appearing in the P4bm phase.

The local structure maintains distortions away from the cubic average structure in the range $0.10 \leq x \leq 0.90$. On the BNT-rich side, additional oxygen octahedral tilting can be observed, which changes from rhombohedral type $a'a'a'$ to tetragonal type $a^0a^0c^+$ and no tilting $a^0a^0a^0$. The average lattice symmetry changes as follows: orthorhombic ($x \sim 0.005$) \rightarrow tetragonal ($x \sim 0.10$) \rightarrow pseudocubic ($0.10 < x < 0.90$) \rightarrow rhombohedral ($x \geq 0.90$). With increasing BNT content the change in dielectric behaviour follows the sequence: normal ferroelectric \rightarrow diffuse phase transition \rightarrow re-entrant-like relaxor \rightarrow relaxor + dipolar-glass-like relaxor \rightarrow BNT-like relaxor.

The application of different experimental techniques was viable - the complex phase diagram could only be revealed by a comprehensive combination of dielectric, spectroscopic and diffraction methods.

[1] L. Liu et al., Average vs. local structure and composition-property phase diagram of $K_{0.5}Na_{0.5}NbO_3 - Bi_{1/2}Na_{1/2}TiO_3$ system; *J. Eur. Ceram. Soc.* 37, 1387 (2017)

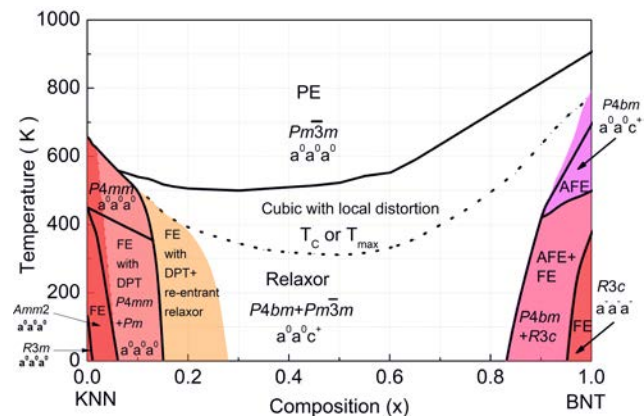


Figure 2: Phase diagram of the KNN-BNT system plotted based on the results of dielectric, Raman and diffraction measurements. FE-ferroelectric, AFE-antiferroelectric, PE-paraelectric, DPT-diffuse phase transition.

Y. Kousaka^{1,2}, T. Koyama³, K. Ohishi⁴, K. Kakurai⁴, V. Hutanu⁵, A. Sera³, K. Inoue^{2,3}, J. Akimitsu^{1,2}

¹Research Institute for Interdisciplinary Science, Okayama University, Okayama, Japan; ²Chirality Research Center, Hiroshima University, Higashi-hiroshima, Japan; ³Graduate School of Science, Hiroshima University, Higashi-hiroshima, Japan; ⁴Neutron Science and Technology Center, Comprehensive Research Organization for Science and Society (CROSS), Tokai, Japan; ⁵Institute of Crystallography, RWTH Aachen, and Jülich Centre for Neutron Science (JCNS) at MLZ, Garching, Germany

Chiral helimagnetic structures, which form only one-handed screw magnetic structures, have attracted attention because of the emergence of characteristic magnetic textures such as Skyrmion lattices and chiral magnetic soliton lattices. Therefore, it is very important to investigate the interplay between crystallographic and helimagnetic chirality since the sense of the rotation of helimagnetic structures strongly depends on the chiral crystal structure which allows an anti-symmetric Dzyaloshinskii-Moriya (DM) interaction. However, there have been few experimental results due to the difficulty of synthesizing homo-chiral single crystals that have only right-handed (RH) or left-handed (LH) crystal domains.

Special crystal growth technique

Helimagnetic CsCuCl_3 has a chiral crystal structure with chiral space groups of RH $P6_122$ and LH $P6_522$, as illustrated in Fig. 1 (a) and (c). However, the interplay between crystal and magnetic chirality cannot be investigated because conventional crystal growth techniques produce racemic twinned crystals that have RH and LH domains in a specimen.

Our crystal growth technique for inorganic chiral compounds makes it possible to obtain centimeter-sized homo-chiral single crystals of CsCuCl_3 with the desired handedness. To determine the helimagnetic chirality of the homo-chiral crystals of CsCuCl_3 , polarized neutron diffraction experiments were performed on the BL15 (TAIKAN) in the MLF in Japan, and on the instrument POLI at the Maier-Leibnitz Zentrum

(MLZ) in Germany. A single-crystal spherical neutron polarimetry technique using CRYOPAD was carried out at the POLI diffractometer operated with 2-axis mode. Neutron polarization and analysis were achieved by ^3He -spin filters in the incoming and scattered beams. Incomplete neutron polarization due to ^3He -spin filters were corrected by using a transmission monitor for the incoming beam and nuclear Bragg reflections for the scattered beam. The neutron spin polarization is analyzed along i, f , where i and f represent the incoming and outgoing neutron polarization, respectively. Here, x is one of three orthogonal directions and is parallel to the scattering vector Q . The omega-scan profiles of the spin-flip channels of the magnetic satellites are shown in Fig. 1. For the $(1/3, 1/3, 6-q)$ reflection in the RH crystal, shown in Fig. 1 (b), we observed the magnetic satellite peak only when the neutron polarization was along $+x, -x$. However, the opposite behaviour was observed for the LH crystal, shown in Fig. 1 (d). The results indicate that the RH crystal-line CsCuCl_3 forms a RH helimagnetic structure, and the LH crystal a LH helimagnetic structure.

Our experimental data revealed that the handedness of the magnetic helicity is coupled and directly controlled by the crystallographic lattice chirality. The results can be understood in terms of a DM interaction strongly coupled to the lattice.

[1] Y. Kousaka et al., *Monochiral helimagnetism in homochiral crystals of CsCuCl_3* ; *Phys. Rev. Mater.* 1, 071402 (2017)

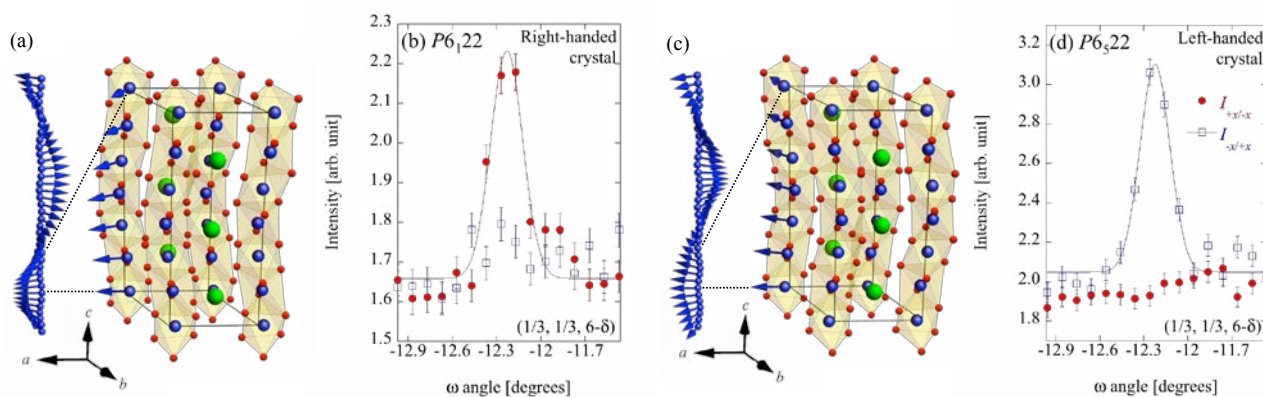


Figure 1: Chiral crystal structures of (a) right-handed (RH) (space group: $P6_122$) and (c) left-handed (LH) (space group: $P6_522$) CsCuCl_3 . Arrows in a Cu chain in (a) and (c) represent RH and LH helimagnetic structures, respectively. Spin-flip channels omega-scan profiles of $(1/3, 1/3, 6-q)$ magnetic Bragg reflections for (b) RH ($P6_122$) homo-chiral crystal and (d) LH ($P6_522$) homo-chiral crystal. Filled circles and open squares represent the measured intensities, continuous lines are gaussian fits to the data.

A. Sazonov¹, V. Hutanu¹, M. Meven¹, G. Roth², H. Murakawa³, Y. Tokura⁴, V.K. Guduru⁵, L.C.J.M. Peters⁵, U. Zeitler⁶, L.F. Kiss⁶, D. Szaller⁷, B. Náfrádi⁸, I. Kézsmárki⁷

¹Institute of Crystallography, RWTH Aachen University and Jülich Centre for Neutron Science (JCNS) at MLZ, Forschungszentrum Jülich GmbH, Garching, Germany; ²Institute of Crystallography, RWTH Aachen University, Germany; ³JST, University of Tokyo and Department of Physics, Osaka University, Japan; ⁴QPEC, University of Tokyo and RIKEN CEMS, Wako, Japan; ⁵HFML-EMFL and IMM, Radboud University, The Netherlands; ⁶Institute for Solid State Physics and Optics, Wigner RCP, HAS, Budapest, Hungary; ⁷Department of Physics and Magneto-Optical Spectroscopy Research Group, BME, Budapest, Hungary; ⁸École Polytechnique Fédérale de Lausanne, LNNME, Lausanne, Switzerland

Recently, several members of the melilite family, such as $\text{Ca}_2\text{CoSi}_2\text{O}_7$, $\text{Sr}_2\text{CoSi}_2\text{O}_7$, $\text{Ba}_2\text{MnGe}_2\text{O}_7$ and $\text{Ba}_2\text{CoGe}_2\text{O}_7$, have been found to exhibit static as well as dynamic magnetoelectric effects. Precise information on the atomic positions, along with the spin order (crystal and magnetic structures), is essential to unravelling the complex physics behind the magnetoelectric behaviour of the melilite compounds.

In order to fill the gap in the magnetic structure information available on $\text{Ca}_2\text{CoSi}_2\text{O}_7$, we performed single-crystal neutron diffraction experiments as well as bulk magnetization measurements at temperatures between 1.7 and 10 K and fields up to 32 T. The zero-field studies were carried out on the 4-circle diffractometer HEiDi at the MLZ, using $\lambda = 1.169 \text{ \AA}$. A total of 4790 reflections with $\sin\theta/\lambda \leq 0.7 \text{ \AA}^{-1}$ were measured at 2.5 K

The low-temperature commensurately modulated lock-in state of $\text{Ca}_2\text{CoSi}_2\text{O}_7$ at 10 K is described by the orthorhombic space group (SG) $P2_12_12$ with a $3 \times 3 \times 1$ supercell, in comparison to the high-temperature unmodulated phase with SG $P-42_1m$. Below $T_N \approx 5.7 \text{ K}$, an additional magnetic contribution to the Bragg reflection intensities appears, corresponding to the commensurate magnetic order with propagation vector $\mathbf{k} = \mathbf{0}$. In order to solve the magnetic

structure, we used the concept of magnetic space groups (MSGs). Only the following distinct types of magnetic ordering of k -maximal symmetry are possible in $\text{Ca}_2\text{CoSi}_2\text{O}_7$: model $M1$ (MSG $P2_12_12$), model $M2$ (MSG $P2'_12'_12$) and twinned model $M3/M4$ (MSG $P2'_12'_12$). All models were used in the refinement process. It was found that only the twinned model $M3/M4$ fits the experimental data well. Moreover, we performed an additional refinement in the simplified magnetic model which assumes that all the cobalt atoms have (1) equal in-plane AF moments, (2) equal in-plane F components, and (3) zero out-of-plane F components. Both twinned $M3/M4$ (14 parameters) and its simplified (2 parameters) magnetic structures are shown in Fig. 1. Thus, in zero magnetic field, the MSG is $P2'_12'_12$ with AF order along the $[100]$ or $[010]$ axes for two types of 90° twin domains, while neighboring spins along the $[001]$ axis are FM-ordered. The ordered moment with a magnitude of around $2.8 \mu_B/\text{Co}^{2+}$ at 2.5 K lies in the ab plane. A noncollinear spin arrangement due to small canting within the ab plane is allowed by symmetry and leads to the existence of the tiny spontaneous magnetization below T_N .

Experimental basis for describing magnetoelectric phenomena

Our neutron scattering experiments, as well as bulk magnetization studies, indicate pronounced differences between the magnetic state of $\text{Ca}_2\text{CoSi}_2\text{O}_7$ and similar magnetically ordered melilites such as $\text{Ba}_2\text{CoGe}_2\text{O}_7$ and $\text{Sr}_2\text{CoSi}_2\text{O}_7$. The structural parameters obtained (both for the nuclear and magnetic order) can serve as a sound experimental basis from which to develop microscopic models describing the multiferroic nature and the peculiar magnetoelectric phenomena in melilites.

[1] A. Sazonov et al., *Magnetic structure of the magnetoelectric material $\text{Ca}_2\text{CoSi}_2\text{O}_7$* , *Phys. Rev. B* 95, 174431 (2017)

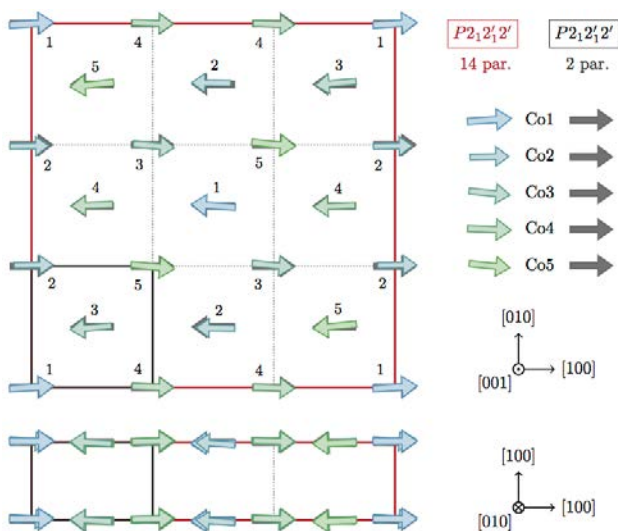


Figure 1: Magnetic structure in the full MSG $P2'_12'_12$ (14 parameters) and its simplified (2 parameters) models, according to our neutron diffraction data at 2.5 K. The small unit cell of the high-temperature unmodulated phase with SG $P-42_1m$ is plotted in gray while the large $3 \times 3 \times 1$ supercell of SG $P2_12_12$ is shown in red. The five inequivalent cobalt sites are numbered.

Y. Khaydukov^{1,2,3}, A. M. Petrzik⁴, I. V. Borisenko⁴, A. Kalabukhov^{5,3}, D. Winkler⁵, T. Keller^{1,2}, G. A. Ovsyannikov^{4,5}, B. Keimer¹

¹Max-Planck-Institute for Solid State Research, Stuttgart, Germany; ²Heinz Maier-Leibnitz Zentrum (MLZ), Garching, Germany; ³Skobeltsyn Institute of Nuclear Physics, Moscow State University, Moscow, Russia; ⁴Kotel'nikov Institute of Radio Engineering and Electronics, Russian Academy of Sciences, Moscow, Russia; ⁵Department of Microtechnology and Nanoscience, Chalmers University of Technology, Gothenburg, Sweden

The rich field of complex oxide heterostructures (COH) is the subject of intensive theoretical and experimental study due to the large number of interface phenomena that arise from reconstruction, strain, proximity effects etc. One advantage of complex oxides is the similarity in their crystal structure, which allows heterostructures with interfaces of extremely high quality to be built. Another advantage is the high sensitivity of different types of ordering e.g. magnetic ordering, superconductivity or the metallic state that appears in COH in response to an external influence such as a magnetic or electric field, and internal such as doping or crystal structure strain. Magnetic ordering in COH features such phenomena as a double exchange mechanism, strong electron-electron correlations and the correlation of magnetic and transport properties that make them attractive materials for developing new functional devices. One example is $\text{La}_{0.7}\text{Sr}_{0.3}\text{MnO}_3/\text{SrRuO}_3$ (LSMO/SRO) heterostructures that show anomalous magnetic, magneto-transport, photoconductivity and thermal transport phenomena.

Polarized Neutron Reflectometry (PNR) is one of the key techniques employed nowadays to study the magnetic properties of COHs. The specular reflection of neutrons arises due to the presence of optical potential contrast. For spin-up (spin-down) neutrons, the potential is the sum (difference) of the nuclear ρ_o and magnetic ρ_m contributions: $\rho^\pm(z) = \rho_o(z) \pm \rho_m(z)$. In order to obtain information about the magnetic depth profile, one has to measure the reflectivities in quite a broad Q-range, which is a time-consuming

task taking into account the small sample area ($\sim 25\text{mm}^2$) and nuclear contrast in COHs. We propose to use magnetic contrast waveguides (MWG) which allow depth selective measurements in a narrow Q-range around the critical edge. A scheme of a typical waveguide is shown in Fig. 1a. It is an A/B/C trilayer where the nuclear SLD of layer B is much smaller than the SLDs of layers A and C. Multiple reflection in the middle layer leads to the formation of the standing wave which, under certain conditions (resonance or waveguide modes), is resonantly enhanced. Waveguide enhancement has already been proposed to produce a sub- μm coherent neutron beam, miniaturize nuclear energy production or enhance spin-flip (SF) scattering. The latter, being of purely magnetic origin, is a very important channel for the study of magnetism. Classical nuclear-contrast waveguides significantly increase the intensity of SF scattering but have very little depth sensitivity. The MWG proposed here also enhance the SF intensity but provide a very good depth selectivity of the different resonance modes. The recipe for the MWG is illustrated in (Fig. 1b, c). The B/C bilayer with a magnetic B layer investigated should be deposited on the D substrate with SLD higher than those of layers B and C, i.e. $\rho_B \approx \rho_C < \rho_D$. The next step is to cover the bilayer with the layer A having nuclear SLD $\rho_A \approx \rho_B, \rho_C$, so that layers A, B and C forms structure having (almost) no nuclear contrast. The presence of a magnetic moment in B layer leads to the increase (decrease) of the total SLD of B layer for spin-up (spin-down) neutrons. As a result, a well-shaped SLD profile will be formed for spin-up and spin-down neutrons with the center in the C and B layer, correspondingly. Thus, for the differently polarized neutron beam a waveguide mode will be formed in different layers, providing the necessary depth selectivity.

To give an experimental example, the magnetic state of $\text{Au}(24\text{nm})/\text{La}_{0.7}\text{Sr}_{0.3}\text{MnO}_3(53\text{nm})/\text{SrRuO}_3(50\text{nm})//\text{NdGaO}_3$ was studied at the NREX reflectometer. By covering the system with the layer of gold, a waveguide structure was created where the first and second resonance spin-flip peaks are sensitive mainly to the magnetic state of the manganite and ruthenate sub-systems, respectively. Using this approach, we were able to detect a suppression of the 2nd waveguide peak at $T < 130\text{K}$ after field cooling. Such a suppression is interpreted as the appearance of a small positive in-plane magnetic moment of only $0.34 \mu_B/\text{Ru}$ in the ruthenate layer.

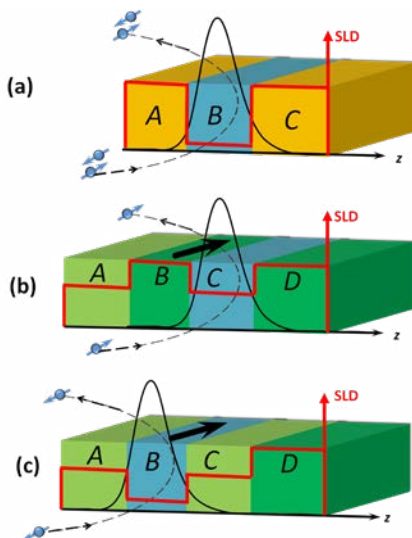


Figure 1: Sketch of the nuclear-contrast (a) and magnetic-contrast waveguide seen by spin-up (b) and spin-down(c) neutrons. The layer B in (b) and (c) is magnetic with the vector of magnetization shown by a black arrow. As a result the SLD depth profile (red line) is different for spin up (b) and spin-down (c) neutrons.

[1] Y. Khaydukov et al., *Magnetic waveguides for neutron reflectometry*; *Phys. Rev. B* 96, 165414 (2017)

A. Syed Mohd¹, S. Pütter¹, S. Mattauch¹, A. Weber¹, T. Brückel^{1,2}

¹Jülich Centre for Neutron Science (JCNS) at MLZ, Forschungszentrum Jülich GmbH, Garching, Germany; ²Jülich Centre for Neutron Science (JCNS) and Peter Grünberg Institute (PGI), Forschungszentrum Jülich GmbH, Jülich, Germany

MARIA is a neutron reflectometer which allows nuclear and magnetic depth profiling of thin films and multilayers. Nowadays, molecular beam epitaxy (MBE) is a well-established technique and, thus, an essential tool in the preparation of the highest quality samples. For the detailed investigation of thin films, a MBE setup was placed close to MARIA in a nearby building. However, to prevent air sensitive thin films being exposed to ambient atmosphere for *ex-situ* PNR measurements, normally a noble metal is subsequently deposited on top of them. But, capping them may change their physical properties. Hence, the investigation of the intrinsic properties of these thin films using PNR must be performed in UHV. However, due to the limited space and geometrical restrictions at MARIA, a UHV system for thin film growth and *in-situ* PNR measurements cannot be realized on-site. Therefore, we developed a handy portable transport chamber which allows the transfer of MBE grown thin films to MARIA for PNR measurements in UHV conditions [1].

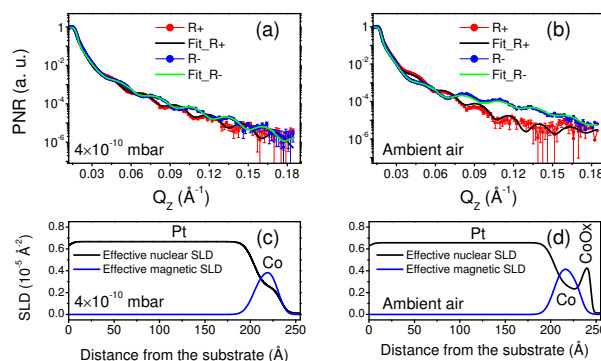


Figure 2: PNR of Co(3 nm)/Pt(20 nm)/MgO(001) measured (a) in UHV using portable transport chamber (b) in ambient air. SLD profile obtained from fitting the PNR data measured (c) in UHV conditions and (d) in ambient air.

This small lightweight (~10 kg) portable transfer chamber, as shown in Fig. 1, is attached to the MBE setup. The pressure in the transport chamber is kept well below 10^{-9} mbar during transfer and PNR measurement. Fig. 2 shows the PNR measurements on a Co (3 nm) thin film, deposited on a Pt (20 nm) buffer layer, measured under UHV condition using the chamber and in ambience. The magnetic field (200 mT) during the measurement was kept parallel to the polarization axis of the neutron beam. Qualitatively, one may notice from Fig. 2(a) and 2(b) that PNR of the same Co thin film measured in UHV differs from that measured in air. Obviously, Co thin films react with air. The fitting of the PNR data shows that a non-magnetic Co-oxide (CoOx) layer is formed at the Co/air interface when exposed to ambient atmosphere. The nuclear and magnetic scattering length density (SLD) profiles of the sample obtained from the fitting of the PNR data measured in UHV and in ambience are shown in Fig. 2 (c) and (d), respectively.

In summary, we observe that our new UHV transport chamber does protect thin Co oxide layers from oxidation. So, samples which are delicate to handle in ambient conditions can be successfully measured using our versatile UHV transport chamber. Access to the MBE system, as well as to the transport chamber, can be booked via the MLZ user office system, in combination with an application for beam time at neutron instruments such as MARIA or NREX.

[1] A. Syed Mohd et al., A versatile UHV transport and measurement chamber for neutron reflectometry under UHV conditions; *Rev. Sci. Instr.* 87, 123909 (2016)

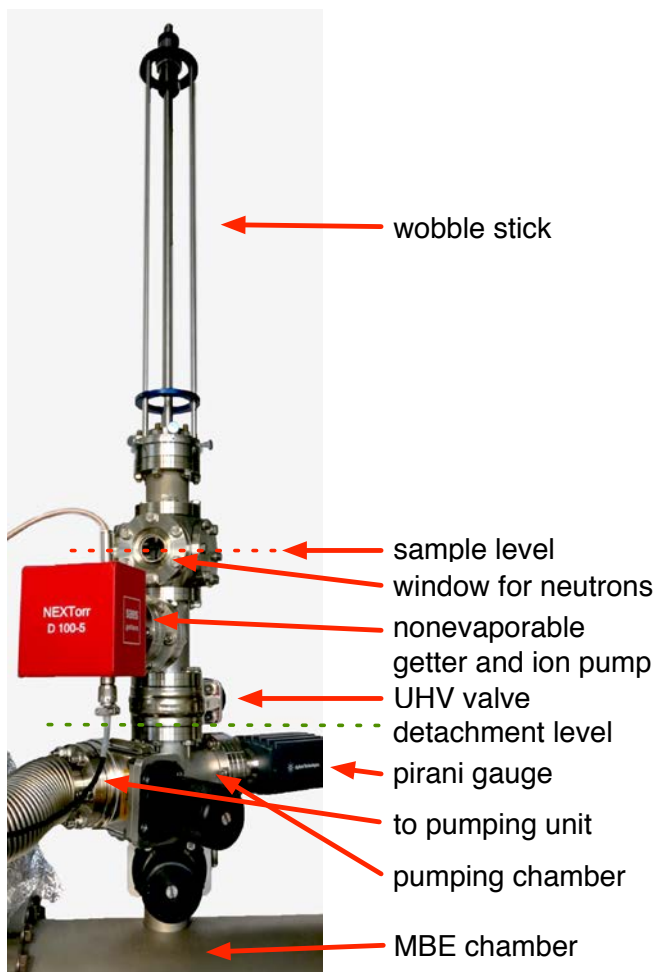


Figure 1: Photo of the UHV portable transfer chamber attached to MBE setup.

M. Rossbach¹, A. Hable²

¹Forschungszentrum Jülich GmbH, Jülich, Germany; ²TU Wien, Atominsttitut, Wien, Austria

Precise nuclear data are essential for the design of nuclear fuel, the safe operation of nuclear power plants and research reactors and for scientific and environmental investigations as well as for basic research e.g. in nuclear synthesis. At the beam line SR10 of the reactor at the Heinz Maier-Leibnitz Zentrum (MLZ) in Garching a beam of fission neutrons from a 95%-enriched ²³⁵U converter providing 10⁸ neutrons cm⁻²s⁻¹ with a quasi-Watt energy distribution is available. This beam, mainly operated for the irradiation of cancer patients can also be used in combination with a well-shielded gamma spectrometer for prompt and delayed gamma spectroscopy (**F**ast **N**eutron **G**amma **S**pectroscopy, FaNGaS). Fast neutrons excite nuclides primarily in (n,n'γ) reactions which are complementary to (n,γ) reactions in thermal or cold neutron irradiations.

Small samples of actinides previously used for a PhD thesis (Ch. Genreith, 2015) ²³⁸U, ²³⁷Np, and ²⁴²Pu were irradiated to record prompt spectra followed by decay measurements after irradiation. A number of fission products induced by fast fission were identified and their reaction rates were calculated to extract integral fission cross sections. The use of tabulated cumulative fission yields made it possible to de-

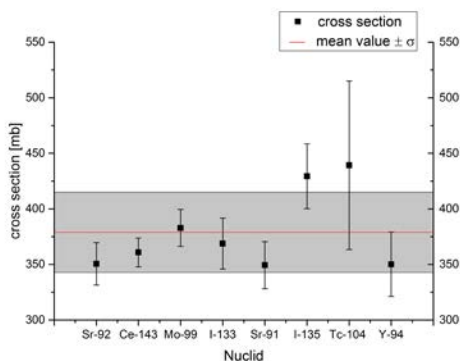


Figure 1: Integral fission cross section of ²³⁸U calculated from individual fission product results.

termine the integral fission cross sections using formula (1).

Ac-tinide	Experimental value	ENDF adopted integral value	JEFF adopted integral value	JENDL adopted integral value
²³⁸ U	379 ± 37 mb	336.2 mb [351.8 ; 318.9]	336.6 mb [365.7 ; 323.5]	335.5 mb [349.6 ; 319.4]
²³⁷ Np	3.0 ± 0.4 b	1,389 b [1.420 ; 1.372]	1.365 b [1.380 ; 1.350]	1.380 b [1.404 ; 1.368]
²⁴² Pu	2.2 ± 0.4 b	1.185 b [1.214 ; 1.171]	1.203 b [1.250 ; 1.177]	1.186 b [1.219 ; 1.172]

Table 1: Summary of results in comparison with adopted integral fission cross sections of the nuclear data libraries ENDF, JEFF, and JENDL (in brackets max. and min. values).

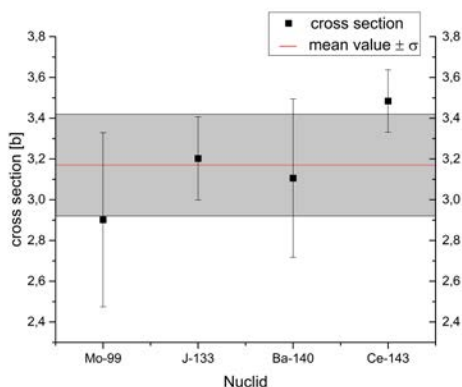


Figure 2: Integral fission cross section of ²³⁷Np calculated from individual fission product results.

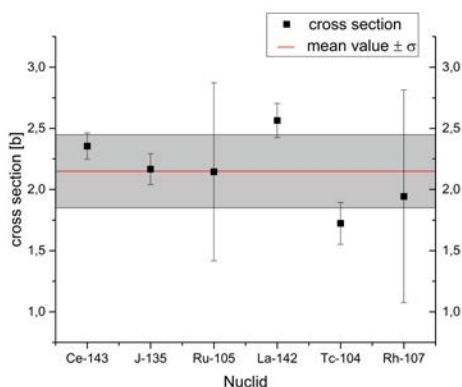


Figure 3: Integral fission cross section of ²⁴²Pu calculated from individual fission product results.

$$R = (\bar{\sigma}) \cdot N \cdot \Phi \cdot Y \tag{1}$$

- R = reaction rate,
- $\bar{\sigma}$ = integral fission cross section,
- N = number of particles involved,
- Φ = integral neutron flux, and
- Y = weighted mean cumulative fission yield extracted from JEFF3.1.

(n,f) Cross sections for ²³⁸U, ²³⁷Np and ²⁴²Pu were determined as 0.38 ± 0.04, 3.0 ± 0.4, and 2.15 ± 0.4 barn, respectively. In comparison to calculated values extracted from differential data in ENDF, JEFF or JENDL our data are slightly higher and demonstrate the urgent need to validate fast fission nuclear data experimentally, e.g. in the beam of SR10.

[1] A. Hable et al., Determination of integral fast fission cross sections (n,f) of ²³⁸U, ²³⁷Np, and ²⁴²Pu in a directed fission neutron beam at FRM II, Garching; J. Radioanal. Nucl. Ch. 314(2), 1471 (2017)

Engineers changing the plug for beam tube no. 6a to insert the future ultra-cold neutron source.



Instrumental Upgrades & Services

News from the instruments

M. Dodenhöft¹, A. Feoktystov², T. Gigl¹, D. Gorkov³, O. Holderer², C. Hugenschmidt¹, H. Keppler⁴, M. Meven^{2,5}, S. Pasini², J. Peters¹, A. Radulescu², M. Singer¹, N. Walte⁴, A. Weber², R. Georgii¹

¹Heinz Maier-Leibnitz Zentrum (MLZ), Technical University of Munich, Garching, Germany; ²Jülich Centre for Neutron Science (JCNS) at MLZ, Forschungszentrum Jülich GmbH, Garching, Germany; ³II. Physikalisches Institut, University of Cologne at MLZ, Garching, Germany; ⁴Bayerisches Geoinstitut, Universität Bayreuth at MLZ, Garching, Germany; ⁵Institute of Crystallography, RWTH Aachen University at MLZ, Garching, Germany

The year 2017 brought a lot of new developments and upgrades to the MLZ: The Spin-Echo instrument (J-NSE), the Small Angle Neutron Scattering instrument KWS-2, the hot single diffractometer HEIDI as well as several new options at the positron source NEPOMUC and in the sample environment pool. Furthermore, two new instruments are approaching completion: The three-axis instrument KOMPASS and the high-pressure instrument SAPHiR.

Like a Phoenix: The new J-NSE

The neutron spin echo spectrometer J-NSE added a new chapter to its nomadic and colourful neutron scattering instrument life. During the first period of operation, it was located at the Jülich DIDO reactor, from where it was transferred to the FRM II more than 10 years ago. After a decade of operation at the MLZ, it transformed again. This time it was not a relocation of the instrument, but rather a cardiac transplantation. The main precession coils, until then water cooled copper coils bearing a maximum of 440 Amps at 360 Volts, were removed in March 2017 and replaced by superconduct-

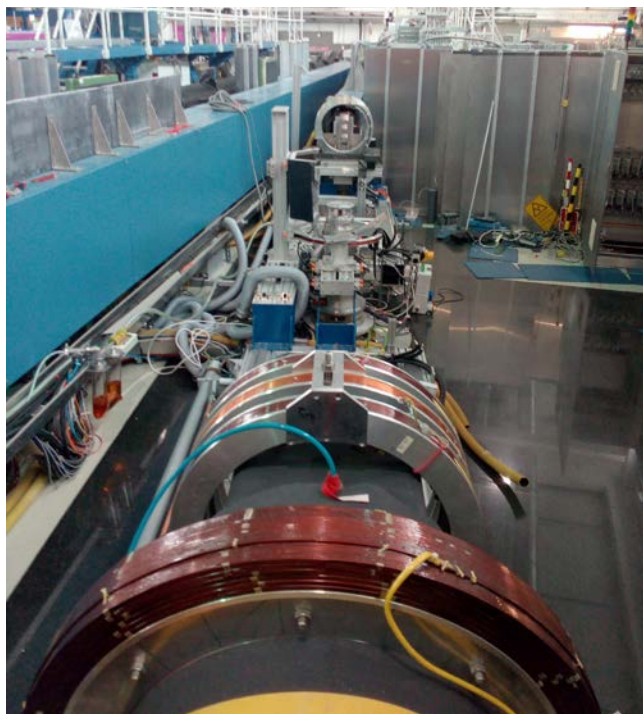


Figure 1: The empty carrier structure after removal of the normal conducting main coils.



Figure 2: The new superconducting main precession coils in their cryostats in place at the J-NSE.

ing segmented main coils that provide a much more homogeneous magnetic field and significantly improve the performance of the J-NSE. A large team of physicists, engineers and technicians from Jülich and Garching made an effort to keep the time on the operating table short. During the summer cycle, the J-NSE instrument recovered from anesthesia and found its way back to life, feeling neutrons on the detector again. The summer cycle was dominated by adjustments and tuning of the auxiliary and correction coils. The concept of improving the resolution by an optimized field shape, thereby making it possible to correct for higher magnetic field integrals with the available correction coils, worked out and allowed the Fourier time range at our standard wavelength of 8 Å to be increased from 40 ns to 100 ns. The new setup will pay off, especially for the time range up to 200 ns, which is now accessible with a wavelength of 10 instead of 15 Å and with a much higher intensity. The cycle ended with a successful first test experiments and, from the next cycle on, the instrument will be able to digest user experiments again, with a much better performance than before. Some time for additional adjustments will be used for further optimization of the many new parameters now available, which is particularly important for very high resolution at longer wavelengths.

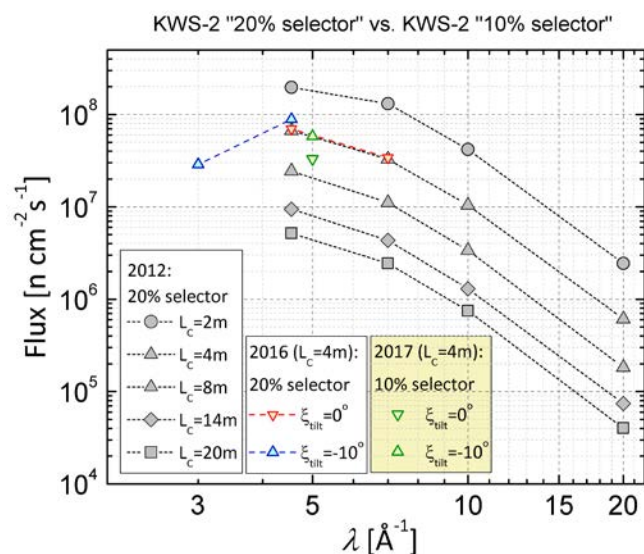


Figure 3: The neutron flux at the sample position of KWS-2 measured in different instrument configurations.

Dual operation mode high resolution / high intensity at the SANS diffractometer KWS-2

KWS-2 is primarily a dedicated high intensity SANS diffractometer which, in the instrument concept, is provided by a specially designed neutron guide system and a velocity selector that facilitates a relaxed resolution, $\Delta\lambda/\lambda = 20\%$ [1]. Following demands from the user community regarding improvements in resolution, the instrument was equipped with a double-disc chopper with a variable opening slit window and time-of-flight (TOF) data acquisition option [2]. The chopper, used together with the velocity selector, allows for the tuning of the wavelength resolution within a broad range, from the standard configuration (only selector) down to 2 %. The instrument gained hugely in performance for applications which require wavelength resolutions $\Delta\lambda/\lambda \leq 5\%$ at wavelengths for which no dedicated velocity selectors exist. However, for wavelength resolutions in the range $10\% \leq \Delta\lambda/\lambda \leq 20\%$ used in typical SANS experiments, dedicated velocity selectors present a clear intensity advantage over the set-up involving the chopper. Detailed McStas simulations have shown that, by tilting a selector designed for a resolution of $\Delta\lambda/\lambda = 10\%$ over an angle of $\xi_{\text{tilt}} = -10^\circ$ with respect to the beam axis, a gain in intensity based on the resolution relaxation up to $\Delta\lambda/\lambda = 20\%$ can be obtained. The results have been confirmed by gold foil activation (Fig. 3) and by measurements on the silver behenate (AgBeh) peak structure and the size standards SiO_2 particles with very small polydispersity in size (Fig. 4). They were carried out with different neutron wavelengths λ and in different positioning configurations of two selectors, one (selector 1) delivering a standard $\Delta\lambda/\lambda = 10\%$ and another (selector 2) -

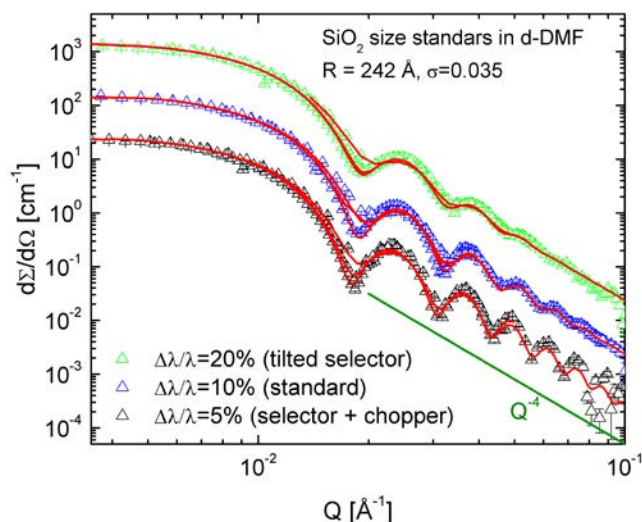


Figure 4: The effect of different instrument resolution configurations at KWS-2 observed on results from SiO_2 size standards; symbols - experimental curves, lines - fitted results using the spherical form factor with size polydispersity and resolution included.

a standard $\Delta\lambda/\lambda = 20\%$. The tilting set-up of the KWS-2 selector was designed and installed in 2016 following collaborative work between the JCNS and the FRM II Neutron Optics Group. Since summer 2017, the use of a velocity selector (ASTRIUM GmbH) that provides either a $\Delta\lambda/\lambda = 10\%$ or $\Delta\lambda/\lambda = 20\%$, depending on its parallel or inclined positioning with respect to the beam axis, is the main monochromatization method currently used at KWS-2. The set-up also makes it possible to both achieve lower wavelengths, down to $\lambda = 2.8\text{ \AA}$ (Fig. 5), hence a higher $Q_{\text{max}} = 1\text{ \AA}^{-1}$, with significant intensity, and continue to maintain a very high flux for experiments that require intensity at the expense of resolution by using monochromatic beams with $\Delta\lambda/\lambda \cong 20\%$.

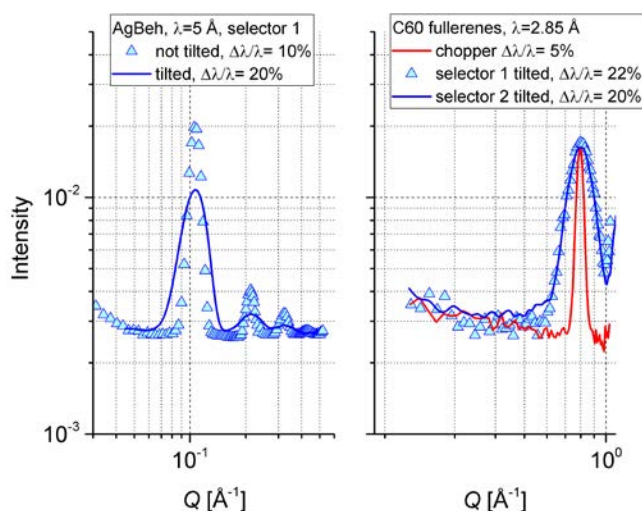


Figure 5: The effect of selector tilting on instrumental resolution and Q_{max} at KWS-2, as evidenced on wavelength calibration standards. For the lowest wavelength reached (2.85 \AA), the wavelength spread is always 20 % regardless of the selector type, due to the cut-off of the neutron guide [2].

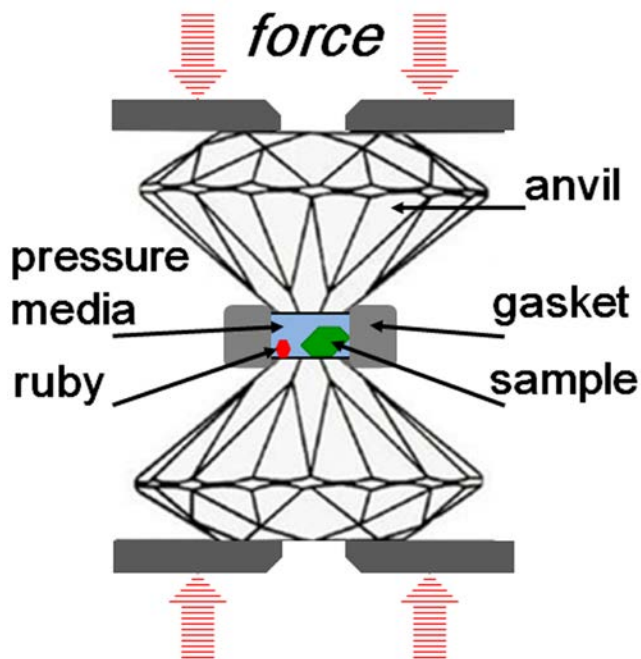


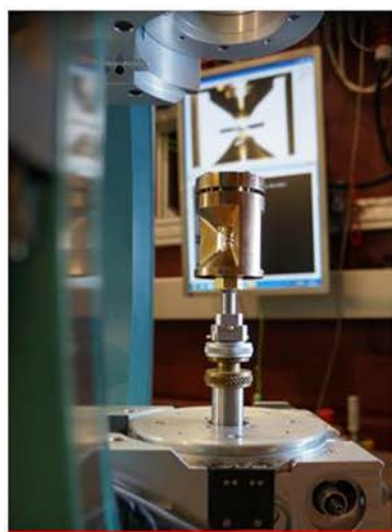
Figure 6: Scheme of pressure cell for single crystals.

HEiDi: Towards extreme conditions and small samples

Within the BMBF project 05K16PA3 „Erweiterung des heißen Einkristalldiffraktometers HEiDi für Experimente an kleinen Proben < 1 mm³ und mit Druckzellen“ (RWTH Aachen University, Prof. G. Roth), which aims to improve the primary optics, the single crystals for the new Cu (220) monochromator were cut at JCMS/FZ Jülich and characterized at Universität Göttingen (Prof. G. Eckold). Final calculations and measurements were performed for the planned new guide and solid state collimators. In addition, new pressure cells were tested at the instrument (Fig. 6 and 7) and as a benchmark the smallest visible single crystal size was determined for the existing optical components, yielding a minimum size of < 0.1 mm³.

IR Furnace with exchange gas option and tests at HEiDi

The aim of this furnace is to facilitate neutron diffraction studies by providing precise control of the gas atmosphere at elevated temperatures up to 1000 °C. The starting point is an infrared furnace design (IRF), developed at the MLZ, that is already in service and has been used for neutron diffraction studies for many years. This furnace consists of a spherical body that employs four crossed halogen bulbs to heat a sample located in the center via infrared radiation. It is tailored to fit into an Eulerian cradle that is installed at different instruments of the facility. Despite the good performance of this set-up and the ability to reach temperatures higher than 1200 °C under high vacuum conditions, it was not possible to carry out research on samples at the temperatures mentioned and dedicated gas atmospheres. In order to do so, the design was modified within a joint MaMaSELF master's thesis together with ICGM (University Montpellier) to allow the installation of a quartz capillary that provides the exchange gas volume close to the sample, but separated from the mandatory isolation vacuum. A new sample holder that fits into the capillary was built, providing reduced heat conduction. This was achieved by making some modifications to the lower body. Furthermore, new connectors for the four halogen lamps were designed and installed together with a new vacuum adaptor and a new lower base to fix the whole construction in the Eulerian cradle (Fig. 8). The modifications were also implemented with the objective of allowing easier rotations when mounted in the cradle and more convenient handling overall. The total heat management of the furnace was checked by performing intense thermal simulations using COMSOL Multiphysics heat conduction and ray tracing modules. In addition to the furnace, a gas handling system was designed and manufactured in order to control the gas mixture inside the capillary with high precision. Following successful tests, single crystal neutron diffraction experi-



panoramic DAC - HEiDi



transmission DAC - HEiDi



transmission DAC - IPDS-II

Figure 7: Different cell designs (A. Grzechnik, RWTH Aachen University), (left) panoramic, (middle + right) transmission cell for usage in both X-ray and neutron instruments.

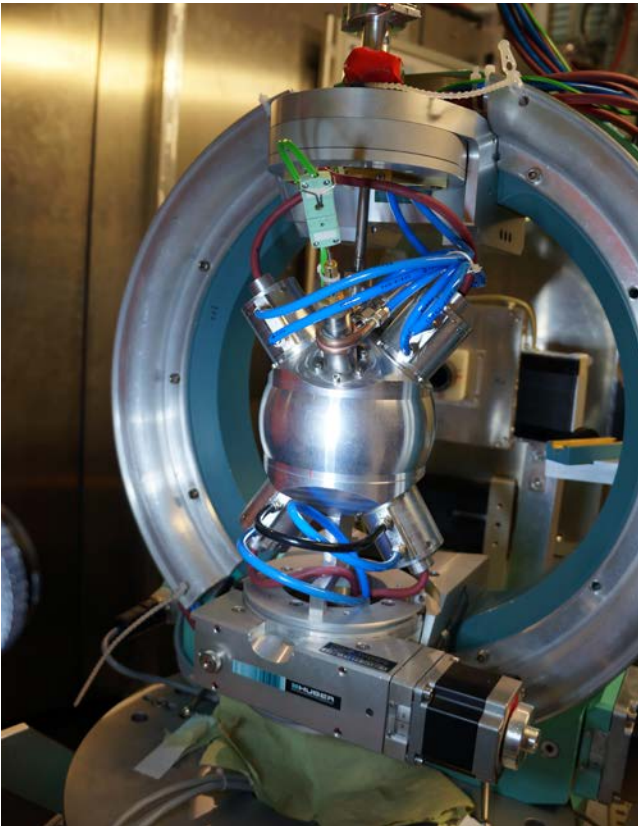
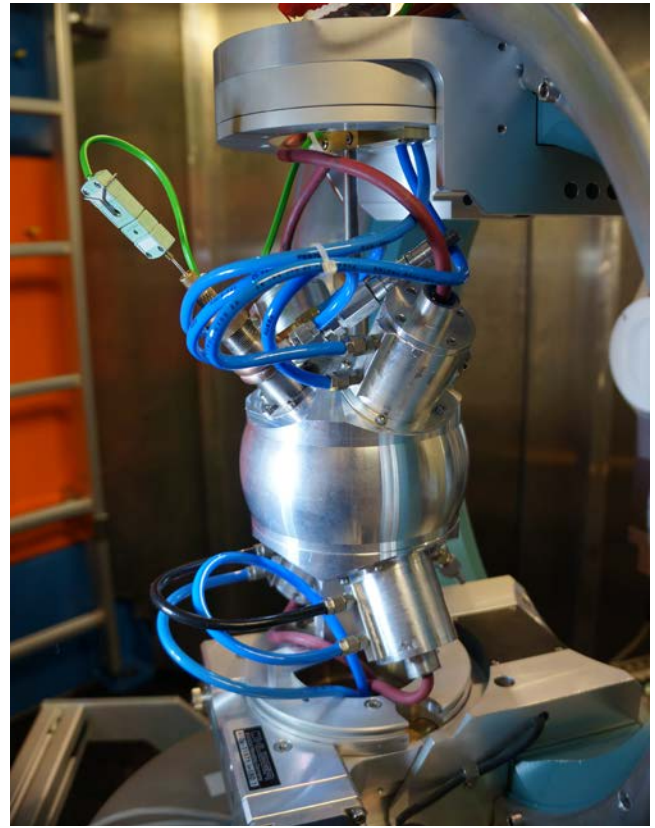


Figure 8: The furnace mounted in the Eulerian cradle at HEiDi.



ments were performed at the instrument HEiDi on the ionic conductor $\text{Pr}_2\text{NiO}_{4+\delta}$ up to $> 900^\circ\text{C}$ and pure Ar and mixed Ar/ O_2 gas mixtures in order to tune and to study the influence of the interstitial oxygen O_{int} in this structure which consists of layers of NiO_6 octahedra. Fig. 9 illustrates the structural effect even for very small amounts of oxygen uptake, showing neutron scattering densities of $\text{Pr}_2\text{NiO}_{4+\delta}$ in the $2a \times 2a$ projection of the 14/mmm unit cell with positions of the Pr, O_{ap} and O_{int} at $z = 0.14, 0.17$ and 0.25 respectively. The left and middle Fig. 9 show tetragonal (900°C) and orthorhombic symmetry (450°C) with the absence of any libration modes along [110] for the stoichiometric phase. An uptake of even small quantities of oxygen (here 0.01) at 450°C (right) turns the symmetry from orthorhombic to tetragonal and modifies

completely the nuclear densities, clearly showing displacements along [110].

Defect spectroscopy with the new positron microbeam at the coincident doppler broadening spectrometer of NEPOMUC

The coincident doppler broadening (CDB) spectrometer was successfully upgraded in order to provide a threefold moderated positron beam at the high intensity positron source NEPOMUC (Neutron induced positron source Munich, Fig. 10). The new positron microbeam yields a minimal diameter of $33\ \mu\text{m}$ over a large scanning range of up to $19 \times 19\ \text{mm}^2$. To achieve this goal, a new brightness enhancement system in transmission geometry, consisting of a Ni(100) remoderation

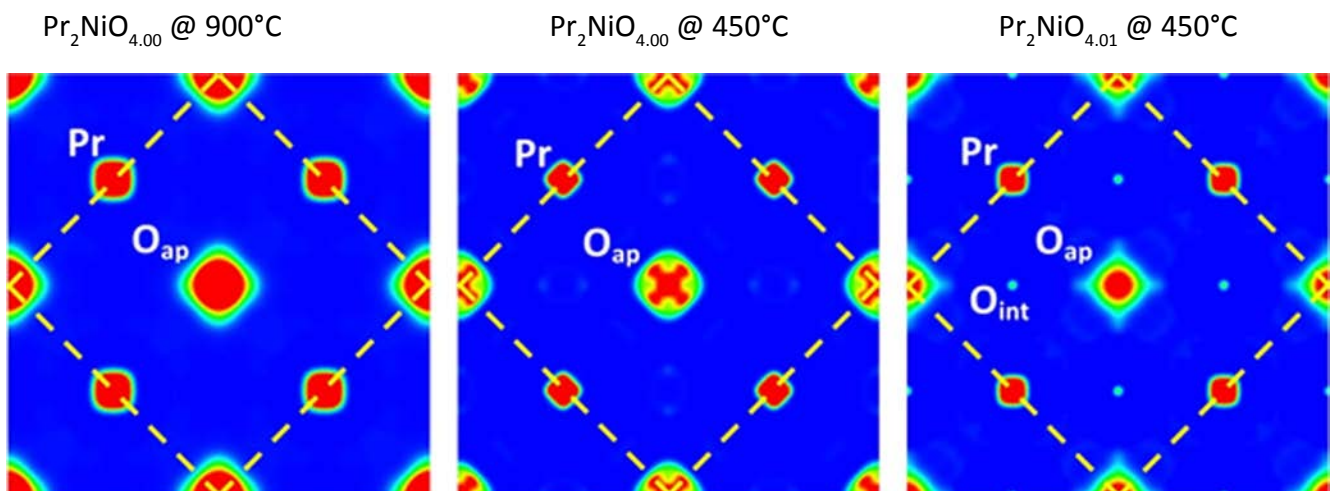


Figure 9: T and δ dependent neutron scattering densities of $\text{Pr}_2\text{NiO}_{4+\delta}$ (data from HEiDi).

foil with a thickness of 100 nm and a moderation efficiency of 9.6 %, was successfully put into operation [3]. By implementing two new electrostatic lens systems – one for focusing the beam onto the remoderation foil and a second for focusing onto the sample – the diameter of the two-fold moderated positron beam of NEPOMUC could be reduced by a factor of 60. The new spectrometer now allows defect studies by conventional Doppler Broadening Spectroscopy (DBS) and element-specific measurements by coincident DBS at the near surface and in the bulk of a sample by varying the positron implantation energy in the range from 0.5 to 30 keV with high spatial resolution. Two piezo positioners facilitate high-precision scanning of the samples. By introducing three new beam monitors, the quality and shape of the beam can be examined and adjusted by altering the magnetic correction and electrostatic lens fields, resulting in a very fast start-up of the user measurements. First measurements on laser beam welds fabricated out of high strength age hardened Al alloys have demonstrated the capabilities of the upgraded instrument. The visualization of the defect distribution revealed a very sharp transition between the raw material and the welded zone, as well as a very small heat affected zone. Additional coincident DBS allowed the detection of Cu precipitates and their dissolution in the welded zone [3].

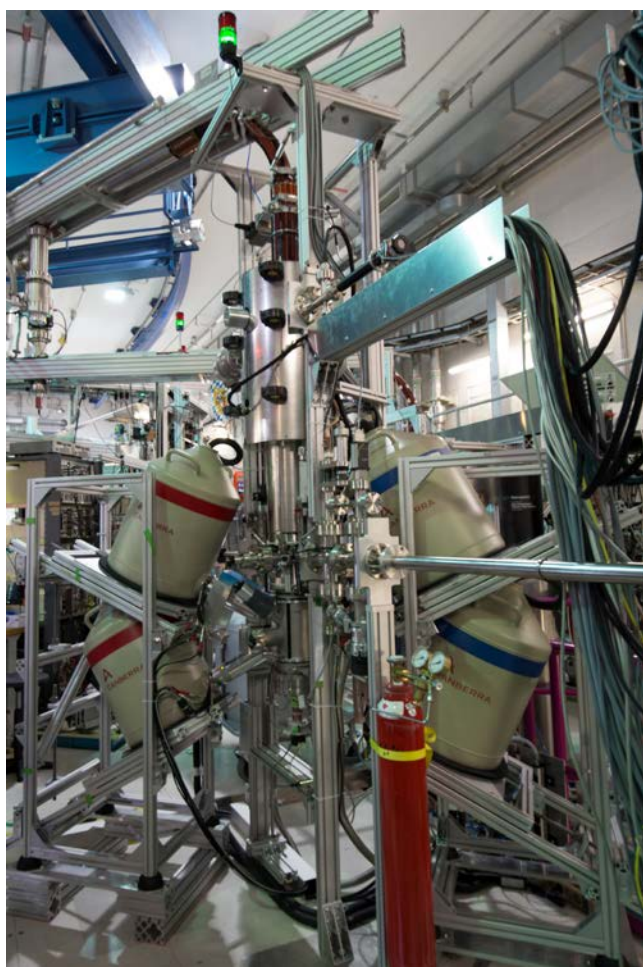


Figure 10: CDB spectrometer upgrade in the experimental hall of the FRM II.

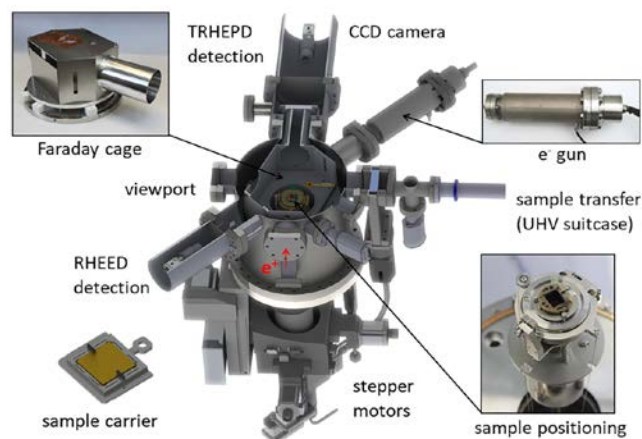


Figure 11: Layout of the TRHEPD UHV chamber.

Development of a novel reflection high-energy positron diffractometer at NEPOMUC

The surface structure of a crystal determines many fundamental physical processes such as the de- and adsorption of atoms and molecules, surface diffusion or chemical reactions. Precise knowledge of this is thus crucial in optimizing catalytic techniques. Furthermore, the arrangement of surface atoms is an important input parameter for density functional theory (DFT) calculations of the electronic structure at the surface. It has been shown that Total Reflection High-Energy Positron Diffraction (TRHEPD) is an ideal technique for determining the structure of the topmost and the immediate subsurface atomic layer of crystal surfaces [4]. Positrons experience a positive crystal potential and are therefore repelled from the surface. In contrast to electrons, which are used in Reflection High-Energy Electron Diffraction (RHEED), positrons exhibit the phenomenon of total reflection when the glancing angle is smaller than the critical angle θ_c . For this reason, TRHEPD features outstanding surface sensitivity. In addition, information on near-surface layers can be obtained by increasing the glancing angle above the critical angle. Currently, we are developing a new TRHEPD setup that will be coupled to the high-intensity positron source NEPOMUC. Since the NEPOMUC beam provides an intensity of 10^9 moderated positrons per second, we expect a further reduction of the measurement time and improved statistics as a result of using the new diffractometer. A cross-sectional view of the vacuum chamber is shown in Fig. 11. The TRHEPD setup features UHV down to 10^{-10} mbar, sample temperatures up to 1000 °C and a RHEED system for complementary measurements. In combination with the existing Surface Spectrometer (SuSpect), NEPOMUC will provide a unique ensemble to characterize surfaces using positrons.

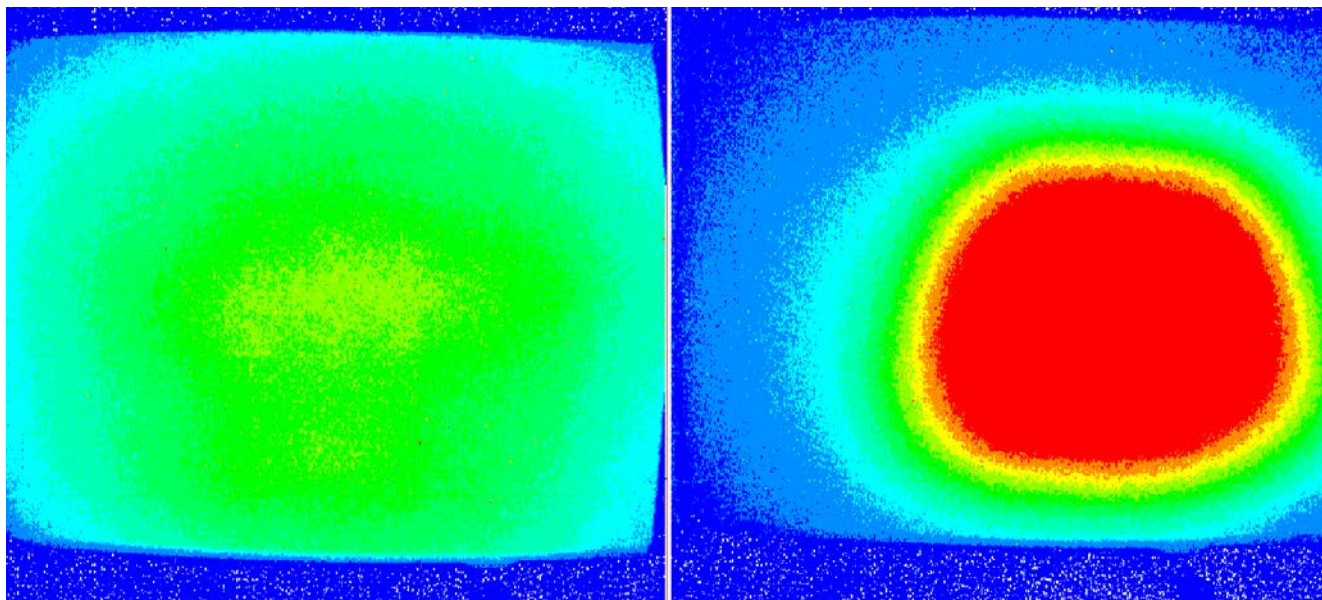


Figure 12: Distribution of the neutrons at the sample position of KOMPASS. The images were acquired when neutrons were extracted for the very first time. The left and right figures show the beam for the non-focusing and doubly focusing configuration of the monochromator, respectively.

APEX at NEPOMUC: Towards the creation of the first magnetically confined laboratory electron-positron plasma

Most research in plasma physics is focused on investigating classical electron-ion plasmas, many characteristics of which arise from the mass imbalance of the species. Altering such a system, by creating a plasma composed of particles with identical mass but opposite charge, is predicted to feature fundamentally different phenomena such as unique stability and wave propagation properties. Such so called “pair plasmas” have therefore been studied theoretically and computationally for decades; however, their experimental demonstration has not been successful to date. The APEX project is aiming for the creation of the first magnetically confined laboratory plasma consisting of electrons and positrons, using the world’s strongest high-flux low-energy positron source NEPOMUC. Achieving a stable confinement of such a system is a challenging endeavor, as there exist no established solutions for many of the key factors which, consequently, need to be derived from scratch. As a first step, we are conducting experiments using a prototype trap, consisting of a supported cylindrical permanent magnet. As positrons guided directly onto it would normally be magnetically mirrored, appropriate external electric fields, inducing a drift motion across closed field lines, are required and generated by a pair of ExB plates. The efficiency of this injection process has recently been demonstrated to reach close to 100 % for the remoderated positron beam at 5 eV and 20 eV kinetic energy. Our most recent results indicate long confinement times in the order of one second, which is equivalent to a hundred thousand toroidal precessions around the magnet. Over the coming year, the trap will be upgraded to the highly symmetrical dipole field of a levitated superconducting coil, which will also allow the simultaneous confinement of electrons and positrons.

Outlook for KOMPASS: Completion envisaged for 2018

KOMPASS, the new polarized cold neutron three-axis spectrometer (TAS) optimized for spherical polarization analysis at the MLZ is undergoing its final construction phase. Last year brought significant progress in assembling the instrument. In particular, the monochromator stage, including the large doubly-focusing monochromator for pyrolytic graphite HOPG(002), the goniometer, the motorized aperture slits, and the pneumatically-controlled lead radiation shielding were completely installed and successfully tested in September 2017. Fig. 12 demonstrates the precise control of the beam focusing as benchmarked by means of a neutron camera. The beam images for the unfocused and focused configuration [5] were obtained when neutrons were extracted for the very first time at KOMPASS. Precise positioning of the samples in the upcoming experiments in early 2018 is provided by the completely assembled sample tower that is equipped with a motorized xy-stage and cradles. Another demanding task completed in 2017 comprises the assembly of the detector tower. It contains a ^3He -counting tube and the detector-electronics surrounded by a multilayered shielding on a movable platform. Fig. 13 shows the most recent view of the KOMPASS spectrometer. We plan to complete the installation of the PILZ safety system, including the yellow security fence and shielding walls around the experimental area, at the beginning of 2018. The forthcoming mounting of guide fields, spin flippers, and the implementation of the NICOS control system promises that KOMPASS will already be available in a half-polarized diffraction configuration during the first reactor-cycles in 2018. Consecutive testing of the instrument in the diffraction configuration will be performed for the commissioning of the installed neutron optical components and the characterization of the momentum resolution of KOMPASS for various focusing and non-focusing configurations via scattering from standard samples in the elastic mode. Presently, the design and manufacture of the compo-



Figure 13: The photo shows the present status of the beamline KOMPASS.

nents for the analyzer tower is in progress. It is expected that the first TAS experiments with full polarization analysis will be able to be performed at KOMPASS at the end of 2018.

Upgrade of SAPHiR in the neutron guide hall east

2017 was devoted to completing the SAPHiR shielding and to further developing the sample environment to increase the maximum pressure. The biological shielding of the SAPHiR neutron guide was simulated by F. Grünauer, followed by the planning and detailed construction by the ZEA-1 group of M. Koenen (Fig. 14). With the manufacture of the shielding, all major components of SAPHiR have been completed and either installed onsite or stored until the final setup is possible. One goal of the ongoing offline operation of SAPHiR is the development of the sample environment and the increase in the available maximum pressure. The currently used anvils

consist of tungsten carbide (WC) whose hardness and maximum load resistance limits the pressure to ca. 15 GPa in samples large enough for neutron measurements. In order to use harder materials such as sintered polycrystalline diamond (PCD), new anvil geometries have been developed that combine PCD pressure tips with other materials. As a first step, an anvil geometry has been constructed in which conic pressure tips of hard material are supported by a WC base (Fig. 15 a-b). However, the load resistance of the geometry is limited by the tensile strength of the WC. Hence, the design has been modified and refined by finite element modelling (Fig. 15 c-d). The final results are currently being tested.

A new 3 Tesla magnet for Small Angle Scattering

The sample environment equipment pool was expanded by the addition of a new 3 T high temperature superconducting magnet with air bores (Fig. 16). Together with the company HTS 110 from New Zealand a new, compact and light-weight magnet for small angle scattering applications was constructed. The magnet works with a closed cycled refrigerator and is optimized for low stray fields. Thus, full polarization analysis is possible even with ^3He polarization cells in close proximity. Thanks to its air bores, the background at room temperature is minimized. Additionally, standard top loading cryostats can be used inside the magnet. This makes the new magnet a very powerful and flexible tool.

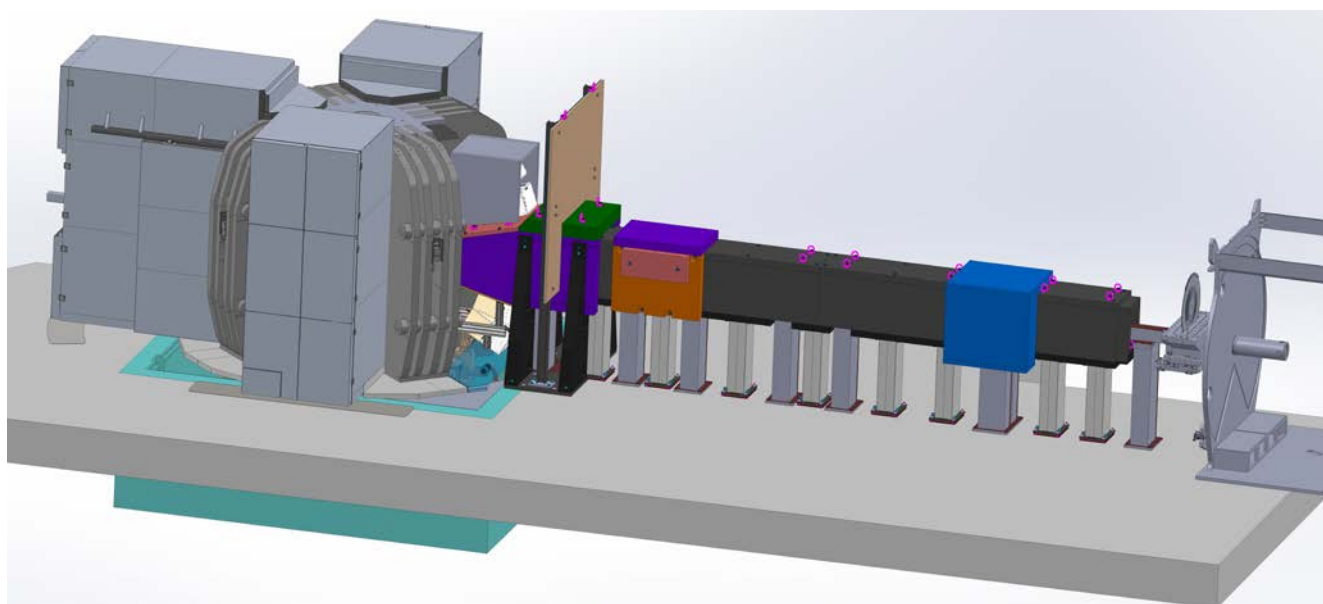


Figure 14: Model of SAPHiR with neutron guide shielding. The double elliptic neutron guide covers the distance from the upstream instrument POWTEX on the right to SAPHiR (left) and has a length of ca. 10 m. The shielding consists of a sandwich construction of steel and Boron – PE.

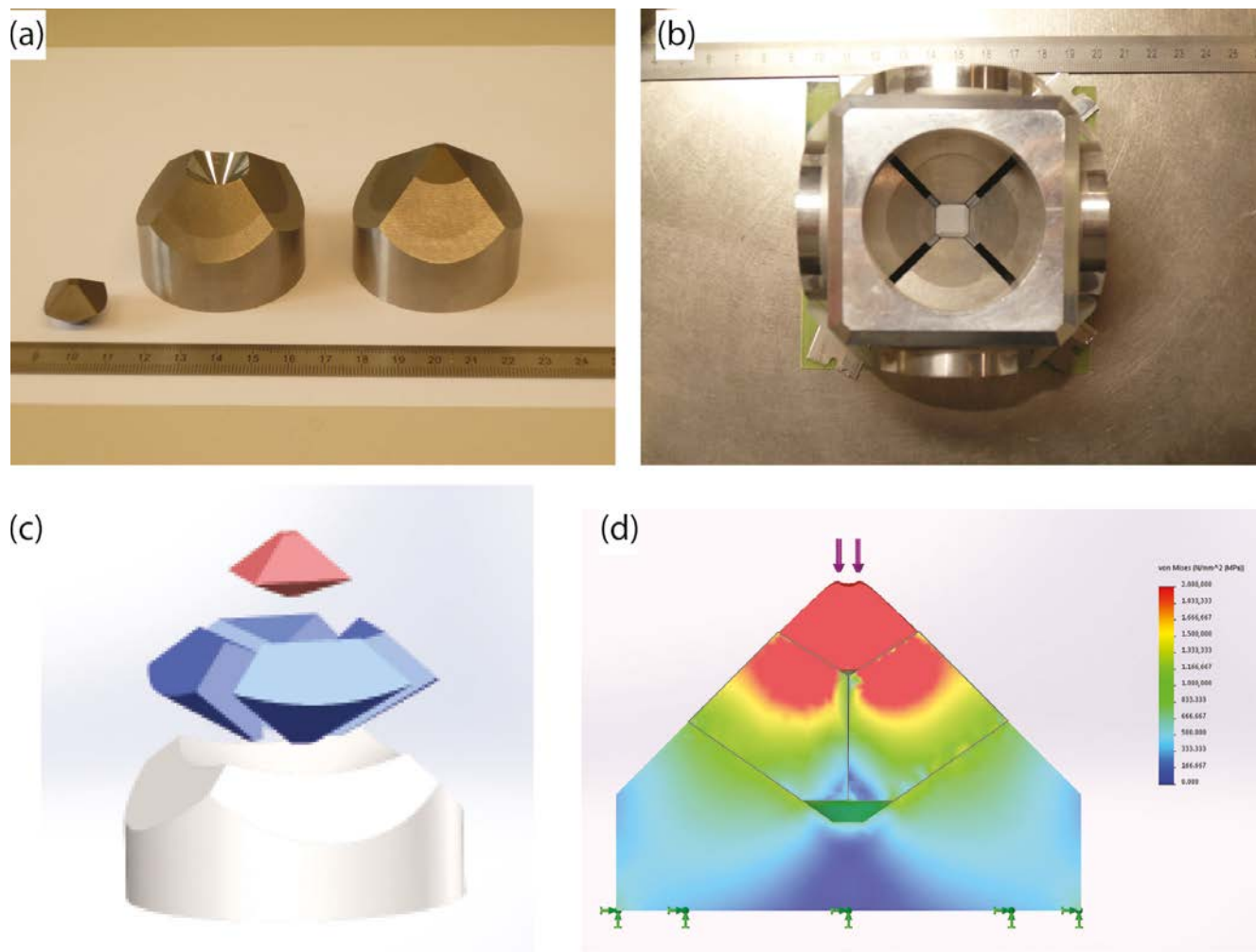


Figure 15: (a) New secondary anvils for small samples; pressure tips of highly sintered tungsten carbide or polycrystalline diamond are supported by solid tungsten carbide bases. (b) A stack of secondary anvils surrounding the sample is placed in the press. Neutrons enter and exit the sample through the anvil gaps. (c) Model of improved design with a sintered diamond pressure tip (red), sectioned tungsten carbide (blue), and a hardened steel base (grey, 60 mm diameter). (d) Finite element modelling with a simulated force of 1 MN (100 tons) to determine the contact angles between the different components.

[1] A. Radulescu et al., *Nucl. Instr. Meth. A* 689 1 (2012)
 [2] A. Radulescu et al., *J. Appl. Cryst.* 48 1849 (2015)
 [3] T. Gigl et al., *New Journal of Physics* 19 123007 (2017)
 [4] I. Mochizuki et al., *Phys. Chem. Chem. Phys.* 18 7085 (2016)
 [5] A.C. Komarek et al., *Nucl. Instr. Meth. A* 647 63–72 (2011)



Figure 16: The new 3 T horizontal SANS magnet.

When the instruments operate smoothly ...

R. Bruchhaus¹, R. Georgii², G. Kemmerling³, J. Krüger², J. Wuttke¹, K. Zeitelhack²

¹Jülich Centre for Neutron Science (JCNS) at MLZ, Forschungszentrum Jülich GmbH, Garching, Germany; ²Heinz Maier-Leibnitz Zentrum (MLZ), Technical University of Munich, Garching, Germany; ³Jülich Centre for Neutron Science (JCNS), Forschungszentrum Jülich GmbH, Jülich, Germany

The project groups at the MLZ coordinate activities in the areas of instrument development, the commissioning of tasks, and technical service. They act as the interface between the instrument scientists, technical support groups or companies, and management.

Detector Group

The CHARM Project – Prototype of a curved ³Helium based Multi-Wire Proportional Chamber

The new high intensity powder diffractometer ERWIN at the MLZ and the existing cold powder diffractometer DMC at the Paul Scherrer Institut (PSI), Switzerland, will be equipped with two new large area 130° curved 2-dimensional position sensitive ³He-based Multi-Wire Proportional Chambers (MWPC). The design of the detectors, which will be built in close collaboration between the MLZ and PSI, has been adopted from the curved MWPCs designed and built by the Brookhaven National Laboratory's detector group for ANSTO and LANSCE. However, an individual channel readout with a center-of-gravity algorithm based on the Time-over-Threshold method is applied to precisely determine the neutron impact position. As a proof of principle, a small size prototype detector covering 29.4° horizontal acceptance has been designed and built by the MLZ detector group in collaboration with the PSI and the Institute Laue-Langevin (ILL), France. It will serve to demonstrate the feasibility of building a large area detector and to evaluate its performance. While the prototype has a fully modular design consisting of two individual MWPC segments, each covering 14.7° angular acceptance, mounted seamlessly inside a common pressure vessel, the full-size device will contain nine MWPC seg-

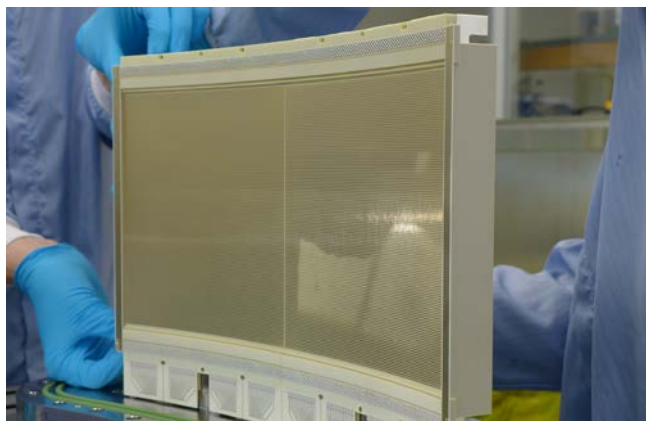


Figure 1: Mounting of the two individual MWPC segments inside the prototype's pressure vessel.

ments. Fig. 1 shows a photograph of the interior of the prototype with the two MWPC segments during the mounting of the device in the cleanroom of the detector lab. Each MWPC segment consists of a bent printed circuit board (radius $R = 800$ mm) with 128 horizontal cathode strips and 128 vertically stretched anode and cathode wires with 1.6 mm strip/wire pitch, respectively. Each cathode strip and wire is read out individually, thus providing a position resolution (FWHM) ≤ 1.6 mm in both directions. The 16-mm deep neutron conversion region is formed by a metalized Polyimide foil directly glued to the thin entrance window of the pressure vessel, resulting in a detection efficiency $\epsilon = 75$ % for thermal neutrons. The fully modular architecture of the front-end readout and signal processing electronics should make it possible to operate each segment with a global count rate of 200 kHz at 10 % dead time.

In autumn 2017, the prototype underwent first measurements at the TREFF beam line at the MLZ, revealing that the envisaged position resolution, in combination with an extremely low differential nonlinearity, can be achieved. Fig. 2 shows a photograph of the device, including its online gas purification system mounted on the detector test bench at TREFF. Further tests of the device, including the newly designed FE-electronics, are planned for early 2018.

Scientific Computing

Contributing to the ESS

For the next three years, the Scientific Computing Group of the MLZ will be reinforced by two colleagues working for the ESS, as part of the German in-kind contribution. They will enhance data analysis software that will be needed by some of the first ESS instruments. While some of their efforts will address the specific data structure of pulsed-source instruments, they will also work on core algorithms and user interfaces that are equally useful for the steady-flux instruments of the MLZ. Conversely, they can validate their code before ESS is commissioned by using real data from the operating instruments of the MLZ, and they can learn from contact with experienced instrument scientists. This cooperation will, therefore, be beneficial for both parties.

From grazing incidence to generic reflectometry

BornAgain, software designed to simulate and fit small-angle scattering under grazing incidence (GISAS), is the largest project the Scientific Computing Group has undertaken so far. BornAgain offers unprecedented functionality and flexibility. Beginners find it convenient to build sample models via a graphical user interface; advanced users can define fit models and parameter constraints programmatically in Python. These qualities have been recognized internationally, and therefore the software work package of SINE2020 stipulates that BornAgain is to become the sole institutionally supported software not only for GISAS, but also for off-specular scattering and specular reflectometry. This will also improve the quality of GISAS analyses, since detector images always contain specular reflections besides the two-dimensional GISAS pattern. In June 2017, the BornAgain team organized a workshop on reflectometry software as part of the SINE2020 software meeting, and gathered input from reflectometry practitioners and software developers. It clearly emerged that the ever-changing needs of instrument users require an extremely versatile, highly configurable analysis software. BornAgain is well on the way to meeting this demand. The remainder of 2017 was for the most part spent on foundational work: the central data structures and algorithms of BornAgain had to be generalized to prepare for full support of reflectometry and off-specular scattering. In summer 2018, this new functionality will be ready for testing by early adopters.

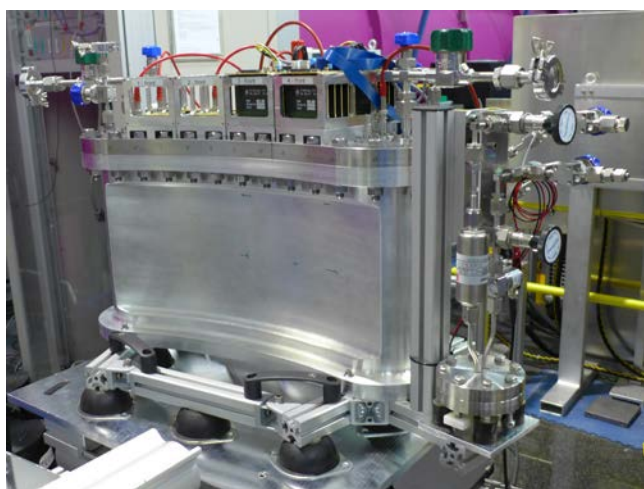


Figure 2: The CHARM prototype detector mounted at the detector test bench at TREFF

Data analysis for single crystal diffraction

Work on the single-crystal diffraction software NSXTool continued in close collaboration with the ILL. The two developers are in almost daily contact, and visit each other for a full week every few months. The quality of peak integration is now on a par with the best closed-source programs. Validation against real data from BioDiff continues. It is expected that NSXTool will go into routine operation in 2018.

Data reduction

Work continues on data reduction software for several instruments. The reduction software STeCa2 for STRESS-SPEC has been further improved in close cooperation with those responsible for the instrument. STeCa2 is now also used at neutron and x-ray instruments in Berlin, Geesthacht, and Harbin (China). At TOFTOF, Mantid with an instrument-specific GUI is in routine operation. At DNS, Mantid support for the diffraction mode is in the commissioning phase; first time-of-flight tests have shown that the workflow established for TOFTOF is also suitable for DNS. Further work will be needed when the position-sensitive detectors go into operation. To prepare for the commissioning of POWTEX, detector tests have been performed at the SNS; the SNS powder diffraction reduction algorithm will be complemented by a couple of instrument-specific routines of our own. Next on our Mantid agenda is support for SPHERES and for SANS-1.

MLZ project groups and JCNS instrument control group

In Jülich, the JCNS instrument control group is operating in close cooperation to improve the instruments through new options using modern hardware and software solutions. Special care is taken to implement standard solutions to support fast and easy maintenance and provide a unified interface to ease the operation of the instruments by the scientific users.

Electronics for detector and motion of TREFF

New electronics have been developed for the detector at the instrument TREFF and successfully integrated into the instrument control and data acquisition system. A major upgrade was carried out for the motion electronics of TREFF. The electronics for 6 additional motion axes for the future new monochromator have been implemented and the outdated electronics for 16 existing axes replaced by new electronics, according to the MLZ standards.

Migrating instruments to NICOS and Tango

Due to the continuing effort of migrating instruments to the unified MLZ instrument control software NICOS, KWS-2 and KWS-3 as well as TREFF are now operating under NICOS and Tango for hardware access. This means that all KWS instruments are now consistent in using the same interface for the definition and execution of a series of standard measurements, which facilitates the process of switching between these instruments for users.

The upgraded neutron spin echo spectrometer J-NSE has been almost completely migrated to Tango, while NICOS is, so far, in use in a supplementary fashion for instrument monitoring. Neutron Depth Profiling (NDP) is a method which is very useful in research fields related to energy, and more specifically in Li-ion battery research. The spectrometer setup is very flexible and can be used at the neutron beams of the test beamline TREFF and the reflectometer MARIA. Now, the spectrometer operates under NICOS and Tango, which makes its use by the scientists much more agreeable.

For the wavelength shifting fiber detector of the instrument SAPHiR, a Tango server has been implemented that facilitates the integration into NICOS.

Extended chopper measurements at KWS-2

At the small angle scattering diffractometer KWS-2, the range of measurement options using the choppers and time-of-flight mode data acquisition has been considerably extended. Real-time measurements can now be extended from hours to days. For measurements with periodic changes of the sample, such as oscillatory shearing, the chopper rotation can now be synchronized to a multiple or divider of that frequency. Finally, for very specialized requirements the event mode data stream can be analysed and histogrammed in different ways using a new tool, with the possibility of reacting to multiple triggers from external sources.

The next generation of the small PLCs offered by the company Beckhoff integrated in sample environment „Tango boxes“ has been tested and introduced for new projects. This will allow code and techniques to be shared with larger PLC projects using Beckhoff parts, which is also the vendor selected for these tasks by the European Spallation Source (ESS).

Control and automation systems

A motorized filter changer was installed at the single crystal diffractometer on the hot neutron source HEiDi. This beautiful piece of equipment was designed and built by the Central Institute of Engineering ZEA-1 of the Forschungszentrum Jülich. Meanwhile, the filter changer was incorporated into

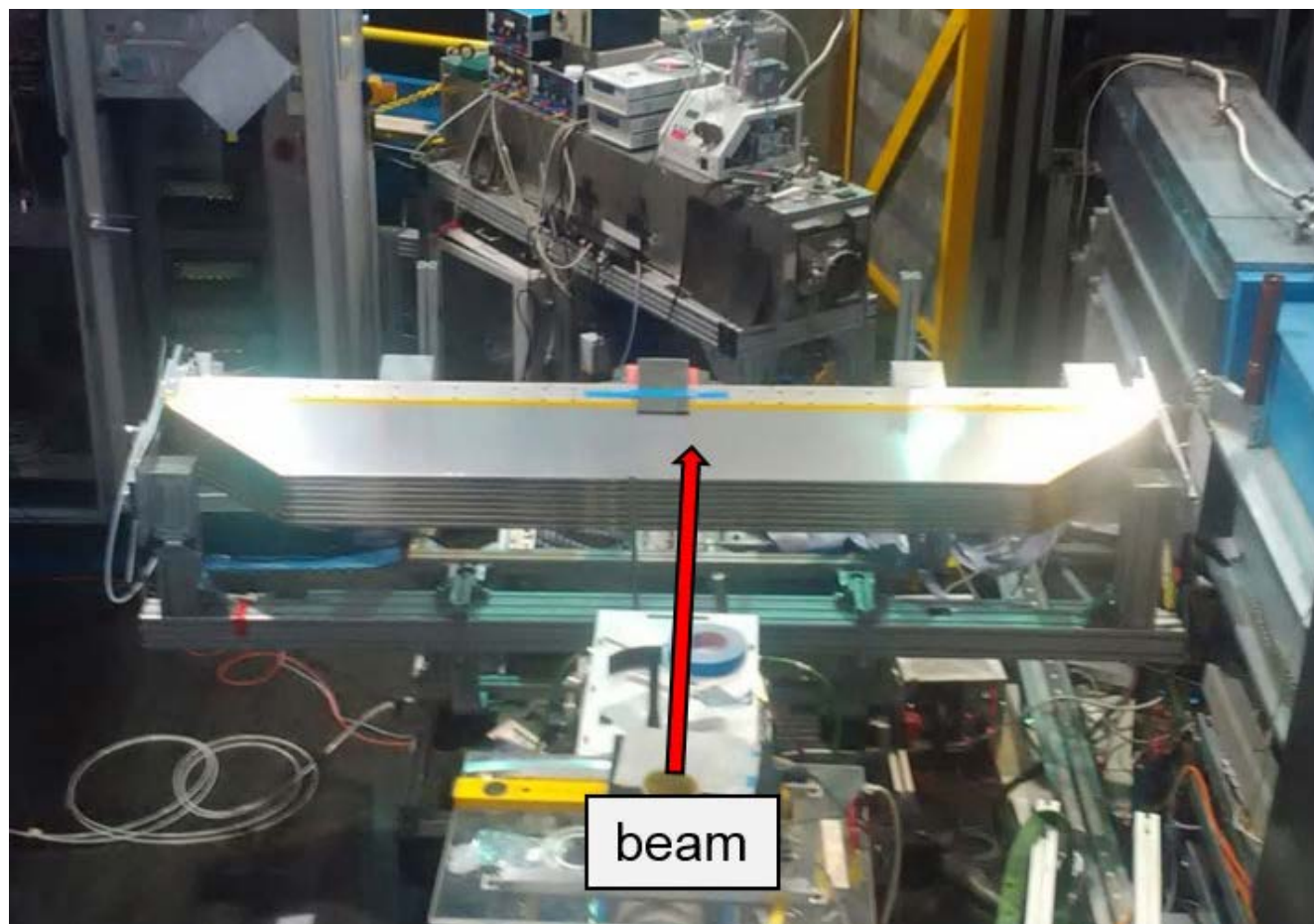


Figure 3: Placement of the Jalousie mounting unit at TREFF. The mounting unit with 8 detector segments in the middle part of the picture was installed on a frame with an angle of 10° with respect to the neutron beam. The neutron beam came from the lower part of the picture and hit almost in the middle of the detector segments.

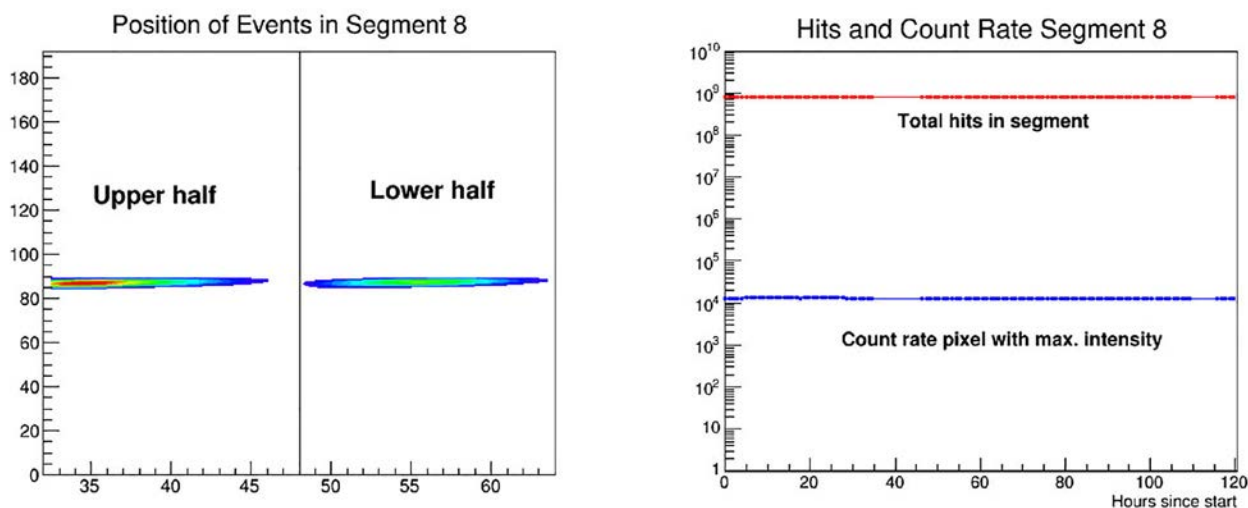


Figure 4: Left: Position of events in the upper and lower half of segment 8. The vertical axis represents the cathode strip number, the horizontal axis shows the readout channel of the anodes in the data acquisition. There are 16 anode channels in each half of the segment. Right: The lower part shows the count rate of the pixel with maximum intensity during the test duration in segment 8, the upper part the sum of its hits.

the motion control network of the instrument and the instrument control software. As for a new aperture, the motion control system was extended by 4 additional axes.

To facilitate control of the sample table, the PLC-based motion control system of POLI was extended by additional axes. The instrument MARIA was equipped with an argon-filled cabinet surrounding the detector and the ³He analyzer chamber. A fully automated system was implemented for this cabinet which is responsible for filling with air or argon as well as the control of the argon concentration. Control of an additional aperture at the entrance of the chamber was also implemented.

Detector group at JCNS

Stability and radiation test with a POWTEX Jalousie detector

The instrument POWTEX envisaged for the east hall is the first instrument that will use the new Jalousie detector type from the company CDT. These detectors are based on modular detector segments with inclined Boron coated layers for neutron capture, which are placed inside two multiwire proportional chambers per segment for detection of the secondary reaction products. The geometry and depth of the segments were chosen such that neutrons pass up to 8 Boron layers at 10° incidence angle, giving a detection efficiency of 55 % at 1 Å. For the barrel part of POWTEX, there are always 8 detector segments grouped together to form a mounting unit for later installation, and meanwhile all mounting units are produced and initially tested by CDT.

At the instrument TREFF, such a mounting unit has been taken to study the functionality of the detectors in the case of long-term neutron irradiation via a suitable short-term measurement. A section of the detectors was irradiated by the neutron beam to receive an accumulated dose under operating conditions, which corresponds to use in the region of at least 10 years at the instrument POWTEX. Under the

“worst-case” assumption that later, at POWTEX, a pixel within a 5 ms pulse sees all the reflexes rushing over the detector, i.e. collecting 100 % of the scattered intensity along the time axis, the neutron dose over an operating period of 10 years at POWTEX should add up to 3×10^8 neutrons/cm². In order to reach this neutron dose, the detector would have to have been continuously operated in the neutron beam, where the intensity had been adjusted to about 60 kHz/cm² to avoid overstress damage (e.g. too high detector currents).

The experimental arrangement of the test is shown in Fig. 3. Due to the limited size of the beam spot, the majority of neutron hits was located in the uppermost segment of the mounting unit. The detector was continuously irradiated over 120 hours and the beam intensity, ambient pressure and hall temperature were monitored. Measurements of 30 minutes duration were periodically taken with the detector during the test. The results for the uppermost segment are shown in Fig. 4.

The left side of the Fig. 4 shows the reconstructed beam spot in the upper and lower half of the segment. Due to the 10° angle of inclination, the passage point of the beam is shifted from the upper to the lower half to higher anode channels. On the right side of the Fig. 4, the number of total hits in the segment and the count rate of the pixel with maximum intensity are plotted for the duration of the test. The total accumulated neutron dose of the pixel with maximum intensity was calculated to be about 2.6×10^{10} neutrons/cm², which exceeds the 10 year operation dose by almost a factor 100. As can be seen in the Fig. 4 on the right, the detector showed very stable operation over the test duration with fluctuations of the total hits and the count rate of the pixel with a maximum intensity of below 2 %. This means that there is apparently no degradation in the beam spot position nor the whole segment and it indicates that the detector should be capable of operating properly during long-term neutron irradiation at POWTEX.

Support for MLZ from Jülich: Engineering and detectors

J. Daemen¹, R. Hanslik¹, H. Kämmerling¹, C. Tiemann¹, D. Durini², M. Herzkamp², R. Bruchhaus³

¹Central Institute for Engineering, Electronics and Analytics, Engineering and Technology (ZEA-1), Forschungszentrum Jülich GmbH, Jülich, Germany; ²Central Institute for Engineering, Electronics and Analytics, Electronic Systems (ZEA-2), Forschungszentrum Jülich GmbH, Jülich, Germany; ³Jülich Centre for Neutron Science (JCNS) at MLZ, Forschungszentrum Jülich GmbH, Garching, Germany

Experts from the Central Institute for Engineering, Electronics and Analytics (ZEA) based at the Forschungszentrum Jülich provide considerable manpower and expertise to support and drive neutron scattering instrument improvement and operation at the MLZ. In 2017, a key project was the installation of the superconducting coils for the neutron spin-echo spectrometer J-NSE. The high-throughput time-of-flight neutron diffractometer POWTEX successfully underwent the transition from the drawing board of the design engineers and structural designers into manufactured masterpieces of shaped materials and metal. The installation to test the impressive parts began in Jülich. The mechanics to install the 288 detector tubes into the vacuum chamber of TOPAS was fabricated and tested. A device to provide an Ar atmosphere in the neutron flight path of the reflectometer MARIA was manufactured and is now in operation at the MLZ. Installation work and commissioning of the equipment constructed and built by ZEA in Jülich can only be completed with help and strong support from the JCNS technical staff on-site in Garching. In order to improve on the neutron count rates currently achievable, gain greater mechanical flexibility, operate in magnetic fields of up to several Tesla, and increase the detector space resolution in small angle neutron scattering (SANS) instruments such as KWS-1 or KWS-3 of the MLZ, a new generation of pixelated scintillator detectors could be the way forward. An interesting candidate for the photodetector element in these neutron detectors could be an array of silicon photomultipliers (SiPM), either analog or digital. Several test setups using SiPM were built and, among other parameters, the spatial resolution tested. The results are very promising and a spatial resolution better than 1 mm might be possible.

A considerable workforce to support and drive neutron scattering instrument improvement and operation at the MLZ is located at the Forschungszentrum Jülich, in Jülich. The Central Institute for Engineering, Electronics and Analytics, Engineering and Technology (ZEA-1) includes groups of expert engineers engaged in design and construction. In addition, it operates workshops in which parts ranging in size from tiny μm up to heavy weights of several tons can be precisely machined, handled and assembled. The Central Institute for Engineering, Electronics and Analytics, Electronic Systems

(ZEA-2) is active in preparing customized detector solutions for the neutron scattering instrument suite at the MLZ. These groups of skillful experts and the large scale infrastructure are key players in enhancing the performance of the neutron scattering instrument to meet the requirements that arise out of the challenges in the various scientific fields. These teams work hand in hand and are strongly supported by the JCNS technicians and engineers based at the MLZ in Garching.

ZEA-1: New superconducting coils for J-NSE

Careful analysis of the performance of the spin-echo spectrometer J-NSE lead to the conclusion that new superconducting coils with better magnetic field homogeneity and strength would lead to a considerable improvement. The magnetic field of the new main coils is 1.8 T, i.e. 4x stronger than the old conventional coils. However, the new coils come with much larger outer dimensions. Thus, a complete reconstruction of the mechanics around the sample table was needed. New X-Y-adjustment devices for the correction coils make it possible to adjust and position the correction coils with a precision better than 0.045 mm radially along the beam axis. The newly designed coil around the sample table can now compensate for differences in length which appear due to the movement of the carrier arm. Fig. 1 gives an overview of the “new” J-NSE.



Figure 1: New super-conducting main coils at J-NSE.

As the coils operate at a temperature of less than 6 K, the complete media supply infrastructure had to be rebuilt. Water cooled compressors provide He for cooling. In addition, modern high-performance computer controlled power supplies with considerably better precision were installed and now feed the current to the coils. Fig. 2 shows the control cabinet with the numerous plug-in units. As a result, the reliability of the set-up has improved significantly. Meanwhile, the commissioning of the instrument has been completed and J-NSE has returned to user operation.

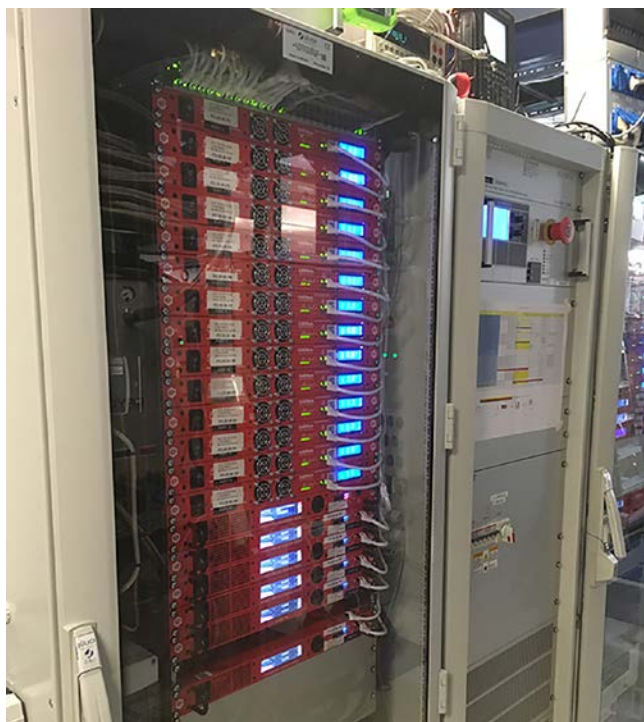


Figure 2: The control cabinet with the series of new high-precision power supplies to power the numerous coils of J-NSE.

ZEA-1: Detector system for the time-of-flight spectrometer TOPAS

The impressive vacuum chamber of the new time-of-flight spectrometer TOPAS, which weighs some 30 tons, has already been installed in the new guide hall at the MLZ in Garching. Testing of the vacuum system has been successfully completed. The next important step is the installation of the detector system. The detectors will cover the wall of the chamber completely, providing a huge solid angle of 180° for the scattered neutrons. The detector system consists of 288 He^3 filled stainless steel detector tubes with a diameter of 1 inch and an active length of 2050 mm. The flight path of the neutrons from the sample to the detector tubes is 2500 mm.



Figure 3: 16 detectors are mounted on a detector box.

Careful analysis of the mechanics was needed to come up with a design for the detector system which fulfills the requirements of sufficient stability under different operating conditions such as vacuum and temperature in the chamber, and good access to the tubes for maintenance. As a result, 16 detector tubes form a unit mounted onto a box and a total of 18 boxes subdivided on 6 detector banks form the detector system with a total number of 288 tubes. Fig. 3 - 6 give an overview of the system and the various steps involved in its installation, either in the workshop-hall in Jülich or on-site at the MLZ in Garching.

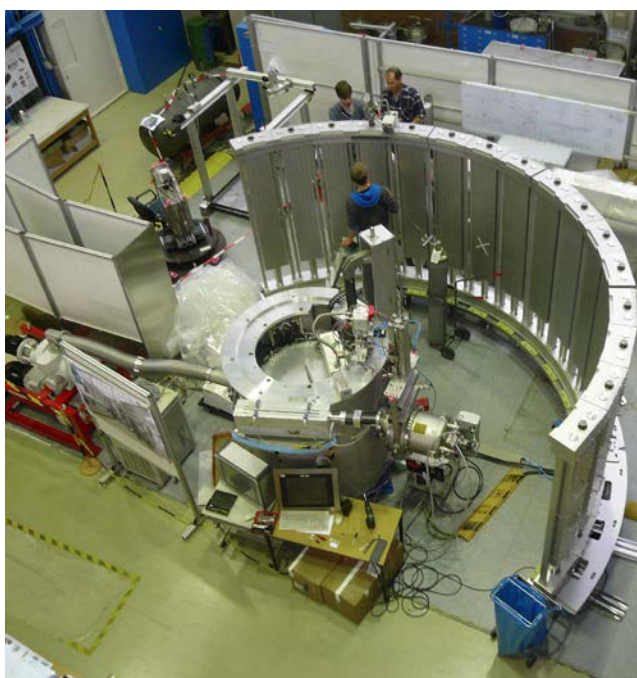


Figure 4: 18 detector boxes are mounted on 6 detector banks in the hall of ZEA-1 in Jülich.



Figure 5: Inside the vacuum chamber the detector bank base plates were mounted and aligned with respect to the the sample center.



Figure 6: Trial installation of a detector box without He³ detector tubes using a specially designed assembly cart.

A rail system at the vacuum chamber ceiling is installed to allow the mounting of the detector boxes at the appropriate position (Fig. 7). Finally, Fig. 8 shows a detector box (for testing without detector tubes) fixed in its final position. In summary, the mechanics, including the vacuum feedthrough for the electrical high voltage supply of the detector tubes, has been manufactured, the different steps to carefully mount the sensitive and very expensive detector tubes to the boxes and banks have been tested and now everything is ready for the installation of the detector system inside the chamber.

ZEA-1: Argon filled cabinet for the reflectometer MARIA

Scattering on the flight path between the sample and detector is a source of background. Providing a controlled atmosphere of Ar in this part of the instrument can improve the performance of the reflectometer considerably. Thus, a sophisticated shielded cabinet was designed and manufactured.

In addition, this box needs to house the Magic Box for neutron polarization analysis which can be moved into and out of the neutron beam. Before the cabinet was transported to



Figure 7: Assembly of the rail system with the carriage. Using this device, the detector boxes can be positioned and mounted inside the vacuum chamber.



Figure 8: The detector box (for testing without tubes) is placed in the final position and mounted on the detector bank with the rail system and carriage.

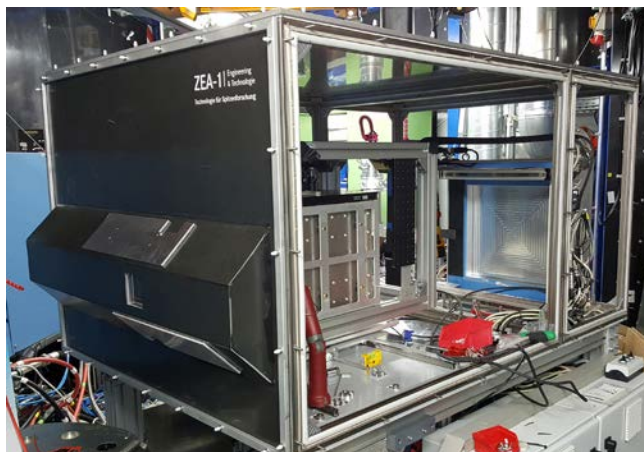


Figure 9: The cabinet during installation at the instrument.



Figure 10: The closed and shielded cabinet in operation.

the MLZ in Garching, extensive leak testing and electromagnetic compatibility (EMC) checks were performed to ensure that the gain afforded by the Ar atmosphere is not counterbalanced by poor electrical performance. The EMC tests showed very good shielding up to a frequency of 7 MHz, which means that no interference can be expected during use. In addition, Ar leak rates of the cabinet were very low, resulting in a very low Ar consumption during operation. Finally, the cabinet was moved to MARIA prior to installation, Fig. 9 and 10. Meanwhile MARIA is back in user operation and the first experiments demonstrated the improvements due to the Ar atmosphere in the flight path and showed that the specified requirements have been fulfilled.

ZEA-1: The high-throughput powder diffractometer POWTEX takes shape

The high-intensity time-of-flight neutron diffractometer POWTEX successfully underwent the transition from the drawing board of the design engineers and structural designers into manufactured masterpieces of shaped materials and metal. Fig. 11 gives an overview of the area in the ZEA-1 workshop where the instrument is assembled for testing.

Fig. 12 shows the test of the impressive wing-shaped doors to open the sample chamber. This operation is required to gain access to the detectors for maintenance. The top part of the sample chamber can be removed completely and slid



Figure 11: POWTEX assembling area at the ZEA-1 workshop.



Figure 12: Test of one detector wing door.

to the side to allow easier access to the chamber from the top (Fig. 13). Now, the part of the detector which is built into the roof of the instrument can be reviewed and maintained quite easily. Powerful motors are used to move the heavy doors of several hundred kilograms which need to be carefully controlled so that the doors move smoothly without causing damage to the very sensitive detector assembly. In 2018 assembly and testing will be continued, after which the whole instrument will be transferred to the place of operation at the MLZ in Garching.



Figure 13: Mounted lifting device for the top detector.

ZEA-2: Development of the Neutron Scintillation Detector using Digital Silicon Photomultipliers

Due to their vulnerability to radiation, silicon photomultipliers (SiPM) have not been used as photodetectors in neutron detection applications until now. However, tests detailed in the annual report 2016 (pp. 58/59) showed that the expected life-time can be more than a decade in e.g. the KWS-1 instrument. Therefore, first attempts were undertaken to develop a detector system using SiPMs as an alternative to Photo Multiplier Tubes, and a demonstrator device was built to show the feasibility of this technology.

We developed four different optical setups on one Philips Digital Photon Counter (DPC3200-22-44, henceforth PDPC) in order to test several configurations. Two designs featured a continuous, polished, 1 mm thick ^6Li -glass scintillator screen, which converts incoming neutrons to light ashes. In one design the scintillator was glued directly on top of the PDPC while, in the other case, a 0.5 mm thick glass plate was placed between the scintillator and photodetector. This optical disperser improves the distribution of light among the pixels, which allows a position reconstruction with better resolution than the pixel pitch of the PDPC (4 mm). Another design featured grooves cut inside the scintillator in order to divide it into pixels as well, with a one to one correspondence between the scintillator pixels and PDPC-pixels. This design is used for the characterization of the detector with regard to linearity and efficiency. Finally there was a pixel design using a four to one correspondence between the scintillator pixels and PDPC pixels. This design was used to test if a resolution of $2 \times 2 \text{ mm}^2$ is reachable. For this to work, the light needs to be distributed among more than one pixel, which is why we placed a disperser glass between the scintillator and PDPC in this design as well.

Several trial measurements were carried out at the KWS-1 in order to test the device and characterize it with respect to linearity, efficiency and position resolution. For the linearity and efficiency, the demonstrator device was placed directly in the neutron beam at varying beam intensities. A 2 min measurement at each intensity setting was compared to a measurement by the Anger-camera currently installed at the KWS-1. We found that the demonstrator device can reach an efficiency of 97(6) % of that of the Anger-camera, which is about 91(6) % total efficiency for neutrons with a wavelength of 5 Å.

To examine the spatial resolution, a 1:5 mm thick lucite screen was placed in a cold neutron beam (5 Å wavelength) in order to scatter neutrons isotropically. The demonstrator was positioned off-beam, 15 cm away from the lucite screen. In this way, the detector area was irradiated almost homogeneously (less than 6 % deviation across the detector surface). A boron carbide mask containing several holes of 4, 2 and 1 mm diameter was placed in front of the scintillator screen. By comparing the reconstructed image with the original mask design, it is possible to give an estimation for the spatial resolution of the detector.

We also simulated the detector design and obtained the spatial distribution of photons across the SiPM surface. Using this information, it is possible to estimate the neutron position of an event by minimizing the difference between the measured and expected photon counts with respect to that estimated for the neutron position.

Fig. 14 shows the spatial distribution of reconstructed neutron events recorded during a 20 min measurement of homogeneous irradiation. Overlaid on this image are green circles, which correspond to mask holes. Most holes have clearly visible peaks with corresponding positions and diameters. In particular, the three small holes close to each other in the lower left quadrant are clearly distinguishable, which suggests that a spatial resolution better than 1 mm might be possible with such a detector.

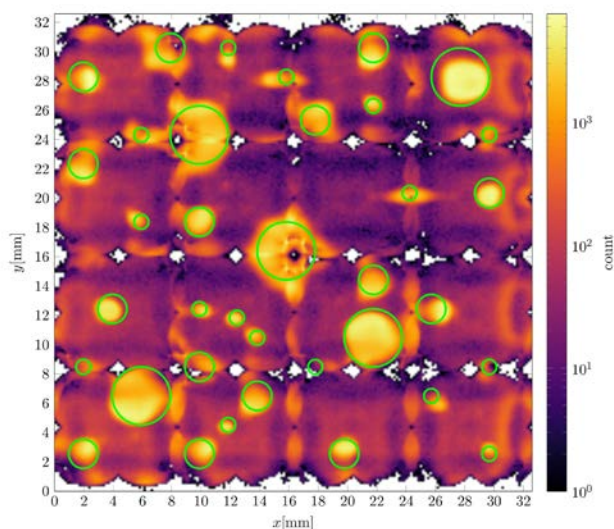


Figure 14: Reconstructed irradiation image of a 20 min measurement behind the diaphragm. The green circles are the diaphragm holes as per design.

Exchanging the plug JMA16 in the beam tube SR6 at FRM II

E. Calzada

Heinz Maier-Leibnitz Zentrum (MLZ), Technical University of Munich, Garching, Germany

The idea of changing a completely inaccessible element weighing 5 tons and with a local dose rate up to 5 Sv/h at its front, and then mounting a new element of 5 tons in a completely inaccessible beam tube with a tolerance of 2 mm was a highly challenging - and at the same time fascinating - task. In December 2017, the exchange of the plug JMA16 in the beam tube SR6 at the FRM II was finally accomplished after 2.5 years of intensive planning, development and training. The exchange of this beam plug was an important step in promoting the commissioning of the ultra-cold neutron source, which will significantly expand the scope of research at FRM II in the future.

The reason for the exchange was not due to any defectiveness of the old plug. The previous plug was a blind one and only had a shielding function, i.e. locking the beam tube completely. Since it was not accessible for measurements prior to the hot phase, the complete planning process for the approval and development of the workflow regarding radiation protection, and waste disposal in particular, was based exclusively on Monte-Carlo simulations.

The exchange of the plug JMA16 consisted of the following four partially self-contained projects:

1. Manufacturing of the new plug with a central channel

The UCN group was solely responsible for the design and manufacture of the new plug, in close cooperation with the FRM II quality control office.

For the new design, the main focus was on the careful selection of materials with low impurities (in particular, the low cobalt content of the materials used), as well as the covering of the part closest to the neutron source with boron rich material in order to reduce the activation of the new plug.

The design and manufacture, along with the complex documentation involved, was meticulously carried out by the engineers of the UCN team supported by the quality control team and monitored by the experts from the approving authority.



Figure 1: Working area in front of the beam tube SR6.

2. Development of special tools

Due to the high dose rate at the front part of the plug, the element was inaccessible.

Thus, a strategic framework had first to be mapped out for this task. Then, a range of new tools and special equipment had to be developed for the remote manipulation of the plug located on the beam tube SR6.

There were three main components: a bottle to shield the plug nose, a transportation frame, and a lifting system were fabricated and tested. In addition, a dummy plug with exactly the same dimensions, weight and center of gravity location as the original plug was manufactured for training purposes. Special machines such as the so-called 'Strahlrohr-nase-Wechselmaschine' (SRWM) were put into operation. With the SRWM, heavy and potentially hot components within or near the biological shielding of the FRM II can be replaced. In addition, a two-winged shielding door was used. Both were remote-controlled and monitored by eight cameras.

The equipment in its entirety was first assembled in another sector in order to practice each movement and optimize the strategy to the maximum. This strategy consisted of a series of individual procedures that were to be followed meticulously to guarantee that no step was forgotten. At the same time, this strategy had the potential to free the mind to react flexibly and adequately in the event of unexpected issues.

The final step of the optimization was carried out under the critical eye of the approving authority and their consulting experts.

3. Establishing the working area

The space near the beam tube SR6 in the experimental hall is occupied by the permanent set-up of the instrument TRiSP. In order to gain sufficient working area, as a first step after the reactor had been shut down all the shielding elements placed in front of the beam tube SR6 had to be disassembled in order to make it accessible.

Enough space had to be gained for the placement of the 8-ton shielding gate in front of the beam tube SR6 which functioned as a shield against the radiation coming from the reactor while the plug was being removed.

That is why several tons of shielding also had to be removed from the neighboring TRiSP and PUMA instruments (Fig. 1).

4. Changing the plug

Once the necessary space had been cleared, all the remote handling tools for the plug were transported in front of the beam tube 6 (SR6) and were fully assembled and adjusted there.

When the set-up for the work in the experimental hall was complete, the technical and organizational radiation protection measures were implemented.

Meanwhile, the necessary authorization for handling radioactive waste was granted by the Federal Office for Radiation Protection, as well as the approval by the consulting expert from the approving authority for implementing the measures. The working team was all set to change the plug between 15th and 17th November 2017. For this most critical period, the team consisted of a small and well-trained crew of only 4 operators assisted and overseen by 2 radiation protection colleagues. Although each operator was assigned to a specific job, it was part of the safety framework that each operator was also able to take over each of the tasks.

Due to the radiation, nobody was allowed to stay near the device during and immediately after removal of the plug until the plug nose had been radiologically shielded and the local dose rate reduced to an acceptable value of 50 $\mu\text{Sv/h}$. The period of time when the beam plug is outside the beam tube without shielding is called the 'hot phase'.

Therefore, the team operating the SRWM had to stand behind a protective shielding wall during the entire procedure – and as a consequence, without direct view of the equipment, tools or beam plug. In order to still being able to determine the exact position of the SRWM at any given time, the technicians installed a total of eight cameras at strategic points and marked every significant set position exactly. The video



Figure 2: Handling tools remotely behind the shielding wall.

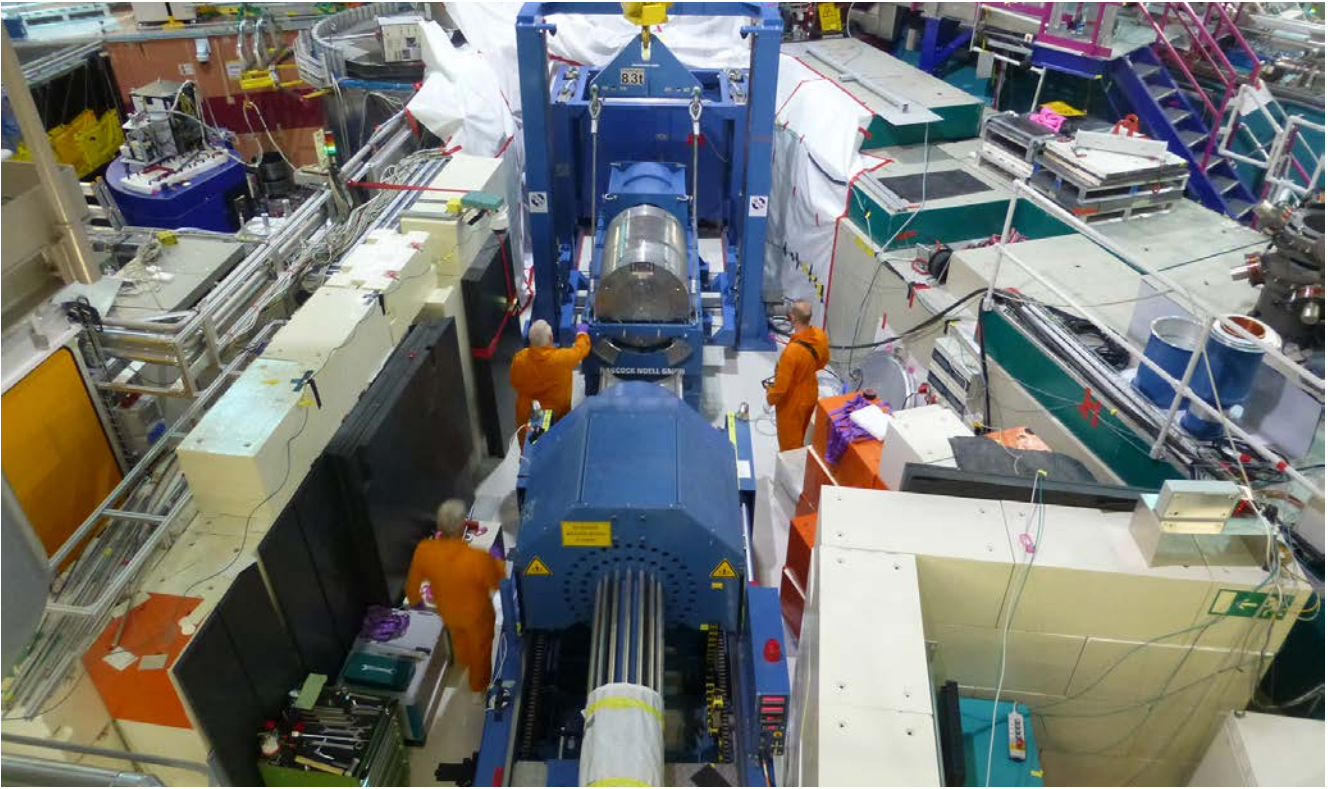


Figure 3: The original plug JMA16 after its removal from the beam tube SR6 with the shielded most active frontal part, and fastened prior to being lifted by the crane.

was transmitted in real time to several screens so that the operators were able to drive the SRWM, the lifting system, the shielding gate and the hall-crane accurately via remote control (Fig. 2).

Initially, the transport system with the shielding bottle was located high above the SRWM transit point and in front of the open shielding gate. The SRWM machine was placed directly in front of the beam tube attached to the plug.

As soon as the last connecting component between the plug and the beam tube had been removed, everyone had to retire to the security area.

Once the original plug had been carefully drawn from the beam tube SR6 and placed onto the SRWM, the shielding door was closed to reduce radiation from the reactor.

Then, the SRWM was pulled back a little further to allow the lifting system to deposit the steel structure containing the shielding bottle carefully and precisely. This redundant system had a special mechanism that would have been able to deposit its load even in the unlikely event of a hall crane malfunction.

Once the system with the shielding bottle was in the correct position, the SRWM inched forward, engaged the system and smoothly pushed the radioactive plug until its nose was fully shielded. This bottle was specially designed for the task and optimized for final waste disposal.

The radiation protection technicians approached the shielded plug carefully using dosimeters and telescopic measurement devices to check that the local dose rate had reduced to an acceptable value of 50 $\mu\text{Sv/h}$.

When they had confirmed that the working area was accessible, the plug was able to be locked in the shielding bottle and attached to the transport frame (Fig. 3).

The next step was to transport the plug with its shield and special transport frame to a suitable container with the help of the hall crane. In this container, material samples required for the documentation were extracted. At the same time, the opportunity was taken for an inspection of the beam tube SR6 using remote-controlled cameras.

One day later the new plug JMA16 was carefully positioned and adjusted on the SRWM.

The space between the largest diameter of the plug and the diameter of the beam tube SR6 was only 4 mm in total, so that even a small skew discrepancy would have caused a significant problem (Fig. 4). Fortunately, the team was able to assemble the new plug at the first attempt and without any difficulty.

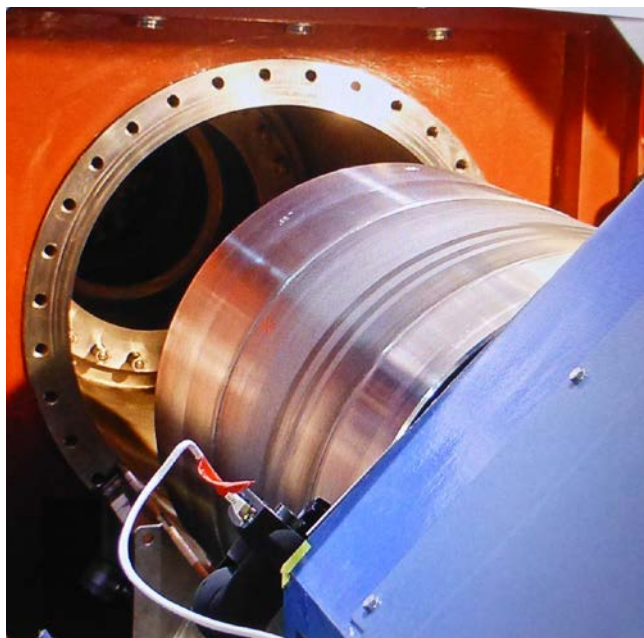


Figure 4: The new plug JMA16 at the very moment of being mounted on the beam tube SR6. A dose rate of 250 mSv/h was measured directly in front of the open beam tube.

After this hot phase, the new plug was carefully adjusted to its final position, monitored by the person responsible from the FRM II quality control team.

With the assembly of the beam tube cover and the leakage helium test both controlled by the approving authority, the work was completed on December 16, 2017.

Conclusion

Pursuing a zero-error strategy with strict adherence to a task list, which had been meticulously drawn up and optimized during numerous cold runs, was the basis for the success of this highly demanding project:

The efficiency of this strategy is reflected in the actual, as compared to the estimated, radiation dose:

The maximum estimated individual dose was 189 μSv . The actual measured individual dose was only 30 μSv .

The maximum estimated collective dose was 826 μSv . The actual measured collective dose was only 150 μSv .

No accidents occurred.

No contamination was detected in the experimental hall.

All the remote-handling tools developed worked precisely and reliably.

No less important was the team spirit of the crew who was eager to face new challenges, to contribute and exchange ideas in frank and open discussions.



Figure 5: The new plug JMA16 is finally fixed on the beam tube SR6.

Working on the mock-up of the molybdenum-99 production facility.



Reactor & Industry

Operation of the research reactor FRM II

A. Kastenmüller

Forschungs-Neutronenquelle Heinz Maier-Leibnitz (FRM II), Technical University of Munich, Garching, Germany

For 2017, 180 operating days were incorporated into the reactor operation schedule issued on 1 September, 2016. This made allowance for, inter alia, the exchange of the shielding plug of the through-going beam tube SR6 on the side of the beam tube oriented to the experimental hall, which the science division has planned for autumn/winter 2017. The newly inserted plug has a slot destined for the installation of the future UCN source. After extensive preparations i.a. transportation of the previous plug for external conditioning prior to disposal, the actual change of the plug took place in mid-November 2017 (p. 66).

Cooling system for the ^{99}Mo facility

Parallel to this, the first parts of the cooling circuit for the future production facility for the medically used radioisotope ^{99}Mo were installed in the reactor pool and further extensive maintenance and testing work was carried out in order to make optimal use of the longer maintenance break. So, the reactor staff used the maintenance break to transfer about half of the heavy water moderator into suitable drums so that it could be transported for reprocessing and the removal of the tritium accumulated in the meanwhile.

Reactor cycles

In the course of 2017, the reactor was operated in the cycles 41, 42 and 43 for a total of 177.4 days and thus achieved an excellent availability of 98.5% compared to the 180 days of operation promised to our users and customers in the latest operations schedule.

Cycle 41 started on schedule on 23 January, 2017. Due to a failure of the computer gateway between the digital reactor protection system and the PLC system used for the operation and control of the reactor, an unplanned scram occurred on 16 March, 2017. After clarifying the cause and replacing the gateway computer, the reactor was restarted on 18 March, 2017. The shutdown at the end of the cycle took place on 25 March, 2017.

Cycle 42 also started according to schedule on 2 May, 2017 and was interrupted once by a scram on 21 June, 2017 due to a failure of a control module in a chiller of the cold neutron source. The restart took place on 23 June, 2017, the lost operating time due to the interruption being appended at the end of the cycle. The cycle therefore ended on 3 July, 2017.

Cycle 43 started on 7 August, 2017 as planned. There were no planned or unplanned outages during the cycle and the shutdown took place on 6 October, 2017.

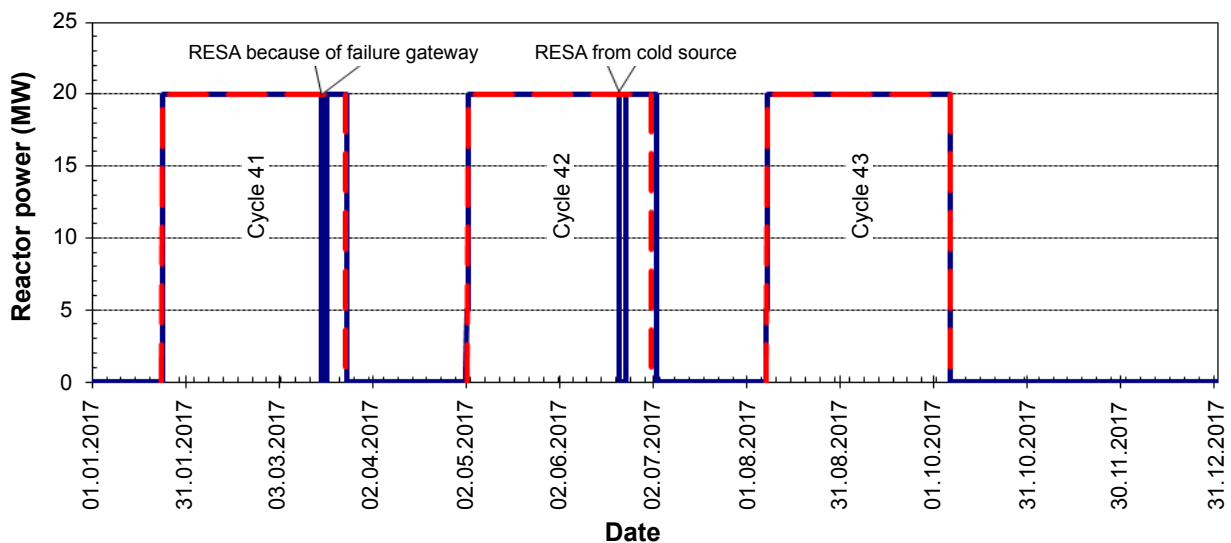


Figure 1: Operation of the FRM II in 2017.

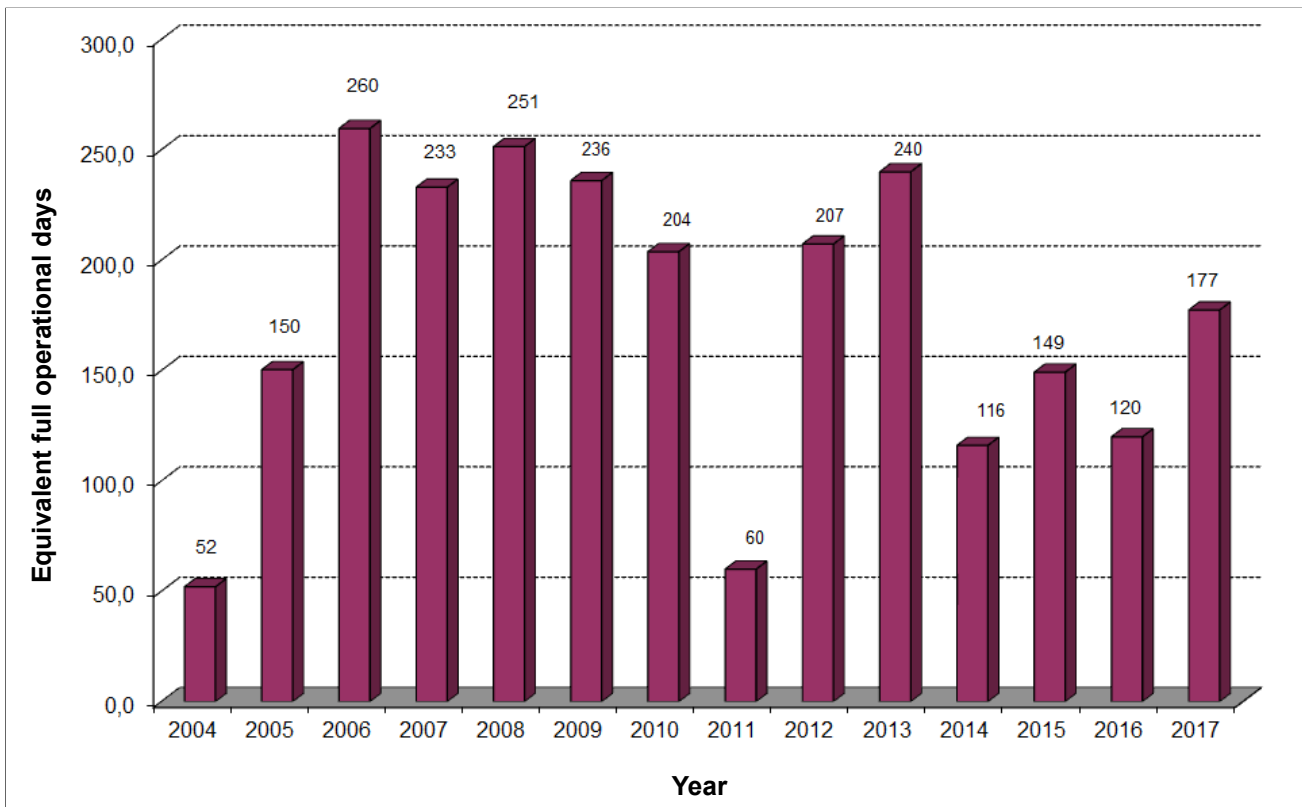


Figure 2: Number of equivalent full power days per year since the start of nuclear operation.

Fig. 1 shows the operating diagram for 2017. Fig. 2 shows the operating statistics since the start of nuclear operation at the FRM II.

A total of 1815 in-service inspections, regulatory inspections by the TSO of the regulatory body covering 18 different topics, maintenance and service works and a total of 34 modifications to improve the facility, guaranteed that the high safety standard of the FRM II was sustained, and even enhanced.

Disposal of spent fuel elements

The FRM II had been in operation for 43 cycles by the end of 2017. As the reactor uses only one very compact single fuel element per cycle, there are 43 spent fuel elements to be disposed of to date. To transport these fuel elements to an interim storage facility and store them there until their final disposal, a special cask is needed. The development, licensing and manufacturing of this cask is well under way. Also, the equipment necessary to handle the cask at the FRM II and the truck to transport it to the interim storage facility are in preparation. The license extension of the interim storage facility for the FRM II spent fuel elements has also been applied for by the operator of the storage facility.

Construction works for the new buildings

On 20 February, 2017, the foundation ceremony for the construction of the new workshop and office building of the FRM II and the laboratory and office building of the FZJ took place. Immediately afterward, the excavation and foundation work for the two buildings started. By the end of 2017, the structural work of the UYW workshop building had progressed so far that the outside walls had already been built up to the 2nd floor.

In the case of the more complicated UYL laboratory building, due to the extensive cellar the concreting work was completed up to the upper edge of the basement ceiling.

These multiple projects represent a continuing additional challenge to the reactor operation division due to the often associated administrative procedures caused by the regulatory framework in a nuclear facility. At the same time, FRM II staff are also involved in other projects such as the dismantling of the FRM (old) and related preparations, the planning of the dismantling of a former cyclotron accelerator located on the site of the FRM II as well as additional tasks necessitated by the nuclear fuel development laboratory that is operated under license according to § 9 AtG.

Quantitative comparability of heavy ion and in-pile irradiation experiments

J. Shi, H. Breitzkreutz, W. Petry

Forschungs-Neutronenquelle Heinz Maier-Leibnitz (FRM II), Technical University of Munich, Garching, Germany

Irradiation with heavy ions from an accelerator source can quickly reproduce and simulate certain aspects of in-pile irradiation tests and thus avoid the complexity and high costs of handling highly radioactive samples. In the last few years, the technique has advanced from feasibility, via qualitative analysis to quantitative prediction. One prominent application is the conversion of High Performance Research Reactors that currently use highly enriched uranium to low enriched uranium using the newly developed uranium-molybdenum (UMo) fuels. This has considerably hastened fuel development.

In accelerator based out-of-pile experiments, Iodine-127 with an energy of 80 MeV serves as a representative fission product. Samples are, for the most part, prepared from tailored model systems that consist of an Aluminium substrate, an optional coating layer of a few 100 nm and a $\leq 5 \mu\text{m}$ thin UMo layer on top. Often, the order is reversed and UMo serves as the substrate with a $\leq 13 \mu\text{m}$ thick Al layer on top. The model systems were produced by Physical Vapor Deposition (PVD) in the Uranium lab of FRM II.

Irradiations were performed at the Maier-Leibnitz Laboratorium (MLL) in a dedicated irradiation set-up (Fig. 1). The sample can be cooled and heated in a temperature range between 30°C and 300°C.

The interdiffusion layer

During irradiation, an interdiffusion layer (IDL) forms between the UMo and the surrounding Al. Due to its inferior irradiation properties, the IDL can lead to exponential fuel swelling and therefore needs to be avoided. IDL growth in the reactor follows an Arrhenius-like formula, which can be used to predict the thickness d_{IDL} of the interaction layer formation between the UMo and Al during irradiation:

$$d_{\text{IDL}}^2 = A f^{\rho} \exp\left[-\frac{q}{T}\right] t \cdot f_{\text{Mo}} f_{\text{Si}} \quad (1)$$

Here, $A = 2.6 \cdot 10^{-8} \mu\text{m}^2 \text{cm}^{3\rho} \text{s}^{\rho-1}$ is the proportionality factor, $\rho = 0.5$ the power of the fission rate \dot{f} averaged over the irradiation time t and $q = 3850 \text{ K}$ the fit parameter that includes the activation energy for the average irradiation temperature T . f_{Mo} and f_{Si} are correction factors for the fuel composition.

One of the key points is the conversion of the ion flux ϕ to the corresponding fission rate equivalent, $\dot{f} = \frac{1}{2} \phi \xi$, where ξ is the relative total energy deposition that was calculated using SRIM/TRIM. An inverse Al/UMo system with the Bragg peak near the interface was irradiated to study the growth dynamics of the IDL and verify the flux-fission rate conversion mechanism. The beam had a 2D-Gaussian profile and the five samples therefore cover a large variety of fission rate and burn-up equivalents. The samples were irradiated at five different temperatures between 383 K and 548 K and for different time spans (3.5 h to 12.5 h). For this irradiation geometry, $\xi = 0.21 \mu\text{m}^{-1}$ was calculated.

Fig. 2 shows the deviation between the expected and measured IDL thickness. Even though significant scattering is present, which is attributed to the general fluctuation of IDL thicknesses that is also observed in-pile, prediction and measurement match very well within the uncertainties of the experiment and the assumed uncertainties of the in-pile-equation ($\sim 15\%$). The proportionality constant was repro-

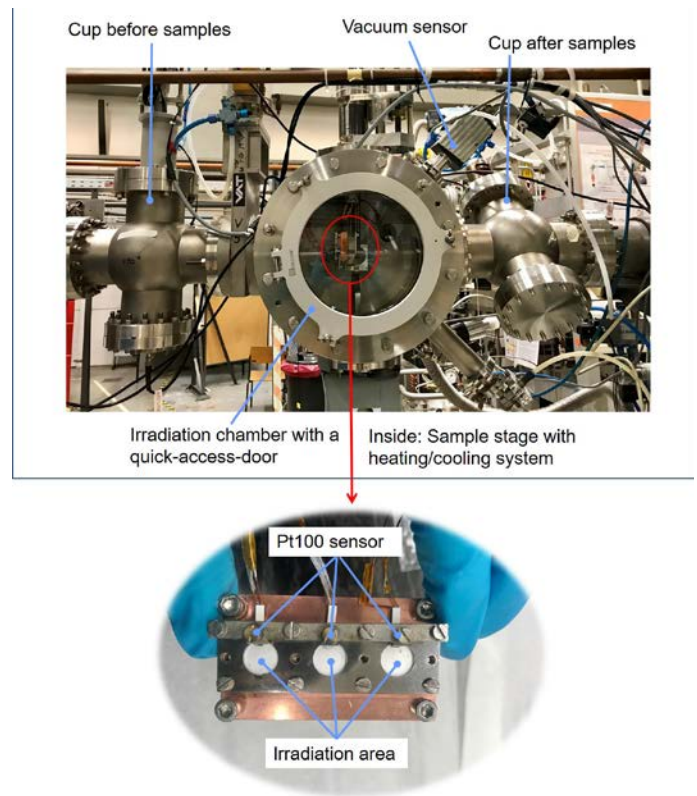


Figure 1: Irradiation set-up for heavy ions irradiation of small fuel samples with I-127 at the MLL accelerator facility. The sample holder offers 3 irradiation positions and temperature sensors, electrical heating, air cooling and a faraday blend.

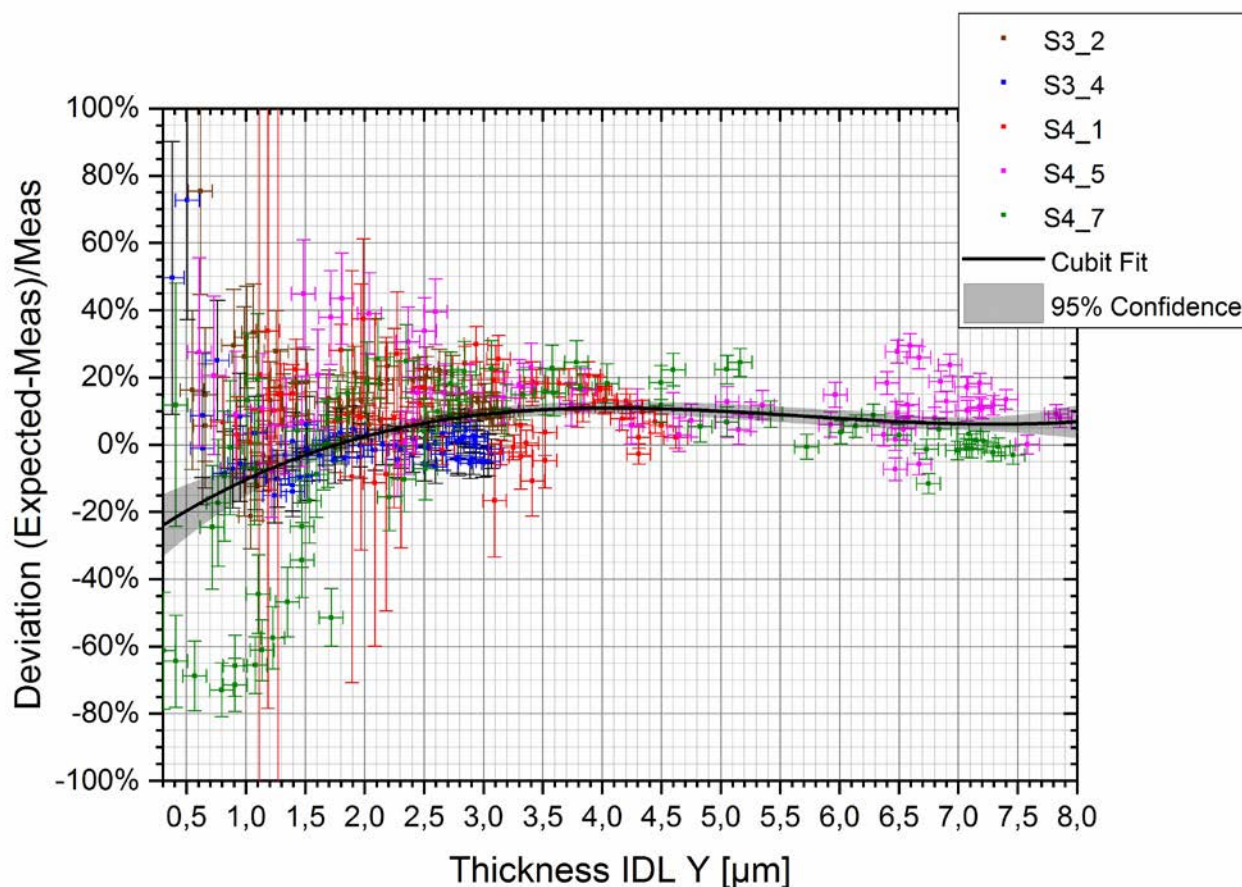


Figure 2: Deviation of the measured IDL thickness compared to the value expected from in-pile irradiations, i.e. y-axis is the difference between the expected and measured values, divided by the measured value. The use of a cubic fit is arbitrary to visualize a trend. $S_{x,y}$ are the sample names.

duced with an accuracy of 10 %. It was furthermore shown that p is constant over several orders of fission rates and the dependency $d_{IDL} \sim \sqrt{t}$ was also established for the early growth of the IDL. The temperature normalization q was verified by comparing the value obtained from the fit results of ion irradiation data (3906 K) and that from in-pile data (3850 K).

These quantitative ion experiments with matching thicknesses and the growth dynamics of out-of-pile produced IDLs with predictions based on in-pile data verify the current understanding of the Arrhenius-like in-pile IDL growth, as well as the conversion between ion flux and fission rate.

Composition

IDLs generated in-pile usually consist of UAl_3 with far smaller amounts of UAl_2 and UAl_4 , and are amorphous. Early ion experiments lead to partially crystalline IDLs, but improved sample cooling and the use of monolithic samples allowed for a fully amorphous IDL. Recent experiments led to IDLs with a U/Al ratio between $\frac{1}{3}$ and $\frac{1}{4}$ as identified by EDX. This is in reasonable agreement with in-pile results; IDL composition depends on the irradiation temperature, fission rate and fission density, making exact comparisons difficult. Ion

and in-pile experiments did not show ternary $U_xMo_yAl_z$ phases as do purely thermal-driven diffusion couple experiments, which underlines the necessity for irradiation to correctly reproduce IDL growth. Also, the nearest neighbour distances agree well (in-pile between 0.239 nm and 0.251 nm, out-of-pile 0.248 nm).

Conclusion

All in all, the experiments demonstrate very well the applicability of the approach of using Iodine-127 irradiation for qualitative, and even quantitative, experiments to reliably simulate numerous in-pile irradiation effects. Even though the burn-up equivalent reached with ions up to now has been comparably low ($\leq 6 \cdot 10^{20}$ fiss/cm³), important contributions have been made to the development of UMo fuels.

The main advantage of this technique is its effectiveness: No additional radioactivity is involved, the complete cycle from experiment design, through irradiation to post irradiation examinations can be carried out in a few weeks. Even though the method has obvious limitations, it is well able to minimize the number of expensive and time-consuming in-pile irradiation experiments.

Figures, numbers and information about visitors, events, staff and publications are presented in the chapter Facts & Figures.



Facts & Figures

The year in pictures

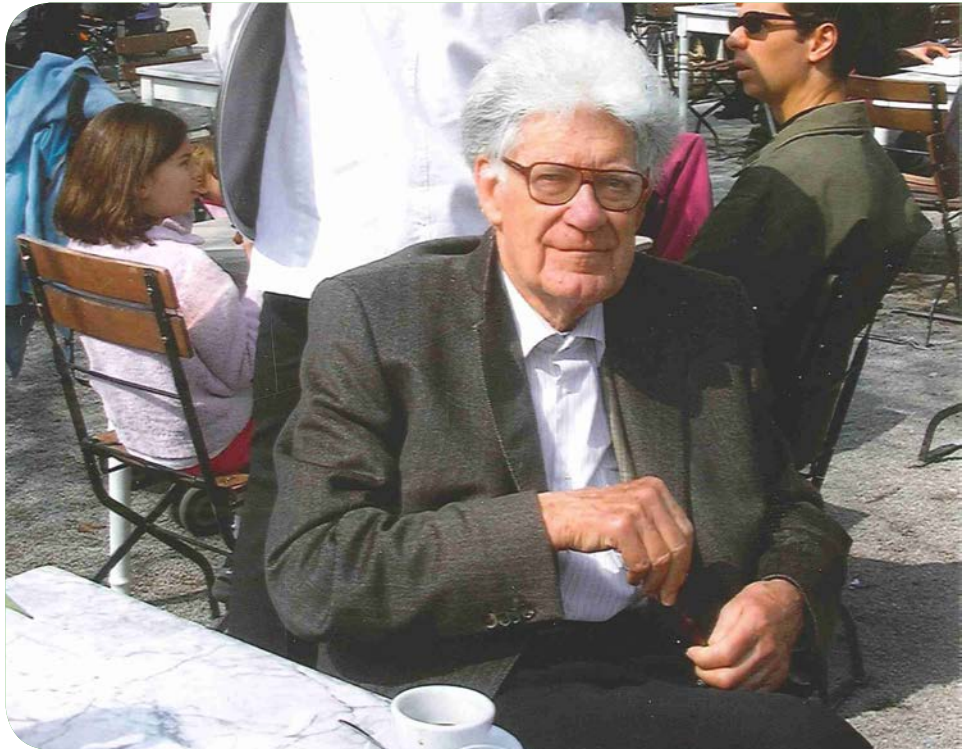


February 2nd

Fascinating physics: Dr. Astrid Schneidewind delivers a talk on neutron scattering to pupils at the "Schülertag" of the Technical University of Munich.

March 3rd

Sad news: It is with great sadness that we have to report that Emeritus professor Dr. Tasso Springer has passed away at the age of 86. He was one of the first students of Prof. Dr. Heinz Maier-Leibnitz, in whose honour the FRM II and MLZ are named. Together with his mentor, he discovered and developed the principle of guiding neutrons by mirroring at the atomic egg, i.e. the neutron guides.



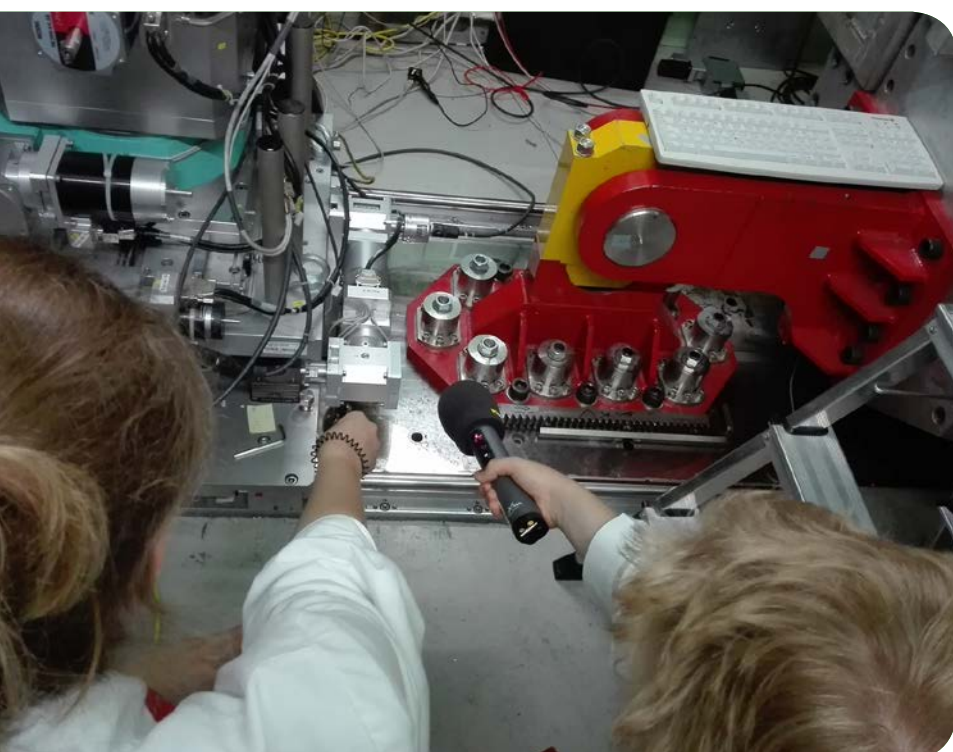
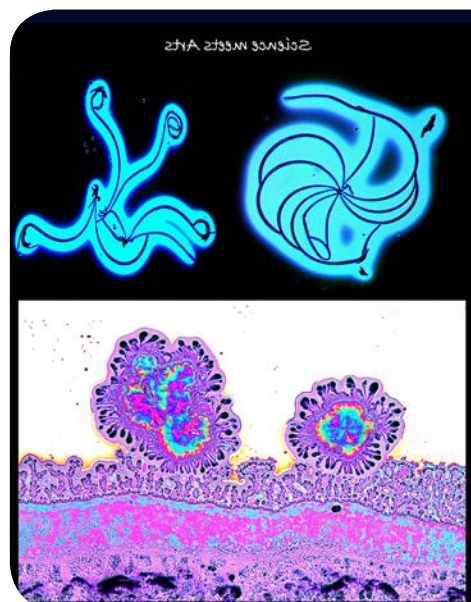
March 9th

On the home straight: for molybdenum-99 FRM II technicians and engineers have tested the mock-up facility under water.



April 1st

Science meets Art: The micrograph image of a thin film of indomethacin, a pain reliever from the group of non-steroidal anti-inflammatory drugs, looks artistic. Armin Kriele, a member of the Material Science Laboratory of the MLZ, entered his picture into a competition for scientific photos (Cerfa Photon 2017) in Munich and has reached the final round.



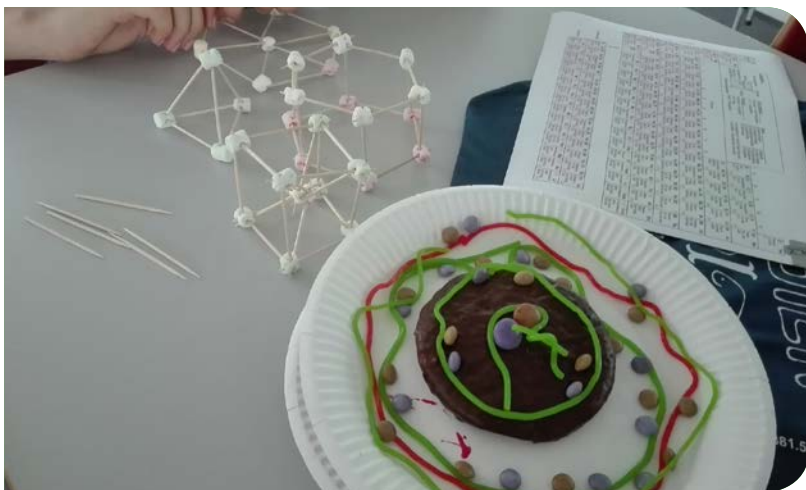
June 28th

How does the FRM II sound? Architectural students have recorded the sound of the neutron source. The result is a walk-in wooden model of the Atomic Egg, where the visitor can listen to different sounds and interviews with scientists. It was presented in an art exhibition in Munich and at the open door day of the Garching campus.

July 17th

Taster-day for a student with Dr. Sabine Pütter (right) in the Thin Film Lab of the MLZ.





August 3rd

Physics can also taste very sweet – this is one of the things that 11-13 year old girls learned during their girls only physics and technics workshop. They got a tour of the FRM II and built their own robots as well as cookie atoms.

August 4th

Visit from Berlin: Florian Hahn (left), Member of the German Parliament, met Prof. Dr. Winfried Petry and had a look at the instruments in the neutron guide hall west. The Scientific Director of the FRM II gave the representative of the constituency München-Land a brief insight into the science of the Heinz-Mai-Leibnitz Zentrum.



September 14th

New chairmen: Dr. Astrid Schneidewind from the MLZ, Forschungszentrum Jülich, is the new chair of the Komitee Forschung mit Neutronen, representing the German neutron users. Prof. Dr. Markus Braden (University of Cologne) was elected vice-chair.

September 27th

Forging a partnership for the construction of a new neutron source in Buenos Aires, Argentina (from left): Dr. Javier Santisteban, Scientific Director from Laboratorio Argentino de Haces de Neutrones (LAHN), Miguel Vicente Alvarez, Gabriel Juarez, Manuel Suarez, all three scientists at LAHN, Karina Pierpauli, Director of Administration at LAHN, and Dr. Michael Hofmann, instrument scientist at the MLZ.



October 10th

Neutrons for the council meeting: The community council of the neighbouring town Ismaning visited and toured the FRM II.

October 21st

Celebration for the Egg: The open day offered a special exhibition on the occasion of the 60th birthday of the Atomic Egg, the first nuclear reactor in Germany.





November 6th

Tour for communicators: The German Nuclear Society held part of their annual workshop for public relation officers at the FRM II where Prof. Dr. Winfried Petry gave a tour.

November 9th

Fishing for academics: The MLZ regularly offers internships, postgraduate opportunities and positions at the Hochschulkontaktmesse in Munich, where students and young academics look for jobs.

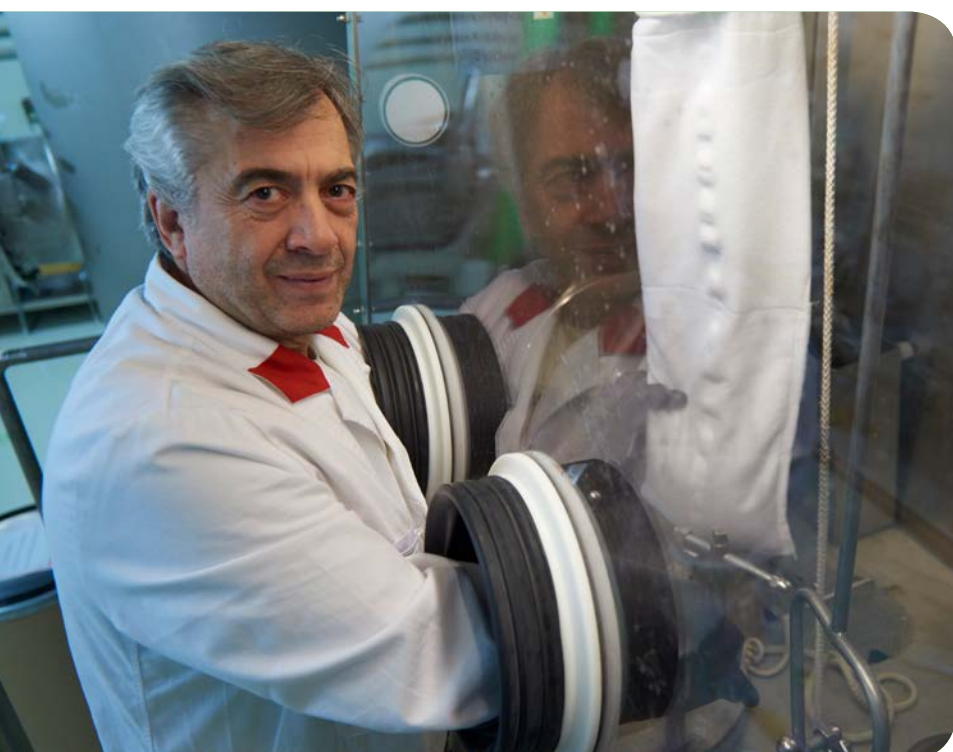
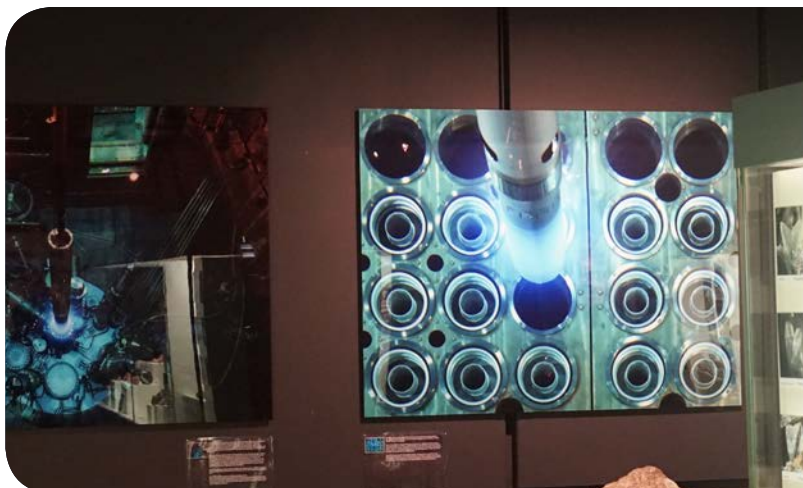


November 10th

One step closer to ultra-cold neutrons: Engineer Linus Willerding and his team worked on changing the plug of the beam tube no. 6a for the insertion of the future ultra-cold neutron source.

November 15th

MLZ goes museum: The pictures of the photographer Bernhard Ludwig showing motifs of the FRM II and MLZ are exhibited in the museum "Reich der Kristalle" in Munich.

**November 21st**

Our staff member of the year: Ismail Zöybek has developed a novel filtration process for the cleaning of wastewater. This saves the FRM II costs and earned him a personal thank-you letter from the Bavarian Minister of Science, Education and the Arts.

December 13th

Growing up in the air: The two new office, workshop and laboratory buildings have gained height since the ground breaking ceremony in February. The construction site of the new campus building Galileo is visible in the background.

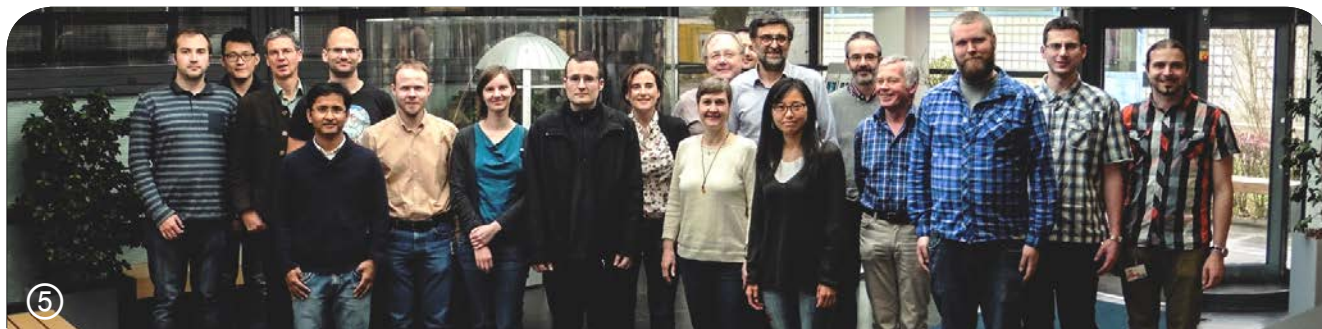


Workshops, Conferences and Schools

①	Neutrons in Research and Industry, weekly seminar	January 9 th - December 11 th	Garching, TUM
②	MATRAC 2 – Winter School 2017	February 27 th - March 3 rd	Garching, GEMS
③	Invenio User Group Workshop	March 21 st - 24 th	Garching, MLZ
④	DGK Workshop Breaking the Walls: Complementary of Synchrotron and Neutron Scattering	March 30 th - 31 st	Karlsruhe, MLZ, DGK
⑤	Triple axis resolution workshop	April 3 rd - 4 th	Garching, MLZ
⑥	PARI 2017: 2 nd Workshop on Public Awareness of Research Infrastructures	May 29 th - 30 th	Garching, MLZ
⑦	F-Praktikum, Hands-on training for physics students	May 29 th - June 2 nd	Garching, TUM



⑧	MLZ Conference “Neutrons for Health”	June 27 th - 30 th	Bad Reichenhall, MLZ
⑨	IAEA Training Workshop AUNIRA	August 28 th - September 1 st	Garching, MLZ
⑩	21 st JCNS Laboratory Course – Neutron Scattering	September 4 th - 15 th	Garching / Jülich, JCNS, RWTH Aachen
⑪	11 th Plenary meeting of the European Observatory on the supply of medical radioisotopes	October 2 nd	Garching, TUM
⑫	JCNS Workshop: Trends and Perspectives in Neutron Scattering: Probing Structures and Dynamics at Interfaces and Surfaces	October 10 th - 13 th	Tutzing, JCNS
⑬	Jana 2006 Workshop on Rietveld refinement of powder or single crystal diffraction data	October 26 th - 27 th	Garching, MLZ
⑭	Accelerator Meeting	November 15 th	Garching, TUM



From science to society

C. Hönl, C. Kortenbruck, B. Tonin-Schebesta, A. Voit

Heinz Maier-Leibnitz Zentrum (MLZ), Technical University of Munich, Garching, Germany

We are pleased to be able to look back on quite a productive year, with an all-time high of 3692 visitors and extensive media coverage. Two photo exhibitions on neutron research, two public talks and a special exhibition for the open day marked the 60th birthday of the Atomic Egg. Another even more successful MLZ- and ESO-workshop, aimed at increasing public awareness of research infrastructures, took place at the European Southern Observatory (ESO). Finally, two new brochures were published.

Photo and art exhibitions

2017 saw the 60th birthday of the „Atomic Egg“ and at the same time the anniversary of the first neutrons produced in Germany. Besides a press release that stimulated 42 articles in the press and on TV covering that celebration, we organised our own photo exhibition that was presented in Garching and at the Museum „Reich der Kristalle“ in Munich. The photographer Bernhard Ludewig, an artist from Berlin who visited the FRM and FRM II in 2015 and 2016, took some interesting photos. The TUM Faculty of Architecture initiated a students' project „Science and Art“. Four of them built a walk-in wooden model of the „Atomic egg“, where visitors could listen to explanations about, and sounds from, the reactor. This was the main attraction at our special exhibition on the annual open day. Some other relics of the „Atomic egg“ completed this exhibition and found many interesting visitors, especially since two contemporary witnesses were able to talk about all aspects of the old days.



Figure 1: The film crew in action at the shooting of the new video about ⁹⁹Mo-production at FRM II.

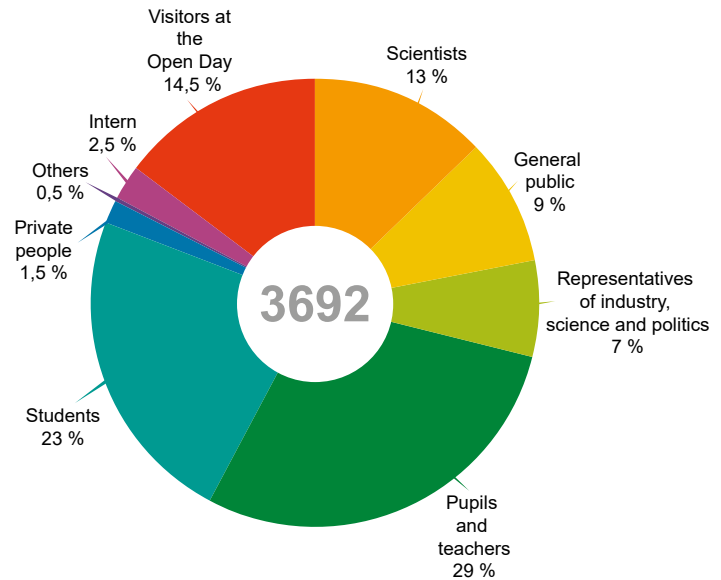


Figure 2: What background did the visitors in 2017 have?

Film production

However, we did not only dig into the past, but also drew attention to a new subject: the future production of ⁹⁹Mo for medical purposes. A new, 6 minute film sets out the reason why it is being produced at FRM II, the technical problems its production involves, and their solution. The film is available in German and English and was uploaded onto the TUM YouTube channel, where it has already attracted many interested users.

New working group for research infrastructures

Following the successful ERF workshop on public awareness of research infrastructures (PARI) in 2015, a second forum was organised in 2017. This workshop was even more successful as we were able to boost the number of visitors by 60 % and saw many very interesting contributions from all over Europe. Immediately after the workshop, which took place in cooperation with the European Southern Observatory and at their conference center, a special working group (RICE – Research Infrastructures Communications and Engagement) was founded to foster exchange between the large-scale facilities, plan common projects and organize the next PARI workshop in 2019.

Talk, technics and taster-day

Another approved cooperation was also successful in 2017: the German Museum in Munich invited Prof. Dr. Winfried Petry to give a talk. According to the organizer of this talk se-



Figure 3: The four students of the TUM Faculty of Architecture posed in front of the “Atomic Egg”, which they rebuilt as a wooden model.

ries (“Science for everybody”), this was “the most successful in the last season”.

Cooperation between the TUM Physics Department, the Gerda-Stetter-Foundation and the MLZ continued: A 3-day workshop on physics and technics for girls only was exciting and satisfying as well. The girls, aged 11 to 13, learned a lot about the principles of optics, built and coded small mobile robots, and were finally treated to a tour through the FRM II. One young student approached us for a taster day at the neutron source. We organized half a day at the instrument TOF-TOF and another half day at the molecular beam epitaxy lab. This might be an experiment to follow up in the future.

New brochures for residents and visitors

We published two new brochures in 2017: The information booklet “Safety first!” was reissued and distributed to households in Garching and the surrounding area. It is available in German and, for the first time, also in English.

The new English brochure “Neutrons for Research” is aimed at foreign scientists who are interested in making measurements at the FRM II and informs non-German speaking visitors to the neutron source about the numerous applications of neutron research.



Figure 4: The photo exhibition to mark the “Atomic Egg’s” birthday was mounted in the museum “Reich der Kristalle” in November as a special exhibition.

Media coverage

In 2017, 170 media contributions were published on the research neutron source FRM II and the Heinz Maier-Leibnitz Zentrum. Radio and television teams visited the neutron source four times this year. The FRM II and the MLZ, together with their partners, have sent out seven press releases this year.

Another focus is still on updates for the two homepages www.frm2.tum.de and mlz-garching.de. Here, we wrote 43 news for 2017. We posted 52 times on the FRM II facebook page, often on other topics or in addition to the websites.

Visitors and open day

The number of visitors was higher than ever before: almost 4000 this year! The most popular month was, not surprisingly, October with more than 500 visitors at the Open day, but also 382 during the other October days. Another favorite month was July with 385. 56 % of our visitors in 2017 came from Germany, 14 % from other European countries and 30 % from Asia, Australia and America. The visitor office offers guided tours in German and English, but also in other languages such as Chinese, Russian, Spanish or Italian, so they are well prepared for another stampede of visitors in 2018.

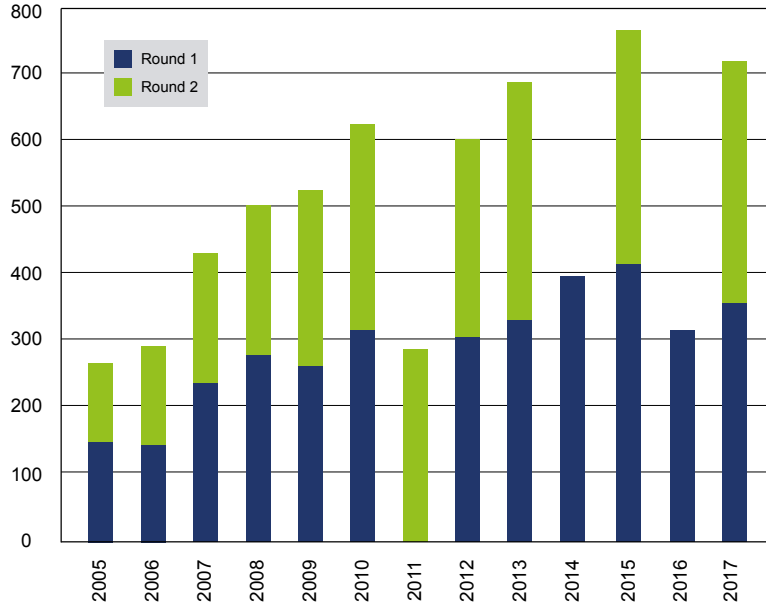


Figure 5: The PARI workshop 2017 was the second of its kind with now 120 participants, followed by the setting-up of the RICE working group for the third workshop in 2019, sharing of best-practices and other common projects.

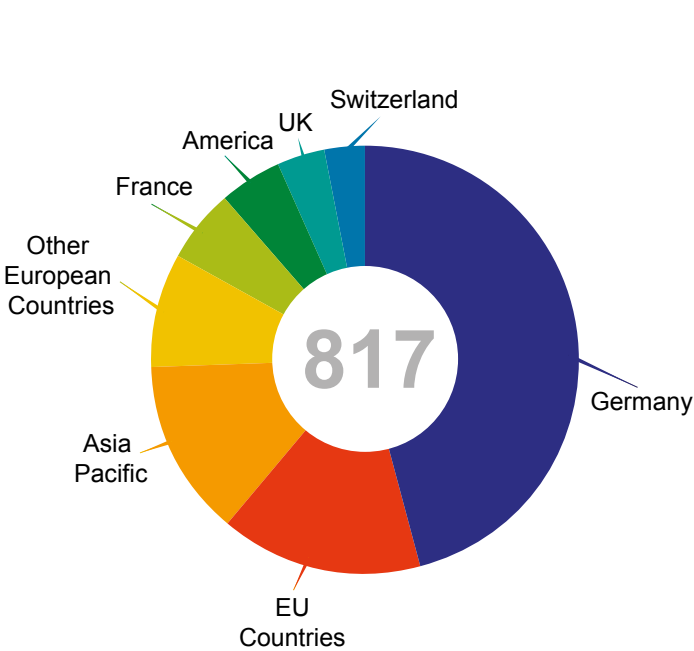
Behind the scenes – At the User Office in 2017

R. Bucher¹, F. Carsughi¹, C. Hönl², I. Lommatzsch², B. Tonin²

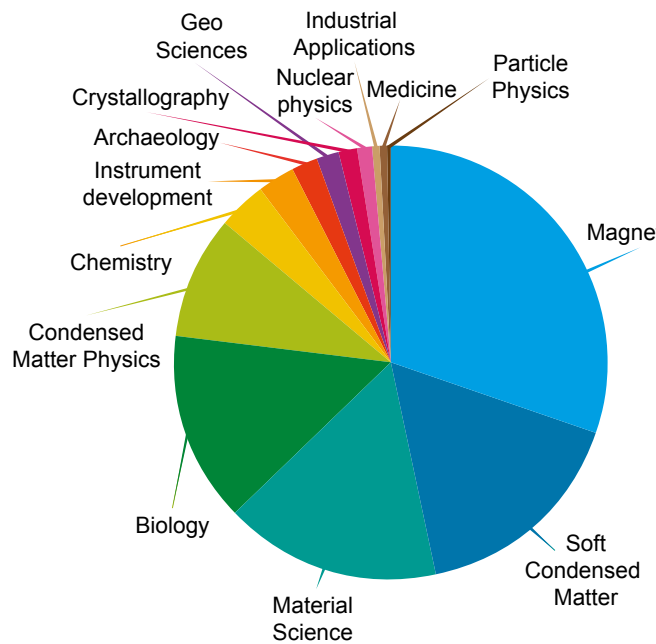
¹Jülich Centre for Neutron Science (JCNS) at MLZ, Forschungszentrum Jülich GmbH, Garching, Germany; ²Heinz Maier-Leibnitz Zentrum (MLZ), Technical University of Munich, Garching, Germany



Proposals submitted since the start of user operation at FRM II.



Where did the main proposers of all 817 proposals submitted in 2017 come from?



Which scientific fields did the proposals submitted in 2017 cover?



2469

Users have a lot of questions about the beam time itself, their stay at the MLZ, preparations relating to radiation protection, access to the site, hotel bookings, public transport, the reimbursement of any travel costs – and so much more!

Most users email their questions to useroffice@mlz-garching.de and thus we responded to 2469 emails this year!



831

We emailed a total of 831 invitations to main proposers for experiments this year.

These experiments had been scheduled at our instruments by the instrument scientists and, through them, our users were informed of the exact dates of their beam time and how to prepare for the visit here in Garching.

3055



The hotels in Garching had good reason to smile in 2017: We booked a total of 3055 nights for our users.

Reservation via the User Office is mandatory for those users requesting reimbursement, but we offer this service to all our guests! We also take care of any cancellations, as well as changes to the bookings.



1142

We dealt with 1142 applications for visits in the context of an experiment at the MLZ. All those users completed the form “Arrival_Departure” in their personal account at the On-line User Office System.

We have to check whether the dates given, as well as the proposal number, are correct and if the user has provided all personal details, we need to organise access to the site. Our Security Department grants access on this basis and in the end, this form helps to create the content of the blue folders all users get when entering the MLZ.

159



Some of our users need special letters of invitation for visa purposes – for example those coming from China, India or Russia. They are required to complete a lot of paperwork in order to organise their visit to the MLZ.

In 2017, we wrote 159 such letters based on a text accepted by the German Embassies worldwide, signed them, and sent them by courier to the expectant users.

Organisation

FRM II and MLZ

The Forschungs-Neutronenquelle Heinz Maier-Leibnitz (FRM II) provides neutrons for research, industry and medicine and is operated as a Corporate Research Centre by the Technical University of Munich (TUM). The scientific use of the FRM II, with around 1000 user visits per year, is organized within the "Heinz Maier-Leibnitz Zentrum" (MLZ).

The chart below shows the overall network comprising the neutron source FRM II and the MLZ, as well as the funding bodies and the scientific users performing experiments at the MLZ addressing the grand challenges of our todays society.

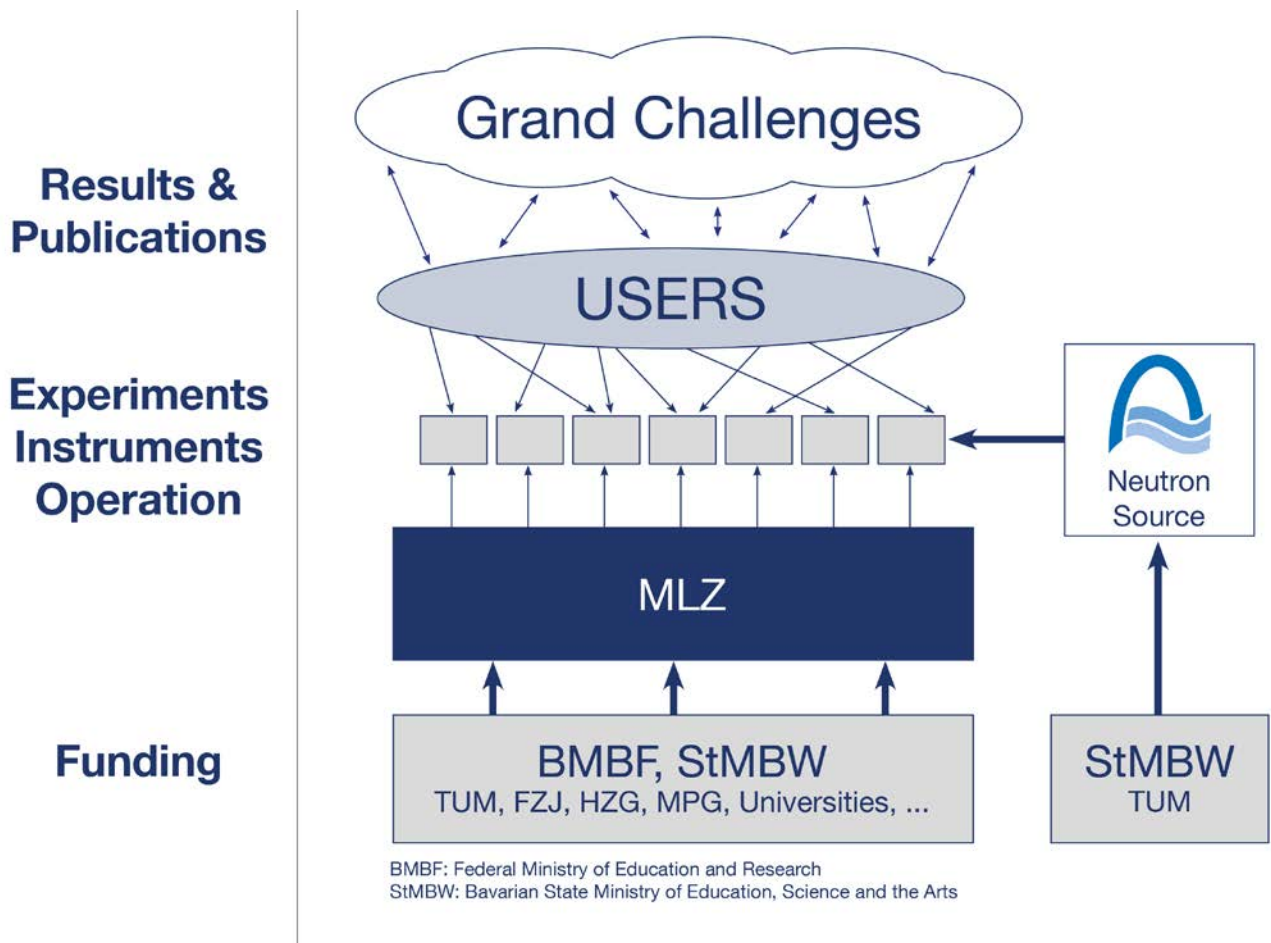


Figure 1: The neutron source FRM II and the user facility MLZ.

Scientific Director MLZ, HGF

Prof. Dr. Thomas Brückel

Technical Director FRM II

Dr. Anton Kastenmüller

Scientific Director MLZ, FRM II

Prof. Dr. Winfried Petry

Administrative Director FRM II

Johannes Nußbickel

Scientific Cooperation at the Heinz Maier-Leibnitz Zentrum (MLZ)

The Heinz Maier-Leibnitz Zentrum with its cooperation partners Technische Universität München (TUM), Forschungszentrum Jülich (FZJ) and Helmholtz-Zentrum Geesthacht (HZG) is embedded in a network of strong partners including the Max Planck Society (MPG) and numerous university groups exploiting the scientific use of the Forschungs-Neutronenquelle Heinz Maier-Leibnitz. The organizational chart of the MLZ is shown below.

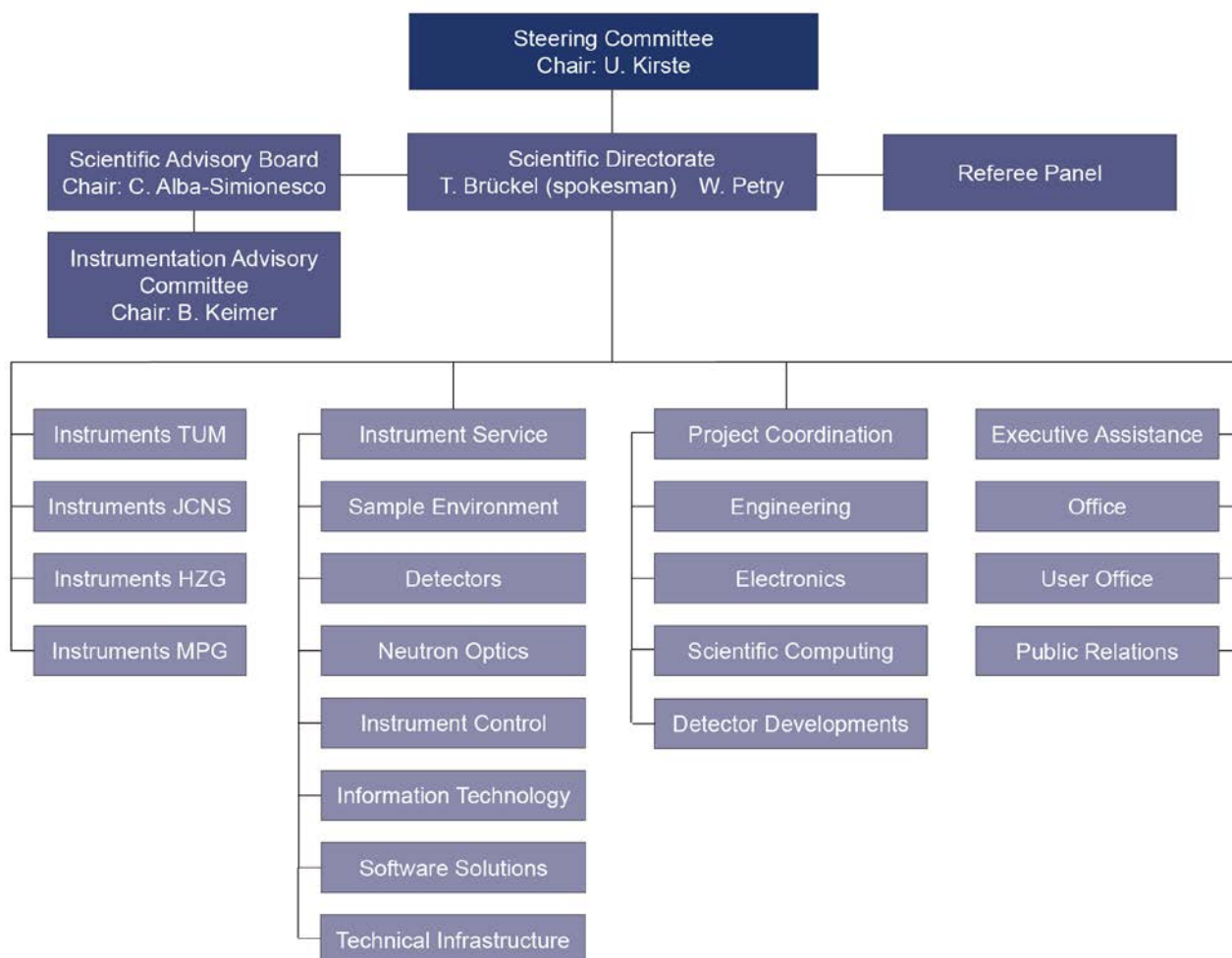
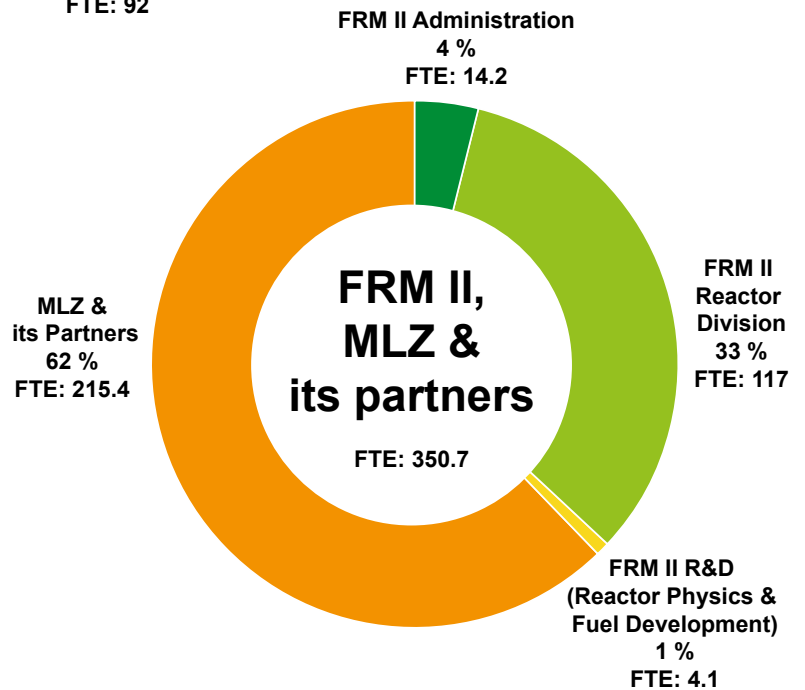
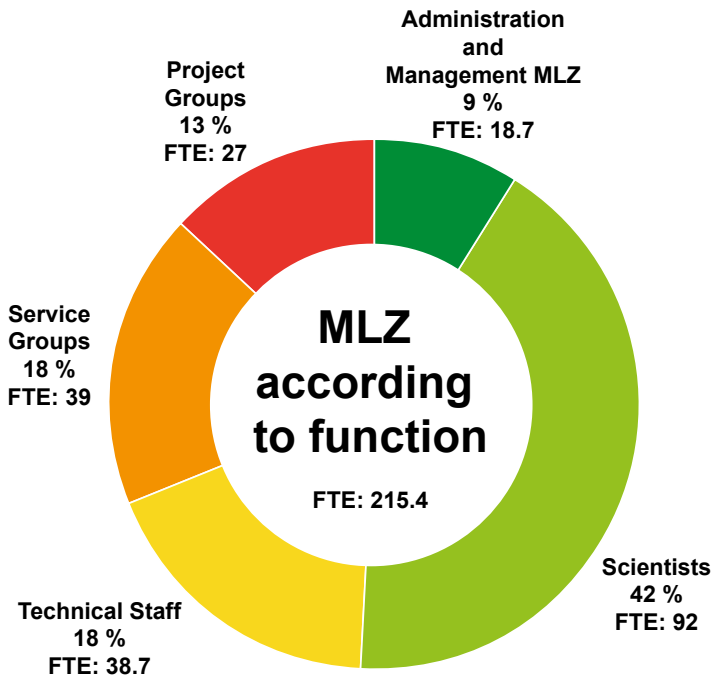
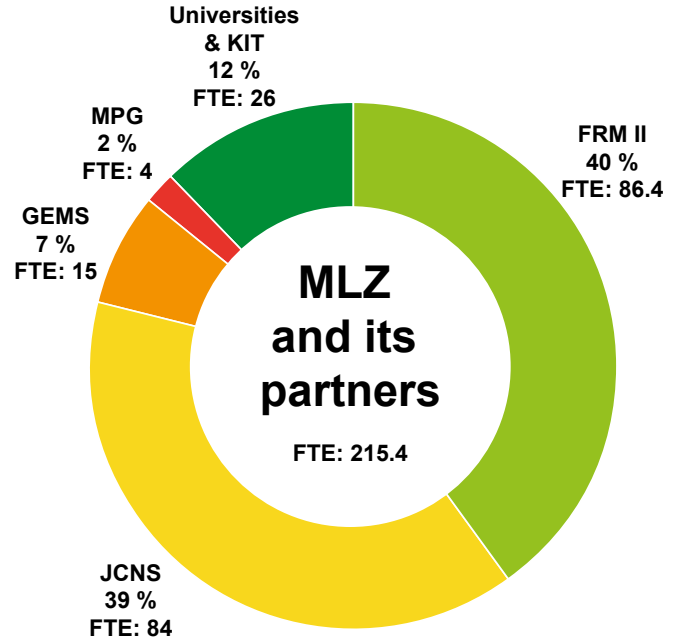


Figure 2: Organisational chart MLZ.

Staff

The charts below show the staff of MLZ and FRM II. The staff of MLZ according to its share among the partners with a detailed view according to the function within the MLZ is depicted as well.



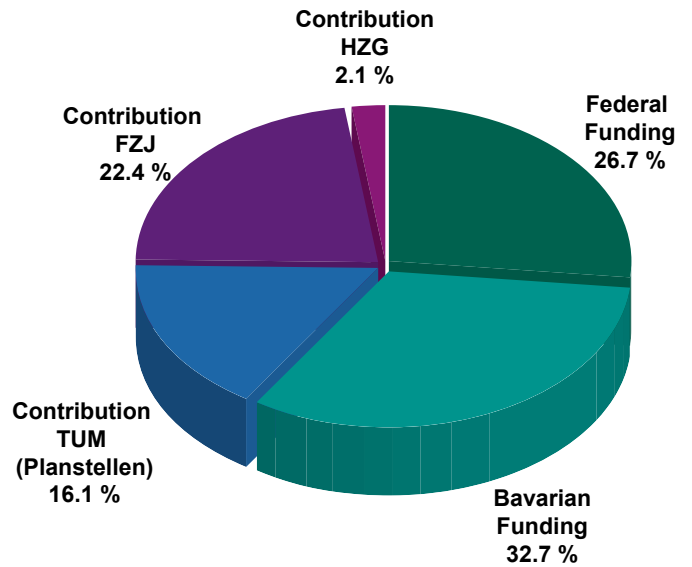
FTE = Full Time Equivalent

Budget

The tables and charts below show the revenue and expenses in 2017.

Revenue 2017

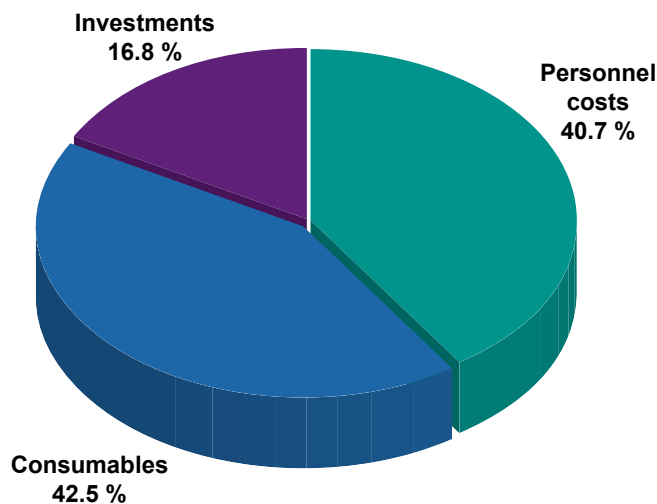
Federal Funding	16.700.000 €
Bavarian Funding	20.420.110 €
Contribution TUM (Planstellen)	10.045.955 €
Contribution FZJ	13.962.312 €
Contribution HZG	1.320.000 €
Total	62.448.377 €



Expenses 2017*

	TUM (€)	FZJ (€)	HZG (€)	Total (€)
Personnel costs	16.142.541	8.468.069	1.396.000	26.006.610
Consumables	22.496.892	4.280.368	386.000	27.163.260
Investment	4.321.142	5.745.436	650.000	10.716.578
Total	42.960.575	18.493.873	2.432.000	63.886.448

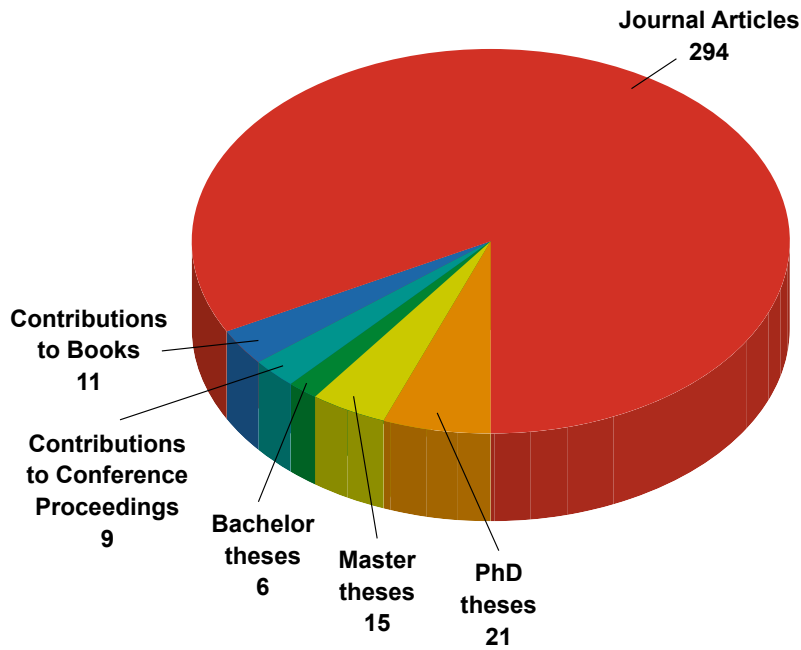
*Spending for construction costs for laboratory and office building and for science and workshop building are not included



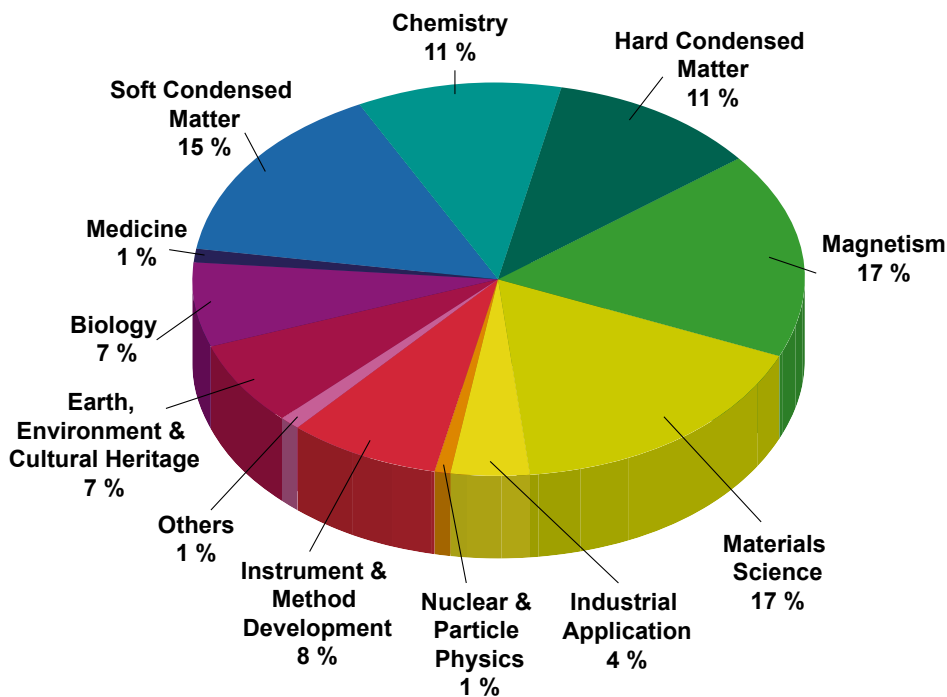
Publications & Theses

In 2017, we received notice of a total of 314 scientific publications, including journal articles, contributions to books and conference proceedings (<https://impulse.mlz-garching.de/> and figure below). Furthermore, in total 42 theses supervised by staff of the scientific cooperation partners were completed in 2017.

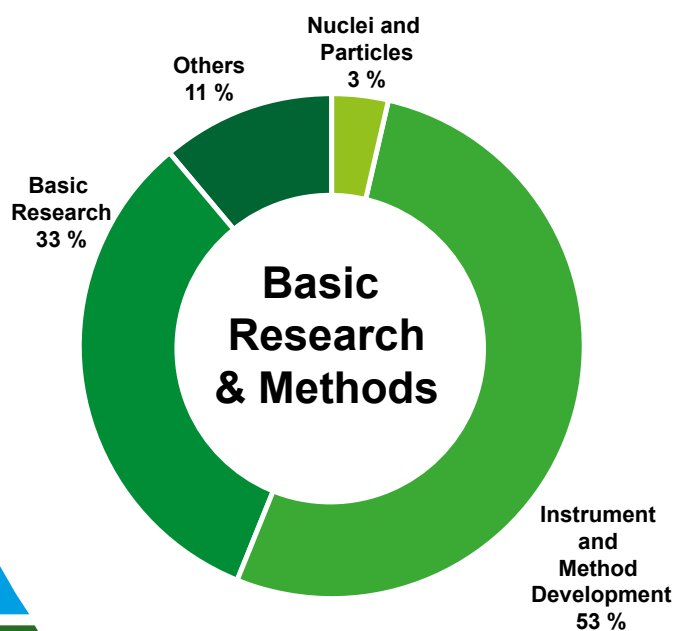
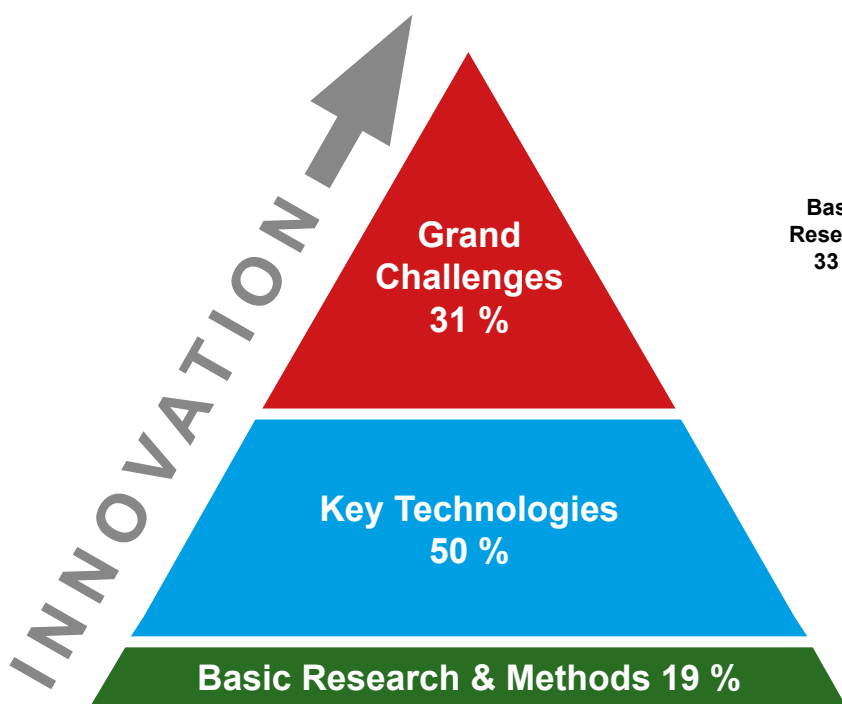
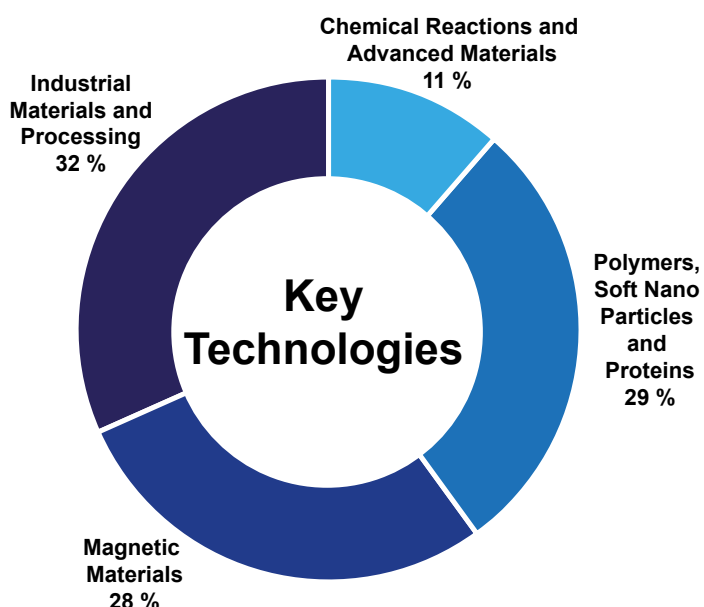
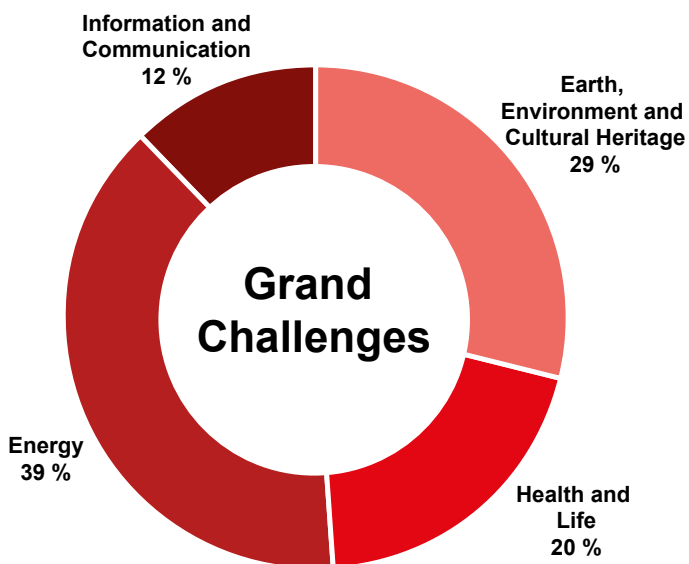
In 2017 more than 210 PhD theses, based on experiments at the MLZ and including external users, were either ongoing or completed. Of these, about 140 are under the direct supervision of staff at the MLZ and its collaboration partners. About 79 % of all doctoral students come from German universities, 17 % come from other universities in Europe and 4 % from the rest of the world.



The next figure shows the classification of the journal articles by Scientific Area (several tags per journal article are possible):



The journal articles at the MLZ can be classified according to a pyramid: from Basic Research & Methods (19 %) required to tackle the Key Technologies (50 %), which address directly the Grand Challenges of our today's society (31 %). The circular charts represent the individual subjects being dealt within these three categories.



Organisation

Steering Committee

Chair

Dr. Ulrike Kirste
Bavarian State Ministry of Education, Science and Arts

Members

Prof. Dr. Sebastian Schmidt (Vice Chair)
Board of Directors of Forschungszentrum Jülich GmbH

Albert Berger
Senior Executive Vice-President
Technical University of Munich

Thomas Frederking
Member of the Executive Board of
Helmholtz-Zentrum Berlin GmbH

Prof. Dr. Dr. h.c. mult. Wolfgang A. Herrmann
President
Technical University of Munich
represented by Prof. Dr. Thomas Hofmann
Vice-President
Technical University of Munich

Prof. Dr. Wolfgang Kaysser
Member of the Executive Board of Helmholtz-Zentrum
Geesthacht GmbH

Dr. Jürgen Kroseberg
Federal Ministry for Education and Research

Prof. Dr. Stephan Paul
Technical University of Munich
Physics-Department E18

Guests

Prof. Dr. Thomas Brückel
Scientific Director of the MLZ, representing HGF institutions

Prof. Dr. Winfried Petry
Scientific Director of the MLZ, representing TUM

Dr. Anton Kastenmüller
Technical Director ZWE-FRM II,
Technical University of Munich

Johannes Nußbickel
Administrative Director ZWE-FRM II,
Technical University of Munich

Dirk Schlotmann
Forschungszentrum Jülich GmbH

RD Petra Lörz
Technical University of Munich, FRM II



Figure 1: Steering Committee (from left to right): P. Lörz, S. Paul, Th. Brückel, Th. Frederking, S. Schmidt, W. Petry, J. Nußbickel, U. Kirste, J. Kroseberg, D. Schlotmann, M. Müller, A. Berger



Figure 2: Scientific Advisory Board (from left to right): Ch. Rüegg, A. Guirao Blank, J. Rädler, H. Abele, W. Paul, A. Arbe, B. Keimer, R. von Klitzing, Th. Brückel, W. Petry, W. Daum, Chr. Alba-Simionesco, H. Schober.

Scientific Advisory Board

Chair

Prof. Christiane Alba-Simionesco
Laboratoire Léon Brillouin
CEA, Centre de Saclay

Prof. Dr. Bernhard Keimer
Max-Planck-Institut für Festkörperphysik, Stuttgart

Members

Prof. Dr. Hartmut Abele
Technische Universität Wien

Prof. Dr. Wolfgang Paul
Martin Luther Universität Halle-Wittenberg

Prof. Dr. Arantxa Arbe
Centro de Fisica de Materiales,
Material Physics Center, San Sebastián

Prof. Dr. Joachim Rädler
Ludwig-Maximilians-Universität, München

Alejandro Javier Guirao Blank
Volkswagen AG, Wolfsburg

Prof. Dr. Helmut Schober
Institut Laue Langevin, Grenoble

Werner Daum
Bundesanstalt für Materialforschung und -prüfung (BAM),
Berlin

Prof. Dr. Regine v. Klitzing
Technische Universität Darmstadt

Prof. Dr. Dirk Johrendt
Ludwig-Maximilians-Universität, München

MLZ Instrumentation Committee

Chair

Prof. Dr. Bernhard Keimer
Max-Planck-Institut für Festkörperphysik, Stuttgart

Prof. Dr. Catherine Pappas
Delft University of Technology, Delft

Members

Dr. Maria Teresa Fernandez Diaz
Institut Laue Langevin, Grenoble

Prof. Dr. Henrik Ronnøw
Ecole Polytechnique Fédérale de Lausanne

Dr. Eberhard Lehmann
Paul-Scherrer-Institut, Villigen

Dr. Margarita Russina
Helmholtz-Zentrum für Materialien und Energie, Berlin

Dr. Frederic Ott
Laboratoire Léon Brillouin, CEA Saclay

Dr. Ulli Köster
Institut Laue Langevin, Grenoble

Evaluation of Beam Time Proposals: Members of the Review Panels

Prof. Dr. Arantxa Arbe
Centro de Fisica de Materiales,
Material Physics Center, San Sebastián

Dr. Roberto Caciuffo
Institute for Transuranium Elements
JRC Karlsruhe

Prof. Peter Battle
Department of Chemistry
University of Oxford

Dr. Monica Ceretti
Institut Charles Gerhardt
Université de Montpellier 2

Dr. Matthew Blakeley
Institut Laue Langevin, Grenoble

Dr. Niels Bech Christensen
Institute of Physics
Technical University of Denmark, Kongens Lyngby

Dr. Victor Bodnarchuk
Frank Laboratory of Neutron Physics, Dubna, Moscow reg.

Dr. Daniel Clemens
Helmholtz Zentrum Berlin für Materialien und Energie, Berlin

Dr. Laszlo Bottyan
Hungarian Academy of Sciences
Wigner Research Centre for Physics, Budapest

Dr. Robert Cubitt
Institut Laue Langevin, Grenoble

Dr. Johann Bouchet
DAM
Commissariat à l'énergie atomique et aux énergies
alternatives, Arpajon

Dr. Pascale Deen
European Spallation Source, Lund

Dr. Philippe Bourges
UMR12 CEA-CNRS
Laboratoire Léon Brillouin, Gif-sur-Yvette

Dr. Sabrina Disch
Department Chemie
University of Cologne

Prof. Roberto Brusa
Facoltà di Ingegneria / Dipartimento di Fisica
Università degli Studi di Trento

Dr. Cecile Dreiss
Institute of Pharmaceutical Science
King's College London

Prof. Dr. Kristina Edström
Department of Chemistry
Uppsala University, Uppsala

Prof. Dr. Stefan Egelhaaf
Lehrstuhl für Physik der weichen Materie
Heinrich-Heine-Universität, Düsseldorf

Prof. Dr. Helmut Ehrenberg
Institut für Angewandte Materialien
Karlsruher Institut für Technologie,
Eggenstein-Leopoldshafen

Dr. Stephan Eijit
Delft University of Technology, Delft

Dr. Bela Farago
Institut Laue Langevin, Grenoble

Dr. Tom Fennell
Laboratories for Solid State Physics & Neutron Scattering
Paul Scherrer Institute, Villigen

Dr. Peter Fouquet
Institut Laue Langevin, Grenoble

Dr. Victoria Garcia-Sakai
ISIS Neutron and Muon Source
STFC Rutherford Appleton Laboratory, Didcot

Prof. Giacomo Diego Gatta
Department of Earth Sciences "Ardito Desio"
Università degli Studi di Milano

Prof. Dr. Rupert Gebhard
Abt. Vorgeschichte
Archäologische Staatssammlung, München

Dr. Jens Gibmeier
Institut für Angewandte Materialien
Karlsruher Institut für Technologie,
Eggenstein-Leopoldshafen

Dr. Francesco Grazzi
Institute for Complex Systems
Consiglio Nazionale delle Ricerche, Sesto Fiorentino

Dr. Christian Grünzweig
Paul Scherrer Institute, Villigen

Dr. Thomas Hauss
Helmholtz Zentrum Berlin für Materialien und Energie, Berlin

Dr. Stephen Hayden
HH Wills Physics Laboratory
University of Bristol

Prof. Paul Henry
ISIS Neutron and Muon Source
STFC Rutherford Appleton Laboratory, Didcot

Dr. Klaudia Hradil
Röntgenzentrum
Technische Universität Wien

Dr. Nikolay Kardjilov
Helmholtz Zentrum Berlin für Materialien und Energie, Berlin

Dr. Christy Kinane
ISIS Neutron and Muon Source
STFC Rutherford Appleton Laboratory, Didcot

Dr. Reinhard Kremer
Max Planck-Institut für Festkörperforschung, Stuttgart

Prof. Dr. Christian Krempaszky
Fakultät für Maschinenwesen
Technical University of Munich, Garching

Prof. Jeremy Lakey
Institute for Cell and Molecular Biosciences
University of Newcastle, Newcastle upon Tyne

Prof. Dr. Martin Lerch
Institut für Chemie
Technische Universität Berlin

Dr. Reidar Lund
Department of Chemistry
University of Oslo

Dr. Sandrine Lyonnard
Commissariat à l'énergie atomique et aux énergies alternatives, Grenoble

Prof. Dr. Andreas Magerl
Kristallographie und Strukturphysik
Universität Erlangen-Nürnberg, Erlangen

Dr. Eric Mauerhofer
Institut für Energie- und Klimaforschung
Forschungszentrum Jülich

Dr. Andreas Michels
Faculté des Sciences, de la Technologie et de
la Communication
Université de Luxembourg

Prof. Dr. Peter Müller-Buschbaum
Lehrstuhl für Funktionelle Materialien
Technical University of Munich
Physik Department, Garching

Dr. Gwilherm Nénert
PANalytical B.V., Almelo

Prof. Dr. Thommy Nylander
Physical Chemistry
Lund University, Lund

Dr. Esko Oksanen
European Spallation Source, Lund

Dr. Alessandro Paciaroni
Dipartimento di Fisica
Università degli Studi di Perugia

Prof. Luigi Paduano
Chemistry Department
University of Naples "Federico II", Naples

Prof. Dr. Oskar Paris
Montanuniversität Leoben

Dr. Oleg Petrenko
Department of Physics
University of Warwick, Coventry

Dr. Thilo Pirling
Institut Laue-Langevin, Grenoble

Prof. Dr. Diana Lucia Quintero Castro
Faculty of Science and Technology
University of Stavanger

Dr. Navid Qureshi
Institut Laue Langevin, Grenoble

Dr. Florin Radu
BESSY
Helmholtz Zentrum Berlin für Materialien und Energie, Berlin

Dr. Stephane Raymond
Commissariat à l'énergie atomique et aux énergies
alternatives, Grenoble

Prof. Dr. Günther Redhammer
Materialforschung und Physik
Universität Salzburg

Dr. Sarah Rogers
ISIS Neutron and Muon Source
STFC Rutherford Appleton Laboratory, Didcot

Dr. Stephane Rols
Institut Laue Langevin, Grenoble

Dr. Matthias Rossbach
IEK-6
Forschungszentrum Jülich GmbH

Dr. Margarita Russina
Institut Weiche Materie und Funktionale Materialien
Helmholtz Zentrum Berlin für Materialien und Energie, Berlin

Prof. Dr. Michael Sattler
Department Chemie /
Lehrstuhl für Biomolekulare
NMR-Spektroskopie
Technical University of Munich, Garching

Dr. Harald Schmidt
Institut für Metallurgie
Technische Universität Clausthal, Clausthal-Zellerfeld

Prof. Dr. Andreas Schönhals
Bundesanstalt für Materialforschung und -prüfung, Berlin

Dr. Romain Sibille
Laboratory for Neutron Scattering
Paul Scherrer Institute, Villigen

Prof. Dr. Wolfgang Sprengel
Institut für Materialphysik
Technische Universität Graz

Dr. Jochen Stahn
Laboratory for Neutron Scattering
Paul Scherrer Institute, Villigen

Dr. Andreas Stark
Institute for Materials Research
Helmholtz Zentrum Geesthacht

Dr. Peter Staron
Institute of Materials Research
Helmholtz-Zentrum Geesthacht



Figure 3: Venue of the MLZ Review Panels' meeting at Munich airport.

Dr. Ross Stewart
ISIS Neutron and Muon Source
STFC Rutherford Appleton Laboratory, Didcot

Dr. Pavel Strunz
Department of Neutron Physics
Nuclear Physics Institute, Rez near Prague

Dr. Anne Stunault
Institut Laue Langevin, Grenoble

Dr. Laszlo Szentmiklosi
Center for Energy Research
Hungarian Academy of Sciences, Budapest

Prof. Dr. Katharina Theis-Broehl
Hochschule Bremenhaven

Prof. Dr. Regine von Klitzing
Fachbereich Physik
Technische Universität Darmstadt

Dr. Ing. Frank Weber
Institut für Festkörperphysik
Karlsruher Institut für Technologie,
Eggenstein-Leopoldshafen

Jun. Prof. Dr. Hongbin Zhang
Theory of Magnetic Materials
Technische Universität Darmstadt

Partner institutions

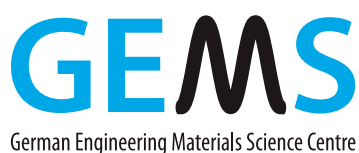


Bavarian Research Institute of
Experimental Geochemistry and Geophysics
University of Bayreuth
www.bgi.uni-bayreuth.de



Georg-August-Universität Göttingen

- Institute of Physical Chemistry
www.uni-pc.gwdg.de/eckold
- Geowissenschaftliches Zentrum
www.uni-goettingen.de/de/125309.html



German Engineering Materials Science Centre GEMS
Helmholtz-Zentrum Geesthacht GmbH
www.hzg.de/institutes_platforms/gems/



Jülich Centre for Neutron Science JCNS
Forschungszentrum Jülich GmbH
www.jcns.info



Karlsruhe Institute of Technology

- Institute for Applied Materials – Energy Storage Systems (IAM-ESS)
www.iam.kit.edu



Ludwig-Maximilians-Universität München

- Section Crystallography
www.lmu.de/kristallographie
- Faculty of Physics
www.softmatter.physik.uni-muenchen.de



MAX-PLANCK-GESELLSCHAFT

Max Planck Institute for Solid State Research
Stuttgart

www.fkf.mpg.de



RWTH Aachen University

- Institute of Crystallography
www.xtal.rwth-aachen.de
- Institute of Inorganic Chemistry
www.ac.rwth-aachen.de



Clausthal University of Technology

- Institute of Materials Science and Engineering
www.iww.tu-clausthal.de



Technische Universität Dresden

- Institute of Solid State Physics
www.tu-dresden.de/mn/physik/ifp



Technical University of Munich

Department of Physics

- E13 - Institute for Functional Materials
www.functmat.ph.tum.de
- E18 - Institute for Hadronic Structure and Fundamental Symmetries
www.e18.ph.tum.de
- E21 - Research area Strongly Correlated Electron Systems
www.sces.ph.tum.de
- RCM - Radiochemie München
www.rcm.tum.de



Klinikum rechts der Isar

Technical University of Munich

- MRI - Klinikum Rechts der Isar
www.mri.tum.de



Technical University of Munich

- Exzellenzcluster
„Origin and Structure of the Universe“
www.universe-cluster.de



TECHNISCHE
UNIVERSITÄT
WIEN
Vienna University of Technology

Vienna University of Technology

- Neutron- and Quantum Physics
Research area at the Atominstut Vienna
Abele Group
<http://ati.tuwien.ac.at/forschungsbereiche/nqp/home/>



Universität der Bundeswehr München

- Institute of Applied Physics and Measurement
Technology
www.unibw.de/lrt2

Universität zu Köln



University of Cologne

- Faculty of Mathematics and
Natural Sciences
Department of Physics
www.ikp.uni-koeln.de
- Institute of Physics II
www.ph2.uni-koeln.de

Imprint

Publisher

Technische Universität München
 Forschungs-Neutronenquelle
 Heinz Maier-Leibnitz (FRM II)
 Lichtenbergstr. 1
 85747 Garching
 Germany

Phone: +49.89.289.14966
 Fax: +49.89.289.14995
 Internet: www.mlz-garching.de
www.frm2.tum.de
 EMail: jahresbericht@frm2.tum.de

Editorial Office, Design and typesetting

Ramona Bucher
 Ariane Fröhner
 Anke Görg
 Connie Hesse
 Elisabeth Jörg-Müller
 Christine Kortenbruck
 Andrea Voit

Editors

Rainer Bruchhaus
 Henrich Frielinghaus
 Robert Georgii
 Michael Hofmann
 Olaf Holderer
 Wiebke Lohstroh
 Andreas Ostermann
 Björn Pedersen
 Olaf Soltwedel
 Anatoliy Senyshyn
 Yixi Su

Photographic credits

Graf Flugplatz: 4 top

Wenzel Schürmann, TUM:
 4 (top, bottom 1st, 3rd and 4th from left), 9, 10/11
 (background), 12/13 (background), 13 (bottom), 47,
 71, 78 (top, bottom), 80 (middle, bottom), 82 (bot-
 tom), 83 (middle), 84 (no. 3, 6, 10), 85 (no. 9), 87
 (bottom), 96, 97, back cover

Bernhard Ludewig:
 10 (top)

Wolfgang Filser:
 10 (bottom)

Morio (Wikimedia):
 11 (bottom)

Tomasz Sienicki:
 13 (top)

Tobias Hase:
 60

Sergiogen - Fotolia:
 77

Editors, authors or FRM II / TUM:
 other images

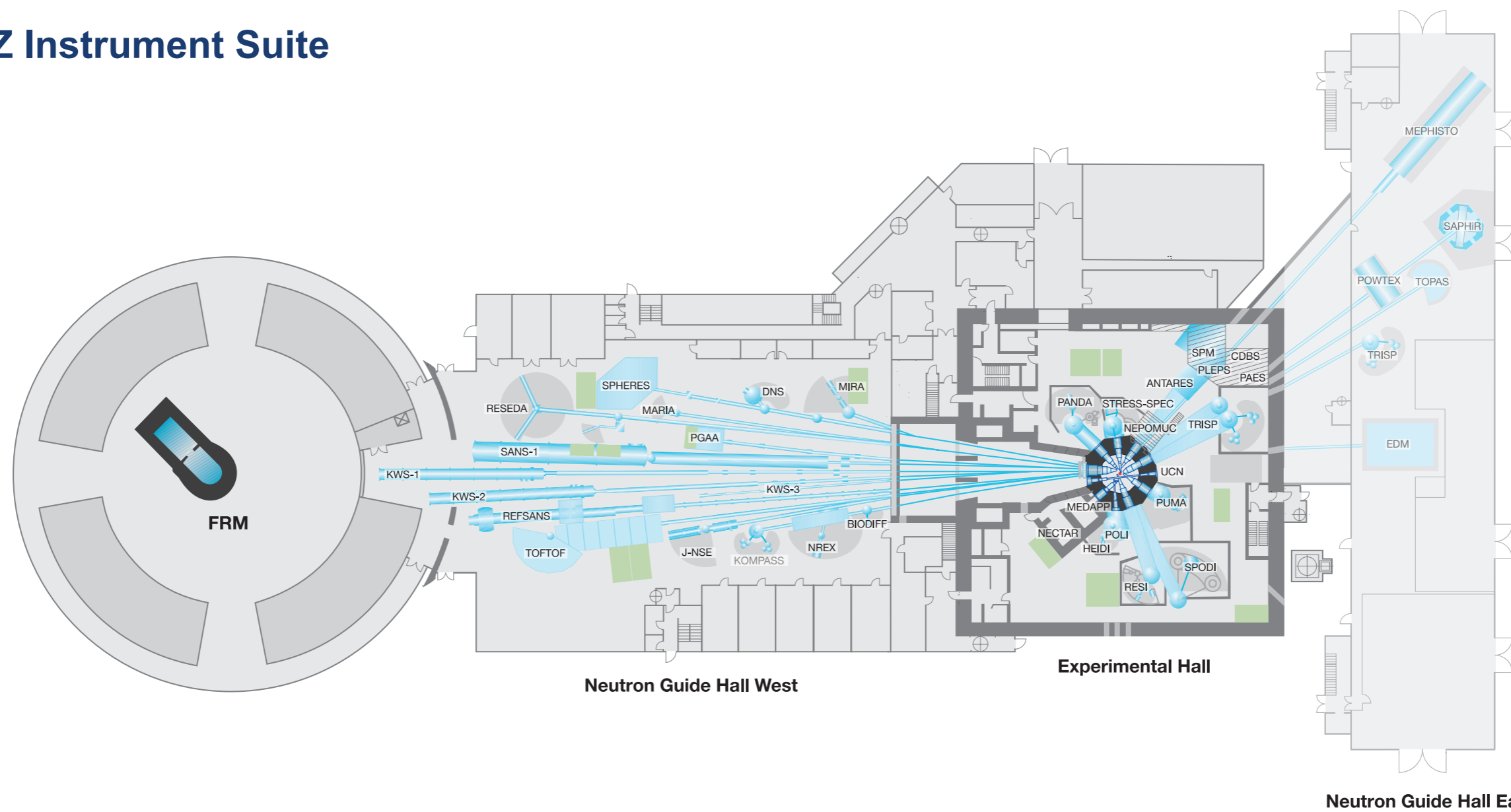
Front page:

The beautiful crystals are the polar magnet VOSe_2O_5 , whose crystal structure consists of stacked square lattices tetragonal pyramids.
(see scientific highlight 'Skyrmions in a polar magnet' on page 11 top)

Back page:

First groundbreaking ceremony for the new science and technology building of the Technical University of Munich as well as the laboratory and office building of the Research Center Jülich for use by the Heinz Maier-Leibnitz Zentrum.

MLZ Instrument Suite



Instrument	Description	Neutrons	Operated by	Funding	Instrument group at MLZ
ANTARES	Radiography and tomography	cold	TUM	TUM	FRM II
BIODIFF	Diffractionmeter for large unit cells	cold	TUM, JCNS	TUM, FZJ	FRM II, JCNS
DNS	Diffuse scattering spectrometer	cold	JCNS	FZJ	JCNS
HEIDI	Single crystal diffractometer	hot	RWTH Aachen	FZJ	JCNS
J-NSE	Spin-echo spectrometer	cold	JCNS	FZJ	JCNS
KOMPASS*	Three axes spectrometer	cold	Uni Köln, TUM	VF	FRM II
KWS-1	Small angle scattering	cold	JCNS	FZJ	JCNS
KWS-2	Small angle scattering	cold	JCNS	FZJ	JCNS
KWS-3	Very small angle scattering	cold	JCNS	FZJ	JCNS
MARIA	Magnetic reflectometer	cold	JCNS	FZJ	JCNS
MEPHISTO**	Instrument for particle physics, PERC	cold	TUM	TUM, DFG	FRM II
MIRA	Multipurpose instrument	cold	TUM	TUM	FRM II
MEDAPP	Medical irradiation treatment	fast	TUM	TUM	FRM II
NECTAR	Radiography and tomography	fast	TUM	TUM	FRM II
NEPOMUC	Positron source, CDBS, PAES, PLEPS, SPM	-	TUM, UniBw München	TUM	FRM II
NREX	Reflectometer with X-ray option	cold	MPI Stuttgart	MPG	MPI Stuttgart
PANDA	Three axes spectrometer	cold	JCNS	FZJ	JCNS

Instrument	Description	Neutrons	Operated by	Funding	Instrument group at MLZ
PGAA	Prompt gamma activation analysis	cold	Uni Köln	TUM	FRM II
PUMA	Three axes spectrometer	thermal	Uni Göttingen, TUM	VF, TUM	FRM II
POLI	Single-crystal diffractometer polarized neutrons	hot	RWTH Aachen	VF, FZJ	JCNS
POWTEX*	Time-of-flight diffractometer	thermal	RWTH Aachen, Uni Göttingen, JCNS	VF, FZJ	JCNS
REFSANS	Reflectometer	cold	GEMS	VF, HZG	GEMS
RESEDA	Resonance spin-echo spectrometer	cold	TUM	TUM	FRM II
RESI	Single crystal diffractometer	thermal	LMU	TUM	FRM II
SANS-1	Small angle scattering	cold	TUM, GEMS	TUM, HZG	FRM II, GEMS
SAPHIR*	Six anvil press for radiography and diffraction	thermal	Uni Bayreuth	VF	FRM II
SPHERES	Backscattering spectrometer	cold	JCNS	VF, FZJ	JCNS
SPODI	Powder diffractometer	thermal	KIT	VF, TUM	FRM II
STRESS-SPEC	Materials science diffractometer	thermal	TUM, TU Clausthal, GEMS	TUM, HZG	FRM II, GEMS
TOFTOF	Time-of-flight spectrometer	cold	TUM	TUM	FRM II
TOPAS*	Time-of-flight spectrometer	thermal	JCNS	FZJ	JCNS
TRISP	Three axes spin-echo spectrometer	thermal	MPI Stuttgart	MPG	MPI Stuttgart
UCN*	Ultra cold neutron source, EDM	ultra-cold	TUM	TUM, DFG	FRM II

*construction
 **reconstruction
 VF: instrument construction funded by "BMBF-Verbundforschung" (Collaborative Projects)



Heinz Maier-Leibnitz Zentrum (MLZ)

www.mlz-garching.de

DOI: 10.14459/2018md1431530